SLOW PROTON PRODUCTION and NEUTRON DISSOCIATION AT 100 and

400 GeV/c FROM NEUTRON TARGETS IN HADRON-DEUTERON

COLLISIONS

A dissertation presented

by

Arthur Ted Brody

to

The Graduate School

in partial fulfillment of the requirements

for the degree of

Doctor of Philosophy

in

Physics

State University of New York at Stony Brook

August 1978

**STATE** UNIVERSITY OF NEW YORK

AT STONY BROOK

Arthur Brody

We, the dissertation committee for the above candidate for the Ph.D. degree, hereby recommend acceptance of the dissertation.

_____
Roderich Engelmann, Advisor

_____
Janos Kirz

_____
John Smith

_____
Francis Bonner, Chemistry Dept.

The dissertation is accepted by the Graduate School.

SIGNED:_____
        Herbert Weisinger, DEAN
        The Graduate School

DATE:_____

August 1978

ABSTRACT

Presented here are the results of the analyses of data obtained from exposures of the 30-inch Fermilab deuterium-filled bubble chamber to mixed, positively charged beam particles incident at 100 GeV/c and proton beam particles incident at 400 GeV/c. The Proportional Hybrid System was used to identify the beam particles, and on low multiplicity events, to improve fast track momenta for the 100 GeV/c data sample. Topological hd and hn cross sections are extracted from both data samples. Events with 3 or 4 prongs at 100 GeV/c are fit to the mass hypothesis $hd \rightarrow hpp\pi^-$ and a free neutron cross section for $hn \rightarrow h(p\pi^-)$ is extracted. This cross section is then compared with values obtained at other energies or measured using different techniques. The production of protons with laboratory momenta less than 1.4 GeV/c is also studied for the full event samples at both energies. The inclusive proton cross sections are seen to scale as functions of M^2/s and t, leading us to make a detailed study of these cross sections in the context of a Mueller-Regge formalism.

iii

To my father

Abraham Harris Brody

City College of New York B.S. 1930

New York University M.S. 1933

TABLE OF CONTENTS

FIGURE CAPTIONS

LIST OF TABLES

so given are the TVGP-PWGP-TRKORG calculated downstream

average track momenta and the corresponding r.m.s. de-

viations.   186

I. INTRODUCTION

A. General Information

This work deals with the analysis of exposures of the 30-inch deuterium-filled bubble chamber at Fermilab to mixed positively charged beam particles at Fermilab energies. The use of the Proportional Hybrid System (PHS) allowed us to identify individual beam particles, mostly protons and pions. Statistics will restrict us to studying only the proton and pion beam samples, or pd and $\pi^+ d$ interactions. As well as identifying beam particles, the PHS downstream of the bubble chamber yields additional information on fast-forward tracks leaving the bubble chamber. In particular, the momentum resolution of measurements made on these tracks may be improved greatly over the resolution of bubble chamber measurements.

B. Deuterium Targets

The use of liquid deuterium as a target affords a unique opportunity to observe processes not available when using hydrogen targets, or too difficult to analyze in more complex nuclear targets. The deuteron can serve as a source of neutron targets if one restricts his attention to the incoherent class of events where only one nucleon, the neutron, participates actively, and one assumes the validity of the impulse approximation. See App. G. Also, in the simple deuteron nucleus, both nucleons may be involved in an interaction, providing information about coherent and rescattering phenomena. See App. G. Though these phenomena are not the main

1

interest of this work, it will be necessary to have an understanding of their effects in order to select neutron target events.

Neutron target reactions will be noted as either

$$h + n \rightarrow X \qquad\qquad\qquad \text{I.1a}$$

or

$$h + d \rightarrow p_s + X \qquad\qquad\qquad \text{I.1b}$$
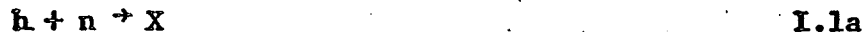
where h denotes either a proton or pion beam particle and p_s is the deuterium proton not involved in the interaction, the spectator proton. This proton may or may not be visible[1] in the bubble chamber so that a neutron target event may have either an odd or even number of outgoing tracks (prongs). The number of prongs in an event will be referred to as the event multiplicity. From the odd-prong event sample we will extract hadron-free neutron cross sections.

C. Inclusive Reactions

Bubble chamber measurements alone provide good momentum resolution for tracks with momenta of a few GeV/c or less in the LAB. (See App. A.) Data is then available for studying inclusive reactions where only particles slow in the LAB, i.e. in the target fragmentation region[2], are measured. The following reaction has been studied with beam particles incident on target with momenta of 100 and 400 GeV/c.

$$h + n \rightarrow p + X \qquad\qquad I.2$$

Here, h is the beam hadron, n is the neutron target, and X

represents all remaining particles not specified on the right-hand

side (in the final state) of the reaction.

The slow proton spectra (Eq. I.2) may be used to test the

validity of Mueller-Regge analysis[3] in the Triple-Regge limit[4].

Basically stated, the behavior of cross sections should be

governed by the behavior of singularities in the exchange- or t-

channel. For the inclusive reaction a+b $\rightarrow$ c+X in the s-channel,

the t-channel reaction is a+$\bar{c}$ $\rightarrow$ $\bar{b}$+X, where $\bar{b}$ and $\bar{c}$ are the anti-

particles of b and c. Physically, s and t are the center-of-mass

energie- squared for the s- and t- channels respectively. This

is shown schematically in Fig. I.1a. (See App. A for the

mathematical definition of s, t and other kinematic variables

used.) The position of a singularity changes with t, and is said

to map out a Regge trajectory $\alpha(t)$. In this case, the behavior of

the cross section is governed by the possible exchange of trajectories.

Fig. I.1b represents the specific reaction in Eq. I.2. The

I=1 label next to the exchange trajectory (wavy line) indicates

that charge (isospin) must be transferred between the two vertices,

in order that the neutron may become a proton, and M^2 is the mass-

squared of the X system of particles. Possible trajectories that

could mediate the charge exchange reaction are the π and ρ/A_2

trajectories. It has been suggested by Bishari[6], and Field and Fox[7], that at high energies, the pion trajectory should dominate, but apriori, there is no reason to rule out ρ/A_2 contribution.
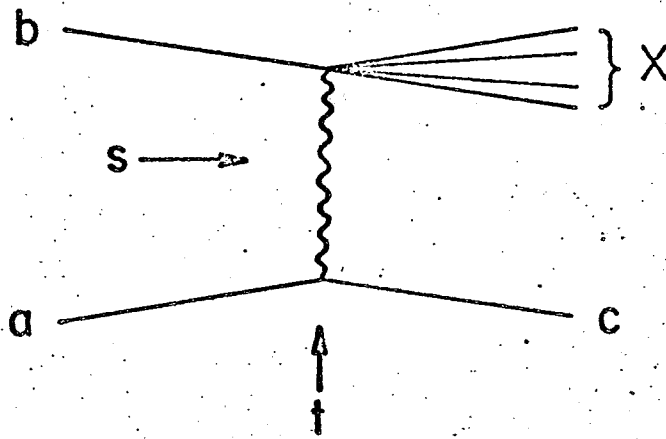
Fig. I.1a
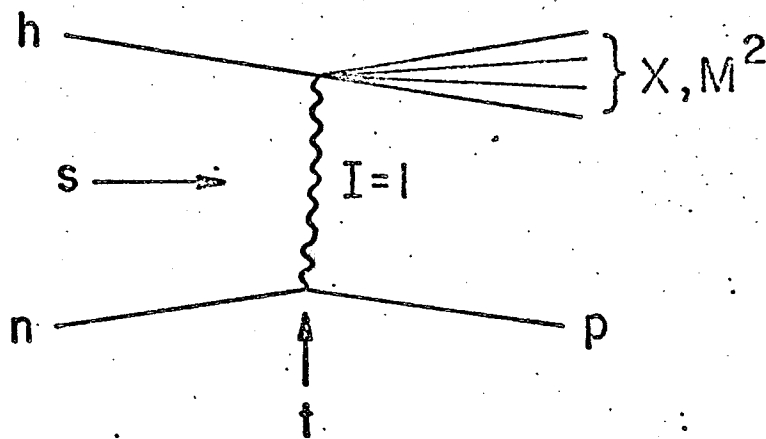
Fig. I.1b

The availability of two types of beam particles at 100 GeV/c allows us to test the validity of the factorization hypothesis[7], implicit in the Mueller-Regge formalism. In the formalism, the effects of the upper and lower vertices on the cross section may be factorized into a product of two functions, $\gamma_{hx}^R \cdot \gamma_{np}^R$, which are independent of each other. The vertices are then "isolated" from each other, a change in beam particle type only changing γ_{hx}^R. Naively, the upper (Reggeon-beam-X) vertex in Fig. I.1b can be viewed as describing the total cross section for the process hR → X, $\sigma_{TOT}(hR)$, at center-of-mass energy M. Therefore, if the same Regge trajectories contribute to the $\pi^+ n$ → pX reaction as to the pn → pX reaction, factorization implies that the two inclusive cross sections should scale as the total cross sections, $\sigma_{TOT}(\pi R)/\sigma_{TOT}(pR)$, and that the shape of the differential cross sections (see App. A), governed by the exchange mechanisms, should also scale.

D. Exclusive Reactions

Improved momenta for fast tracks are obtained by combining the PHS and bubble chamber measurement data (TRACK ORGANIZING). We have therefore attempted to kinematically fit 3- and 4- prong events in the 100 GeV/c data sample to the mass hypothesis in Eq. I.3a, which at high energies have only been studied in counter experiments at Serpukhov and Fermilab, using neutron beam particles incident on hydrogen targets[8]. Exclusive cross sections in general

tend to fall off with energy. To map out the trend of this particular cross section up to an incident beam momentum of several hundred GeV/c is of interest because this cross section seems to change its energy dependence at high energies.

$$h + d \rightarrow h + p + p + \pi^- \qquad \text{I.3a}$$

The hadron h in the final state has the same identity as the incident beam hadron, and one of the final state protons is a possible spectator. While the above counter experiments make high statistics measurements, the determination of the neutron beam flux is difficult to make, and therefore the absolute cross sections difficult to extract. Our bubble chamber experiment has low statistics, but our absolute total cross section measurement is easier to make, as our beam flux is well known.

One might think that as well as measuring deuteron break-up events, we could measure a cross section for the coherent deuteron reaction

$$h + d \rightarrow h + \pi^+ + \pi^- + d \qquad \text{I.3b}$$

where d represents the deuteron. As will be discussed in Section II.G, our efficiency for measuring this reaction was poor and no estimate could be made.

Using our knowledge of the deuteron, we can identify neutron target events on an event-by-event basis, and extract the following cross section.

$$h + n \rightarrow h + (p\pi^-).$$
I.4a

$$h + n \rightarrow (h\pi^-) + p$$
I.4b

The pion has been specifically associated with being in either the beam or target fragmentation region. We might represent these two reactions as in Figs. I.2a and I.2b.

The $(p\pi^-)$ system in Fig. I.2a can have the same quantum numbers (S-spin, I-isospin, B-baryon number) as the neutron target. It certainly has the same electric charge Q, and the exchange mechanism cannot transfer charge from the upper (beam) vertex to the lower (target) vertex. If the mass of the $(p\pi^-)$ system is on the order of 1 or 2 nucleon masses, then Eq. I.4a is a quasi-elastic reaction; i.e. $a+b \rightarrow a+b^*$ where b^* is an excited state of particle b, and should have properties similar to elastic scattering. In particular, it should be dominated by a diffractive[9] mechanism, which involves zero quantum number exchange. The neutron is said to diffractively dissociate. As a rule, purely diffractive processes have little energy dependence at high energies, reflecting the constancy of elastic cross sections, and this can be checked by comparing our results with cross section measurements at other energies. A marked energy dependence would imply a non-negligible non-diffractive component in neutron dissociation.

Fig. I.2b, on the other hand, must involve a charge exchange mechanism. The cross section is expected to fall with energy[11] and
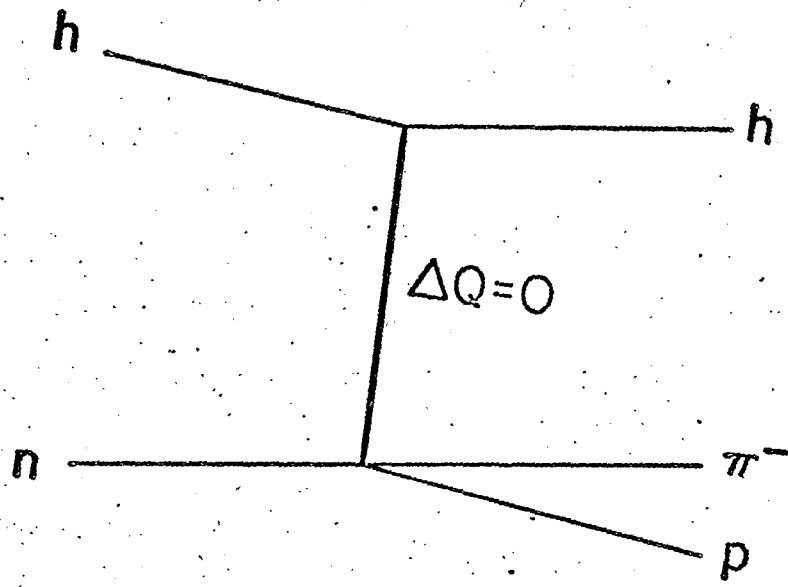
Fig. I.2a
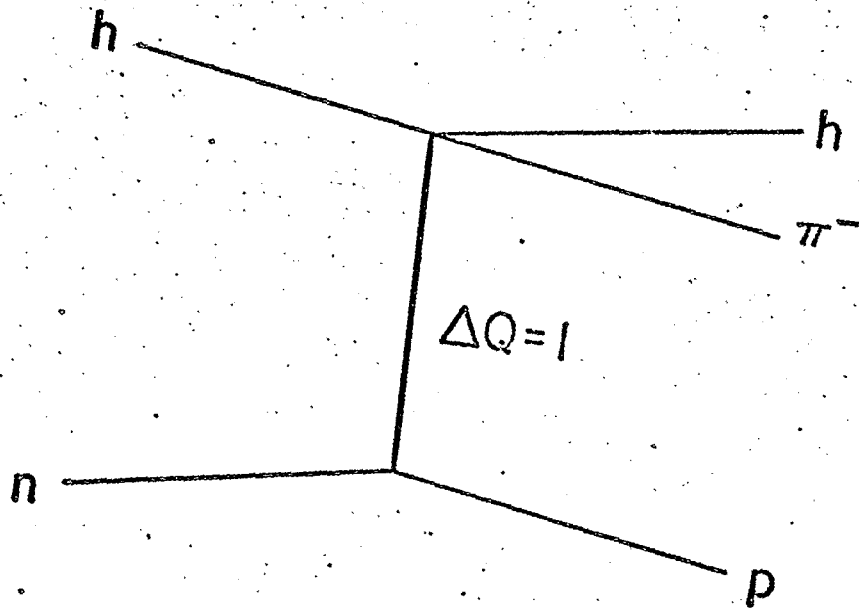
Fig. I.2b

this behavior has been verified at lower energies by bubble chamber measurements. At 28 GeV/c[10] the charge exchange reaction is seen to constitute only 12% of the $pn \to pp\pi^-$ events, and at Fermilab energies, the cross section should be so small as to be unmeasurable in our experiment. Indeed, we will find only one possible event candidate for charge exchange in our total of 46 successfully fitted events.

E. Outline

In Chapter II, the data acquisition and experimental techniques will be discussed. The multiplicity distributions (topological cross sections) will be extracted from the data in Chapter III, and will be used in calculating the inclusive and exclusive cross sectionsin the following chapters. Chapter IV will present the cross section results and analysis of the neutron dissociation reaction, and Chapter V the cross section results and analysis of slow proton production from a neutron target. Much of the details of Chapters II through V have been placed in appendices.

REFERENCES

1) The range of a 120 MeV/c proton in deuterium is only 5 mm.

2) For a description of the beam, target and central kinematic
regions and their physical interpretations see:
K.Gottfried, "An Introduction to Multiparticle Processes"
(CERN Ref. TH.1615, 1973).
M.Jacob, "Multi-body Phenomena in Strong Interactions"
(CERN Ref. TH.1683, 1973).
E.L.Berger, "Multiparticle Production Processes at High
Energy" (CERN Ref. TH.1737, 1973).

3) A.H.Mueller, Phys. Rev. D2, 2963 (1970);
H.M. Chan et al., Phys. Rev. Lett. 26, 672 (1971).

4) C.E.DeTar et al., Phys. Rev. Lett. 26, 675 (1971).

5) M. Bishari, Phys. Lett. 38B, 510 (1972).

6) R.D. Field and G.C. Fox, Nucl. Phys. B80 367 (1974).

7) Proofs of the factorization of residues in Regge Theory
can be found in:
M.Gell-Mann, Phys. Rev. Lett. 8, 263 (1962);
V.N. Gribov and I.Ya Pomeranchuk, Phys. Rev. Lett. 8, 343 (1962).

8) A.Babaev et al., Nucl. Phys. B116, 28 (1976).
J.Biel, Thesis - "A Study of the Dissociation Reaction
n+p → pπ⁻ + p For Neutron Momenta Between 50 GeV/c and 300
GeV/c", UR-614 (Univ. of Rochester, 1977).

9) A great deal of literature exists on diffractive processes.

   An early reference is:

   M.L.Good and W.D.Walker, Phys. Rev. 120, 1857 (1960).

   More recent review articles are:

   H.J. Lubatti, Acta. Phys. Pol. B3, 721 (1972);

   S.V. Mukhin and V.A.Tsarev, "AIP Conference Proceedings" No. 23,

   C.Carlson ed. (American Inst. of Phys., New York, 1974).

   U.Amaldi et al.Ann. Rev. Nucl. Sc. 26, 385 (1976).

10) J.Hanlon et al., Phys. Rev. D12, 673 (1975)

11) H.M. Chan, "Current Phenomenology of Hadron Interactions "

   (Notes of lectures given at SUNY at Stony Brook, 1977).

II. DATA ACQUISITION

A. Film Exposures

Pictures were taken during three separate exposures which will be called RUNS 1, 2 and 3. The Fermilab 30-inch bubble chamber was filled with liquid deuterium (negligible H_2 contamination) for each run. The first exposure of 41,000 pictures utilized a secondary beam of positively charged particles. The momentum was found to be 97.7 GeV/c with a momentum bite of .5%. RUN 2 was a 100,000 picture exposure of the chamber to a 400±2 GeV/c proton beam with negligible non-proton contamination. The third exposure of 45,000 pictures was similar to RUN 1, but with paraffin inserted in the beam line upstream of the bubble chamber to enhance the π^+/p ratio. For all runs the bubble chamber was multiply pulsed for each main ring accelerator cycle. A summary of each run is given in Table II.1.

Pictures were taken with three cameras (3 views) for each frame on 35mm film. Film from RUN 1 was divided between the collaborating institutions of Carnegie-Mellon University, Fermilab, the University of Michigan and the State University of New York at Stony Brook. RUNS 2 and 3 had Carnegie-Mellon, Fermilab and Stony Brook collaborating.

RUNS 1 and 3 comprise Fermilab Experiment E-194, RUN 2 was Fermilab Experiment E-196.

TABLE II.1

	RUN 1	RUN 2	RUN 3
# Pictures	42K	100K	46K
Scannable frames (%)	85	76	86
Beams/frame[*]	6.3	4.95	5.84
Events/frame[*]	0.45[†]	0.55	0.38[†]
p (%)	57	100	40
π^+ (%)	39	——	56
K^+ (%)	2	——	2
μ^+ (%)	2	——	2

[*] per scannable frame

[†] $N \geq 3$ prong events

B. Proportional Hybrid System

Upstream of the bubble chamber in the beam line and immediately downstream are a series of proportional wire chambers, scintillators and Čerenkov counters called the Proportional Hybrid System (PHS). The system facilitates the tagging of individual beam particles and the improving of fast outgoing track momenta. See Fig. II.1.

Signal pulses from each proportional wire chamber (PWC) sense wire are discriminated and amplified in the wire chamber vicinity and transmitted as a digital signal and stored in a 16-bit memory word. A coincidence from scintillators S_1 and S_2 is used to set up a time slot for individual beam tracks. The Č-counter information is stored like sense-wire signals in pseudo planes 1 and 2. At the end of a bubble chamber spill, the data from local memory are transmitted to a PDP-11 computer in the bubble chamber control room, and written out on tape in a Fortran-compatible format.

The Čerenkov system consisted of two separate counters, one set to fire on the passage of a π^+ particle, the other on a K^+ particle. A null signal was assumed to be a proton identification. Non-interacting muon beam tracks were identified by firing PWC H, which was shielded by lead.

Each wire chamber, except plane I, consisted of at least three planes with their wire directions oriented 120° relative to

BEAM

-500m — ☐ C

-300m — --|-- PWC I

-175m — --|-- PWC A
        ╤╤╤ SC I

-16m — --|-- PWC C

-2.5m — ╤╤ PWC B
         ╤╤ SC II

0m — ◯⤳ BC

2.0m — ----|---- PWC D
2.3m — ----|---- PWC E
3.0m — ----|---- PWC F

5.5m — ----|--- PWC G
        ▭ Pb CONVERTER
6.0m — ----|--- PWC H

Fig. II.1

16

Fig. II.2a

VIEW II
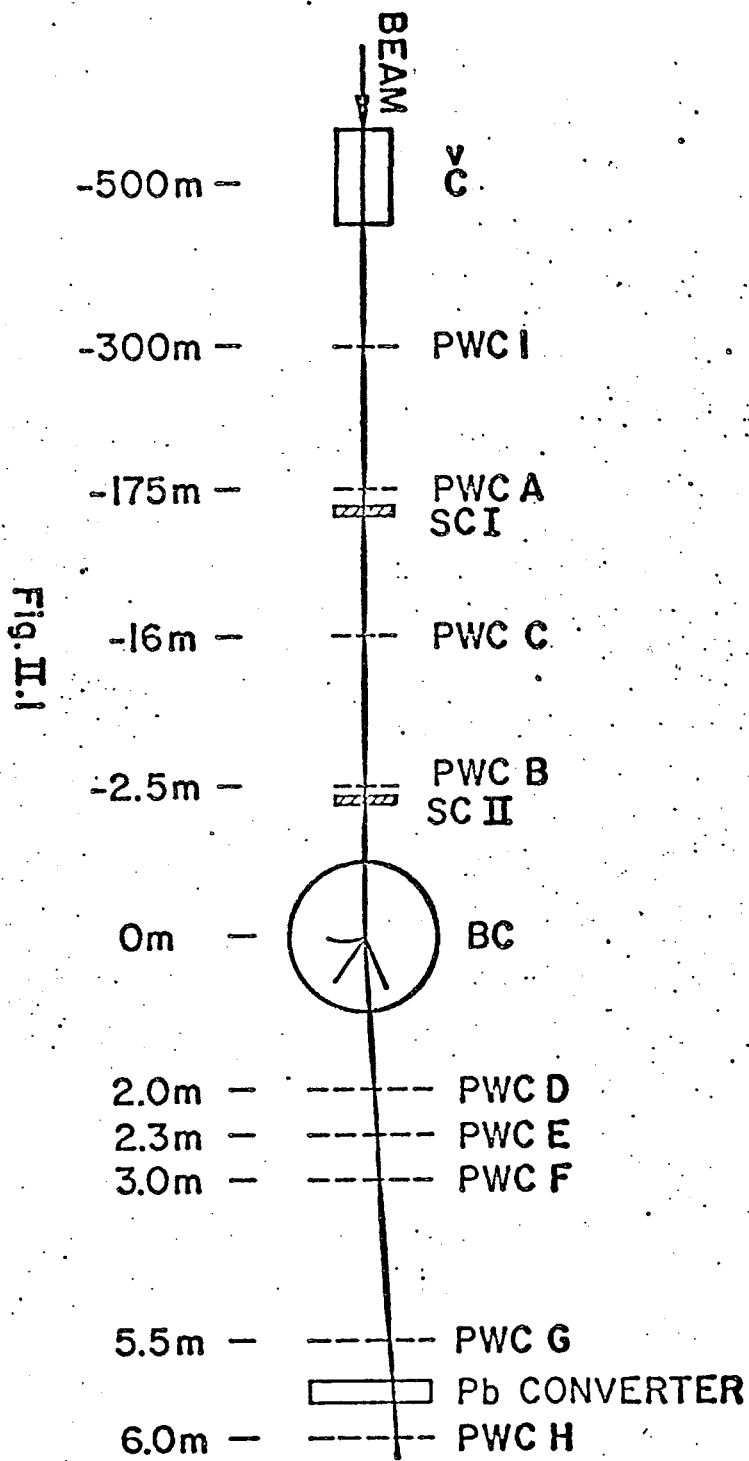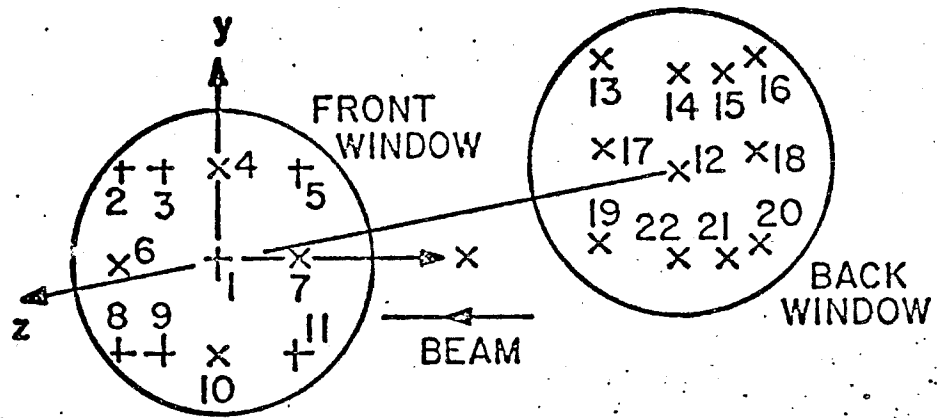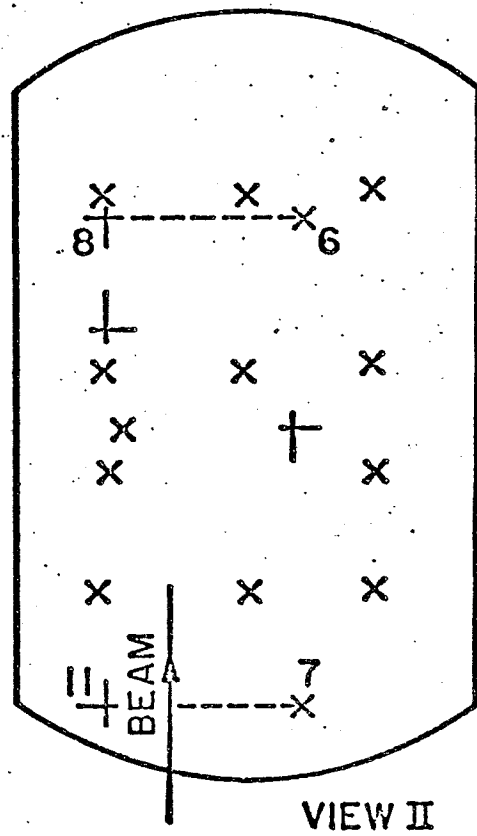
Fig. II.2b

each other around an axis parallel to the beam direction. The
3-plane per chamber construction allows one to uniquely define a
space point through which a particle passes if all planes in the
chamber fire. Some of the downstream chambers contain planes
parallel to one of the three primary planes but offset by 1 mm
(spacing between wires is ∿2 mm) to obtain greater accuracy in
position determination. The chambers were monitored after each
roll of film by looking at the total hits distribution per wire
and the missed hits on reconstructed tracks.[2] The spatial profile
of the beam entering the bubble chamber was monitored by accumulating
hits on the vertical plane of PWC A and the horizontal planes of
PWC's B and C. More details of the physical system are available
in the literature[3],Section II-C, and Appendix B.

C. Coordinate Systems and Surveys.

Two separate coordinate systems were used, one for the
bubble chamber system and one for the PHS, resulting from separate
surveys of the systems. Rotations and translations between these
two systems are corrected for when the data is merged.

Figures II.2a and II.2b give the approximate chamber
orientation, camera and fiducial positions. The bubble chamber
origin was chosen to be at Fiducial 1 on the front glass, the
z-axis pointing towards the cameras and the orientation of the x-
and y- axes defined by the other fiducial marks. The beam is in
the general negative x direction. Relative positions of the

fiducials on the front and back glasses were determined by
mechanical measurements, and a theodolite survey was used to
determine the rotation and translation of the back glass and the
chamber depth, which can change from run to run.

The PHS coordinate system is defined as follows. The x-
axis connects the intersection of the center lines of planes 4
and 5 and the intersection of the center lines of planes 11 and 12,
the positive direction being in the general direction of the beam.
The center line of the plane is an imaginary line equidistant from
and parallel to the center wires in the plane. The x-z plane is
chosen to be horizontal to the ground with the y-axis pointing
vertically downward. The orientation chosen for the z-axis makes
the system right-handed, and x=0 is chosen to correspond with the
bubble chamber origin. A rotation of the PHS system by 180° around
its z-axis and a translation by 8 cm and -18 cm in the y and z
directions respectively, will align the PHS and bubble chamber
systems to within a few milliradians, but it is important to obtain
a more accurate alignment because a misalignment of as little as
.5 mr will wrongly reconstruct the momentum of a 100 GeV/c track
by several GeV/c. More precise translations and rotations will be
obtained by the program FIDROT. See Appendix C.

The relative positions of planes within the chamber and
the wire spacings within the planes are known from construction, so
that if the chambers are perpendicular to the ground, e.g. in the
y-z plane, only three parameters are needed to describe the ith

plane; x_i, the chamber distance from the origin plus the intra-chamber distance, R_i, the perpendicular distance from the x-axis to the planes center line, and ω_i, the angle measured clockwise from the y-axis to the direction of increasing wire address. R_i may be negative if the center line lies in a negative ω_i direction. See Figure II.3.

The distances of each chamber were measured before RUNS 1 and 3. Plane angles ω_i were measured mechanically with a level. The R_i of each plane was determined by the program SURVEY. See App. B.

D. Scan

Scanning of the film for beam interactions was done using projections between 1.1 and 1.4 times lifesize. Some difficult events with many overlapping prongs or secondary scatters and neutral vertices close to the primary vertex were studied at higher magnification. This was found to be of little help in determining the primary event prong count.

The scanner was instructed to reject frames in which one or more views were missing, more than 15 beam tracks were entering the frame (12 beam track limit for the 400 GeV/c data), or more than 20 tracks total entering. The scanning fiducial volume was defined by the fiducial rectangle 6-7-8-11 in View II, the master view (see Fig. II.2b), and only events within these limits in the scannable frames were accepted. All events with two or more prongs
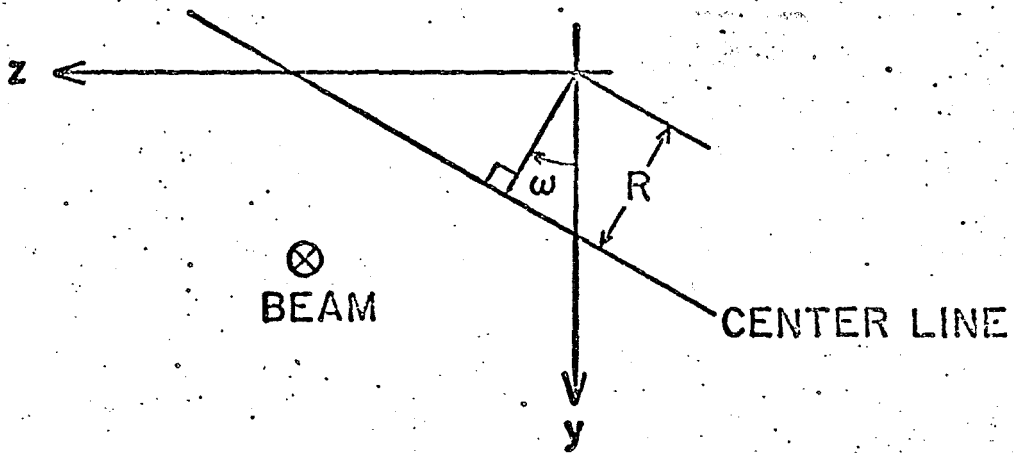
Fig. II.3

had their prong count and projected position recorded. In addition, all neutral decays (vees), converting photons (gammas), Dalitz pairs and neutral particle interactions (neutral stars) had their positions recorded.

Although two independent scans were performed and discrepancies were resolved, for many primary events one could not clearly count the prong numbers because of a secondary interaction, a nearby primary vertex, or a very close spacing of forward tracks. These uncountable events were given a prong count range corresponding to the best estimate of the scanner. The uncountable events from the 100 GeV/c sample were distributed between their minimum and maximum prong counts as to reflect the multiplicity distribution of the countable events within these limits. The sum of the weights contributed by the multiplicity range was normalized to 1.0, so that each uncountable event had a total weight of 1.0. Uncountable events tend to have a high multiplicity and this method probably underestimated the high multiplicity tail of the distribution, but the uncountables were only 3% of the data.

Due to the large number of uncountable events at 400 GeV/c, we chose the following method to distribute the uncountable events: The events were distributed as to maintain the fraction of odd events (f_o) in the entire data sample as determined by the countable events. Odd-prong counts within the prong estimate range contribute a fractional weight of f_o/n_o, where n_o is the number of possible odd-prong entries within the range. At each even prong count within the

range, $(1-f_o)/n_e$ is contributed to the event weight, where n_e is the number of possible even-prong entries. We believe this method gives a better estimation of the tail, only assuming f_o to be the same in the tail as the rest of the distribution. 9% of the 400 GeV/c scanned events were uncountable. The errors assigned to redistrib ted uncountable events are discussed in App. D.

Tables II.2a and b contain the raw multiplicity distribution for parts of the 100 and 400 GeV/c data samples. The 100 GeV/c sample contains the part of the data where all events were measured regardless of topology (approximately 70% of RUN 1) and where the beam has been successfully tagged (90%). We assume that the tagging efficiency is independent of beam mass and event multiplicity. The 400 GeV/c sample contains approximately 55% of the total data taken. Both odd-prong and odd-plus-even (deuterium) event distributions are presented. An odd-prong event in the deuterium distribution is given a multiplicity of $N + 1$ to account for the invisible spectator proton.

We use the methods of Evans and Barkas[4] to find the scanning efficiency as a function of multiplicity. For events with 3 or more prongs the efficiency is 99±1% or better. The scanning efficiency for 2-prongs in the 400 GeV/c film was 97±1%.

E. Track Measurement and Reconstruction

1. Bubble Chamber

TABLE II.2a

N	RAW 100 GeV/c		RAW 400 GeV/c
	pd	$\pi^+ d$	pd
3	410	174	915
5	492	215	996
7	420	197	1087
9	289	121	1028
11	168	87	845
13	82	46	576
15	33	22	408
17	10	3	249
19	4	1	138
21	2	1	82
23	1	—	27
25	—	—	19
27	—	—	7
29	—	—	1
TOTAL	1911	867	6378

TABLE II.2b

N	RAW 100 GeV/c		RAW 400 GeV/c
	pd	π^+d	pd
4	1549	660	2491
6	1719	735	2904
8	1442	412	3198
10	959	412	3008
12	554	268	2459
14	262	129	1718
16	134	52	1177
18	35	16	710
20	10	6	428
22	2	2	245
24	1	1	119
26	—	—	71
28	—	—	28
30	—	—	7
32	—	—	5
34	—	—	—
36	—	—	1
TOTAL	6667	2953	18569

The selection criteria for events from the scanned sample to be measured were different at some institutions, but all criteria contained the subsets of data to be used in subsequent analyses. The basic philosophy was to measure all events with 3 or more prongs which appear to be neutron-target candidates. The candidates are either odd-prong events with an assumed invisible spectator proton or even-prong events with a possible spectator proton. See App. G. For all accepted events, the beam track and tracks with a projected momentum less than 1.4 GeV/c were measured . If a track had a secondary scattering within a projected length of 10 cm, it was also measured, regardless of curvature. In addition, all remaining tracks were measured for 3- through 6- prong events in RUN 1 (the exclusive event sample).

The events were measured on various image-plane and film-plane digitizers (IPD's and FPD's). The FPD's were roughly twice as accurate as the IPD's. The track measurements were reconstructed in space and momenta were determined by the Three View Geometry Program (TVGP)[5]. For 3- and 4- prong events in the exclusive sample, kinematic fits to various mass hypotheses were tried using the SQUAW[6] program. In all three views, the measurer had to identify each track and at Stony Brook, a track matching program inserted into TVGP generated additional solutions, which occured primarily in the exclusive sample where the many fast forward tracks may be confused. In cases where more than one solution reconstructed successfully, the fit for the parametrized tracks with the minimum

r.m.s. deviation (FRMS) from the measured film points was kept.

It was found that for the exclusive event sample, there were some events at each institution which did not satisfy charge balance arising from the fact that the fast track curvature was difficult to measure. These events were kept for further processing, as the merging of bubble chamber data with wire chamber information resulted in a correction of the charge imbalance. The sample of 3- and 4- prong events input to SQUAW, was better than 98% charge balanced.

On IPD and FPD measurements, anywhere from 4 to 7 points were measured per track per view except for short stopping or scattering tracks. The momentum of stopping tracks was almost always determined by range and of other tracks by curvature. The Fermilab exclusive sample was measured on a semi-automatic measuring machine (SAMM), where 19 points per track-view were measured. For a detailed investigation of the error assignments for the various institutions, see App. E. All tracks had an FRMS less than 25μ or the tracks were remeasured.

Masses for each measured outgoing track were identified as follows: Negative tracks were assigned a π^- mass hypothesis and positive non-stopping tracks ≤ 1.4 GeV/c were identified as a proton or pion by the tracks' bubble densities or ionizations.[7] In Fig. II.4, the 1.4 GeV/c momentum limit is seen to yield a 45% difference in $1/\beta^2$, where β is the velocity of the particle in the LAB. As energy loss per unit distance is proportional to $1/\beta^2$, the
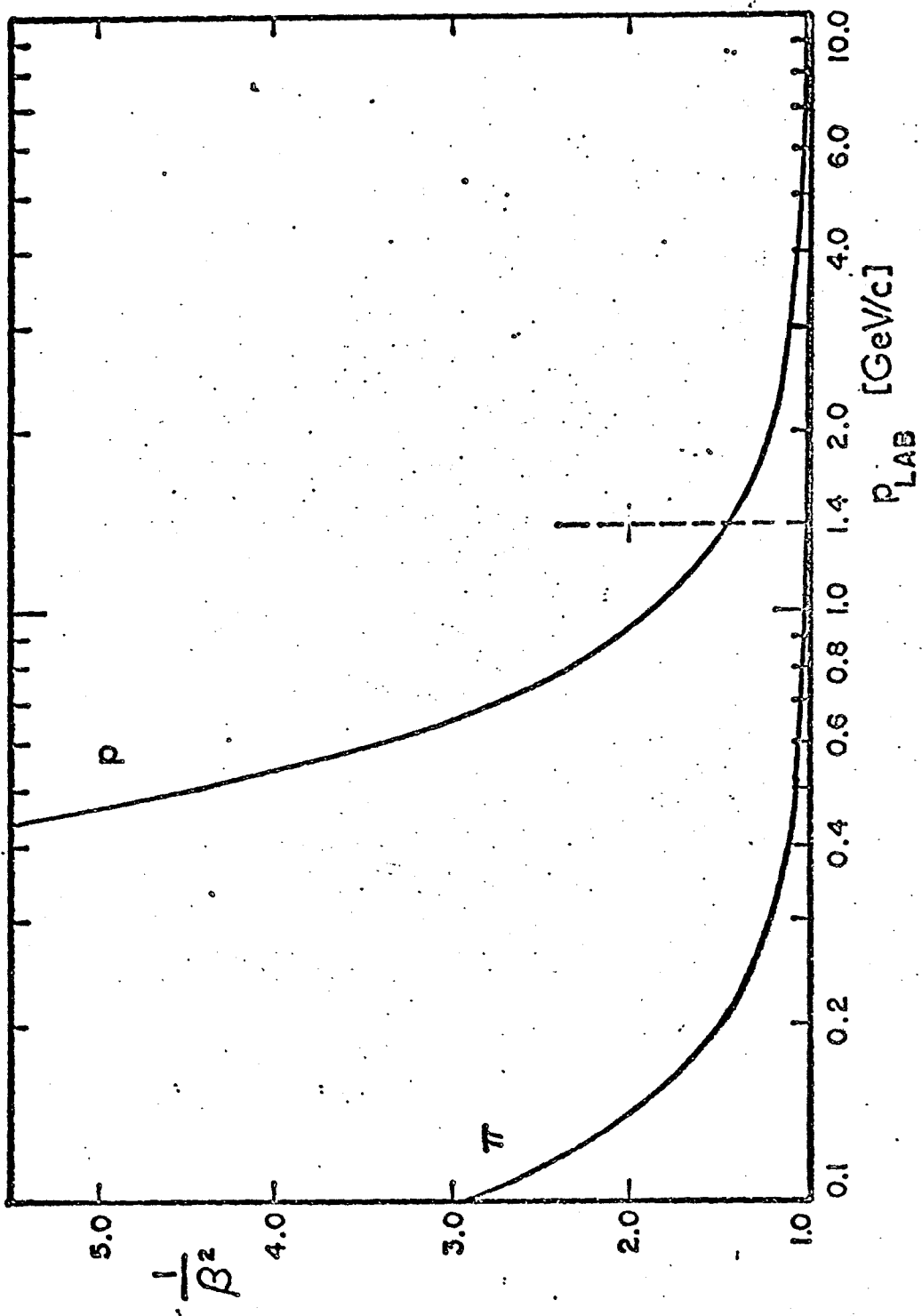
Fig. II.4.

bubble densities will also differ by 45%, this being considered the minimum recognizable difference. Stopping tracks were assumed to be protons and scattering tracks were identified by a combination of ionization and telltale signs such as a $\pi-\mu-e$ decay. In the exclusive event sample, tracks with momenta greater than 1.4 GeV/c were assumed to be pions except where the best 4-constraint fit determined the particle to be a proton. The kinematic fits always found the fastest positive particle to have the same identity as the beam, in agreement with the leading particle effect.[8] Details of the ionization determination and strange particle contamination are given in App. E.

2. Proportional Wire Chamber

In each spill (frame), several time slots are set up by the passage of beam tracks through scintillators S_1 and S_2, each slot having a set of wire hits in the upstream and downstream chambers. The Proportional Wire Geometry Program (PWGP)[9] finds the minimal set of space points that will produce the observed wire hits in each chamber for each time slot. As the wire chambers are outside the magnetic field, straight tracks are reconstructed through the space points. Using the nominal beam momentum value found by the program SURVEY (see App. B), beam tracks are swum into the bubble chamber and if possible, connected with a particular bubble chamber vertex. Associated with each beam track is the Čerenkov information so that each bubble chamber event connected with a PWC beam track has the beam particle identified (tagged).

The downstream tracks reconstructed in the time slot which is associated with the event are also swum to the connected vertex, the best fit yielding the momenta for these tracks. Both upstream and downstream reconstructions are done only for the exclusive event sample while the upstream tracks are reconstructed for beam tagging purposes for the remainder of the 100 GeV/c data samples.[10]

Testing of the program's reconstruction efficiency and accuracy was done in previous experiments with the same apparatus. Results are available in group memos and presented papers.[3,9,11] A Monte Carlo program was used to generate a fast track momentum distribution and the resulting wire hits. The hits were then reconstructed by the program PWGP and the results compared to the generated track. A 92% efficiency for proper reconstruction is quoted. Of the remaining tracks 4% failed due to high χ^2 values and another 4% failed to pass through more than 2 wire chambers. Most important, only 1/3% of all tracks were reconstructed with wrong momentum values. It was also found that for tracks passing through 3 or 4 chambers, $\Delta p/p$ was proportional to the momentum (.0006p with p in GeV/c) and that the spatial accuracy in the y and z directions was better than .5 mm.

F. Beam Track Tagging

Before any 100 GeV/c data could be analyzed, the topological cross sections for the different beam particle types had to be

obtained. This required that in a significant sample of the data, all events had to have their beam track and vertices measured so that they might be tagged and separated into proton and pion samples, whether or not they satisfied the measurement criteria.

The PWGP and BUATAG[10,11] programs provided the tagging in the 100 GeV/c data sample. In short, given a nominal beam momentum, the programs swim PWC upstream tracks to bubble chamber vertices. If the PWC beam passes with 1.5 mm of a vertex, the beam is associated with that bubble chamber event and its Čerenkov information gives the mass identity. Tagging efficiencies for both events treated by PWGP and BUGTAG are given in Table II.3. From Table II.3, it is seen that the tagging efficiency is independent of the event multiplicity as expected. The BUGTAG efficiency for RUN 1 is higher than the PWGP efficiency because the criteria for beam track reconstruction and vertex matching were loosened for the inclusive event sample.

G. Track Organizing

In order to improve fast track momenta before trying kinematic fits with SQUAW, bubble chamber tracks and downstream PWC tracks must be matched and the data combined to give a best fit. A track organizing program[12] (TRKORG) was written by the PHS Consortium for this purpose.

The program proceeds in two steps. All PWC tracks are swum to their bubble chamber vertices and projected onto the film plane. The y-coordinate values of the swum PWC track are then

TABLE II.3

DATA	N	EVENTS	EV TAGGED	EFF (%)
RUN 1 − BUGTAG	≥2	11499	10234	89
RUN 3 − BUGTAG	≥3	5949	4551	77[*]
RUN 1 − PWGP	3	662	520	79±2
RUN 1 − PWGP	4	1320	1034	78±1
RUN 1 − PWGP	5	819	629	77±1
RUN 1 − PWGP	6	1237	986	80±1

[*] Many rolls were unsalvageable due to total Čerenkov failure and are omitted from the efficiency calculation.

compared with the y-values of the bubble chamber track at the beginning, middle and end of the track in each view. The root mean square sum of the y differences in each view, the residue, is then calculated and if less the 50 μ, the tracks are matched for that view. This process discards tracks from secondary interactions or interactions in the chamber walls that go through the downstream wire chambers, but will sometimes have multiple bubble chamber-PWC matches. Ambiguities are removed by an algorithm which favors pairs of tracks that match in all three views, and then the lowest values of the sum of the squared residues.

A 13 parameter least-squares fit is then done to determine the three momentum of the track. As the resultant momenta are greater than 10 GeV/c, the fit is mass independent. The 13 variables fit are the 9 residues, and the y and z coordinates and slopes at the master chamber, PWC D. Appropriate error values are also calculated for each track and the output is written in a format compatible with SQUAW input.

The efficiency for matching PWC and bubble chamber tracks with common vertices depends on the definition of what kind of track should be track organizable ("fast"). The PHS is designed to accept all tracks with a momentum greater than 20 GeV/c in the laboratory, through all four downstream chambers. A 20 GeV/c track within the geometric acceptance of the fourth chamber may then be defined as "fast".[13] In Fig. II.5, the efficiency of the TRKORG program for successfully handling "fast" tracks is shown.
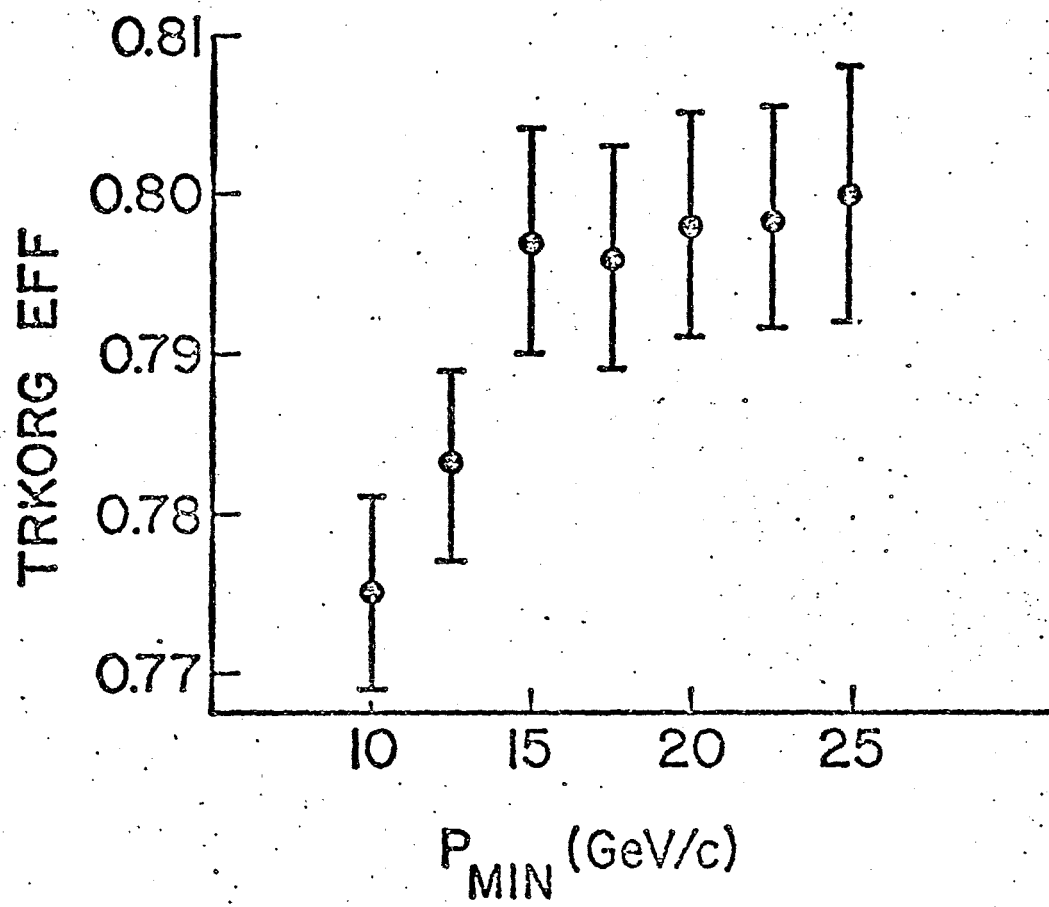
Fig. II.5

Note the constant efficiency above 15 GeV/c. An angle cut-off of 37 mr between the outgoing track and the x-axis is made.

The topology for exclusive reactions $I_.3$a should contain only one beam-like particle if it is mostly a target dissociation reaction, implying that Fig. II.5 shows the TRKORG efficiency correction that must be applied in calculating those cross sections. The coherent reactions in Eq. $I_.3$b could contain as many as three "fast" particles from beam dissociation, the efficiency for these reactions being at best the single track efficiency cubed. This low efficiency combined with the large momentum an invisible deuteron may carry and poor statistics, makes a quantitative cross section calculation for coherent events unreliable. Table II.4 presents the TRKORG efficiency as a function of the number of "fast" tracks in 3-4 prong events, and the number of tracks track organized (hooked-up).

Errors – the errors assigned by TRKORG are smaller than either PWGP or TVGP errors alone. The angular resolution is best for tracks passing through all four downstream wire chambers, and the fractional error on momentum, $\Delta p/p$, is proportional to the momentum. See App. E.

Calibration – To test the accuracy of the TVGP – PWGP – TRKORG system we measure non-interacting beam tracks and divide the track into two parts, creating a phony vertex. For simplicity in programming, we generate a fake straight track at the vertex, defined by the vertex and a fiducial mark, and process the data as

TABLE II.4

N_{FAST}	$N_{HOOK-UP}$	EFF (%)
1	1	80.2 ± 1.0
2	1	78.0 ± 1.9
2	2	60.0 ± 2.2
3	1	65.8 ± 4.4
3	2	61.5 ± 4.5
3	3	25.6 ± 4.0

a 2-prong event. The part of the beam track downstream of the vertex is then a fast forward track passing through the wire chambers and should have wire chamber and bubble chamber data merged. By varying the location of the vertex, and purposely misaligning the two coordinate systems by rotating and translating the output from FIDROT, we test the sensitivity of the processing system to coordinate alignment for various track lengths. Appendix E gives the full results of this study.

For a vertex at the center of the bubble chamber the average momentum for the downstream beam track is $99.8 \pm .5$ GeV/c . This may be compared with the $97.7 \pm .4$ GeV/c as determined by the SURVEY program in Appendix A. The 5 GeV/c width of the distribution is also roughly equivalent to the error in momentum for fast tracks with momenta of 85 to 115 GeV/c. Both of the above facts lead us to believe that the processing system is well calibrated. For more details see App. E.

H. Data Handling

PHS information was written by a PDP-11 computer onto tape in a Fortran-compatible format. This tape was reformatted and then read directly by PWGP or BUGTAG concurrently with reformatted TVGP output. The TVGP output for the exclusive sample of events was the standard binary record, which also served as SQUAW input. For the inclusive slow track sample and the exclusive sample, an abbreviated Data Summary Tape was made, including all ionization information.

REFERENCES

1) See Appendix B for the beam determination by the program SURVEY.

2) Much thanks to Bill Bugg for providing this efficiency programing and on adapting other existing software.

3) T. Ludlam, P.H.S. Consortium Newsnotes 19 and 19a (Yale University, 1972);

   D. G. Fong, Phys. Lett. 53B, 290 (1974).

4) D. A. Evans and W.H. Barkas,Nuc.Inst. and Meth. 56, 289 (1967).

5) F.T. Solmitz, A.D.Johnson and T.B. Day, "Three View Geometry Program", 2nd Ed. (Alvarez Programming Note p-117, U. of Calif.-Lawrence Rad. Lab., Berkeley,1966).

6) O.I. Dahl, T.B. Day, F.T.Solmitz, N.L.Gould, "SQUAW Kinematic Fitting Program" (Group A Programming Note P-128, U. of Calif.-Lawrence Rad. Lab., Berkeley,1968).

7) D.M. Ritson ed., "Techniques of High Energy Physics" (Interscience Publishers, New York,1961);

   R.P.Shutt ed., "Bubble and Spark Chambers", Vol. 2 (Academic Press, New York,1967).

8) M.L. Perl,"High Energy Hadron Physics" (John Wiley and Sons, New York,1974).

9) D.Fong, T. W. Ludlam and T.L. Watts, "Secondary Tracks in Multi-wire Proportional Counters at the NAL 30" Bubble Chamber", PHS Note (1973).

   This is an update of the talk BD13 given at the A.P.S. Meeting

in Washington, D.C. April 1973.

10) Bill Bugg modified the full PWGP program for this purpose and
it has been appropriately become known as BUGTAG.

11) W.M. Bugg, "Utility Programs and System Performance Experiment
154" (University of Tennessee, 1974).

12) D.G. Fong, P.H.S. Consortium Newsnotes 37, 38 and 39
(Brown University, 1975).

13) We include angular cuts for geometric acceptance in the x-y
and y-z planes because TVGP track momenta are unreliable above
10 or 15 GeV/c.

III. TOTAL AND TOPOLOGICAL CROSS SECTIONS

Presented in this chapter will be the results of the 100 GeV/c multiplicity analyses[1,2] and new results[3] from the 400 GeV/c data sample in Section II.D. Details of the scanning corrections to produce the corrected event samples may be found in Appendix D. Total and topological cross sections for hd and hn reactions will be measured for use in subsequent analyses.

A. Scan Corrections

Experience with scan corrections[2] at 100 GeV/c has shown us that the proton stub visibility becomes multiplicity independent for stub lengths greater than 5 mm (120 MeV/c for a proton). While the correction for missed stubs was made in a multiplicity dependent manner at 100 GeV/c, for simplicity in the new data we will define any countable even N-prong event to be an N-1 odd-prong if it has a stub less than 5 mm in length. The uncountable events should then be redistributed, as in Section II.D, to reflect the new odd-prong probability f_o, where now $f_o \approx 0.27$, scanned 1- and 2-prong events being included in the calculation of this value. This raw event sample is corrected for missed Dalitz pairs, close vees, close converting photons and close secondary interactions. The corrected event samples for odd-plus-even hd events are given in Table III.1 and the odd multiplicity events in Table III.2. Both pd and odd distributions at 400 GeV/c are given in Table III.3.

TABLE III.1

	pd 100 GeV/c		π^+d 100 GeV/c	
N	CORRECTED EVENTS	$\sigma(N)$ mb	CORRECTED EVENTS	$\sigma(N)$ mb
4	1576 ±41	12.81 ±0.58	676 ±27	7.57 ±0.48
6	1732 ±43	14.08 ±0.63	742 ±28	8.31±0.51
8	1439 ±40	11.70 ±0.54	672 ±28	7.53 ±0.48
10	943 ±33	7.67 ±0.39	402 ±22	4.50 ±0.33
12	538 ±25	4.37 ±0.26	262 ±18	2.93 ±0.25
14	248 ±18	2.02 ±0.16	121 ±13	1.36 ±0.16
16	126 ±13	1.02 ±0.11	48 ±8	0.54 ±0.09
18	29 ±7	0.24 ±0.06	14 ±5	0.16 ±0.06
20	9 ±3	0.07 ±0.02	6 ±3	0.07 ±0.03
22	2 ±1	0.02 ±0.01	2 ±1	0.02 ±0.01
24	1±1	0.01 ±0.01	1 ±1	0.01±0.01
TOTAL	6643	54.00±2.00	2946	33.00 ±1.60

TABLE III.2

100 GeV/c

N	CORRECTED pd ODD	CORRECTED π^+ d ODD
3	469 ±24	201 ±16
5	550 ±26	242 ±17
7	458 ±24	216 ±16
9	307 ±19	127 ±13
11	173 ±15	91 ±11
13	81 ±11	45 ±7
15	30 ±7	22 ±5
17	8 ±4	2 ±2
19	4 ±2	1 ±1
21	2 ±1	1 ±1
23	1 ±1	———
TOTAL	2083	948

TABLE III.3

400 GeV/c

N	CORRECTED ODD EVENTS	CORRECTED pd EVENTS	$\sigma(pd,N)$ mb
3 4	930±33	2518±62	7.69±0.22
5 6	1005±37	2941±74	8.98±0.26
7 8	1100±40	3245±80	9.91±0.29
9 10	1037±39	3056±81	9.34±0.28
11 12	835±37	2460±76	7.51±0.26
13 14	553±31	1685±66	5.15±0.22
15 16	387±28	1148±57	3.51±0.18
17 18	227±23	674±49	2.06±0.15
19 20	118±18	399±41	1.22±0.13
21 22	70±14	224±31	0.68±0.10
23 24	15±9	102±23	0.31±0.07
25 26	14±7	63±16	0.19±0.05
27 28	3±2	21±9	0.064±0.028
29 30	1±1	5±3	0.015±0.009
31 32	———	6±4	0.018±0.012
33 34	———	———	———
35 36	———	1±1	0.003±0.003
ODD TOTAL	6295	———	———
pd TOTAL	———	18548	56.7±0.80

B. Total and Topological hd Cross Sections

At 100 GeV/c[1], the total cross sections in deuterium for events with 3 or more prongs were (54.00±2.00) mb and (33.00±1.60) mb for pd and π^+d respectively. A sample of 44,000 pictures was used to determine the cross section at 400 GeV/c. On 33,236 acceptable frames in this sample, 16,341 raw events were found in the fiducial volume projected on the scan table. The target density was determined to be (0.1364±0.0007) g/cm^3 from the thermodynamic operating conditions of the chamber. The cross section and the fractional error are defined in Eq. III.1.

$$\sigma(N \geq 3) = (\# \text{ events } N \geq 3) \cdot (\text{mb/event}) = E/(B \cdot C) \qquad \text{III.1a}$$

$$(\delta\sigma(N \geq 3)/\sigma(N \geq 3))^2 = (\delta E/E)^2 + (\delta B/B)^2 + (\delta C/C)^2 \qquad \text{III.1b}$$

E is the corrected number of events with more than 3 prongs in a true 3-dimensional fiducial volume, B the number of beam particles incident on that volume, and C the number of scattering centers (deuterium nuclei) per cm^2 seen by a beam incident on the volume.

The real number of events and the error are calculated using Eq. III.2a and .2b.

$$E = S \cdot (f/\epsilon) \cdot v \qquad \text{III.2a}$$

$$(\delta E/E)^2 = (\delta S/S)^2 + (\delta f/f)^2 + (\delta \epsilon/\epsilon)^2 + (\delta v/v)^2 \qquad \text{III.2b}$$

where S is the total number of raw events with 3 or more prongs
seen in the scan fiducial volume, ε the scanning efficiency for
finding $N \geq 3$ prong events, f the fraction of events in the spatial
fiducial volume and v the fraction of events which really have 3 or
more prongs. The particles incident on the fiducial volume are
calculated using Eq. III.3.

$$B = B_c \cdot (F_s/F_c) \qquad\qquad \text{III.3a}$$

$$(\delta/B)^2 = 1/B_c \qquad\qquad \text{III.3b}$$

Here B_c is the number of beam particles counted (we count approxi-
mately every tenth frame), F_s the number of scannable frames and F_c
the number of frames in which beam particles were counted. The
number of scattering centers per cm^2 seen by the beam is $1/\sigma_T(pd)$
corrected for beam attenuation through the fiducial volume as given
in Eq. III.4a.

$$C = \left[1-\exp(-G) \right] / \sigma_T(pd) \qquad\qquad \text{III.4a}$$

where

$$G = \sigma_T(pd) \cdot L \cdot N_o \cdot \rho/A \qquad\qquad \text{III.4b}$$

L is the fiducial volume length, $\sigma_T(pd)$ is the total pd cross section[4],
N_o Avogadros's number, ρ the target density, and A the atomic weight

of deuterium. The fractional error in C is given by Eq. III.4c.

$$(\delta C/C)^2 = \left[G \cdot \exp(-G) \: / \: (1-\exp(-G)) \, \right]$$

$$\left\{ \left[1 - (C \cdot \sigma_T / \: G \: \exp(-G) \:) \right]^2 (\delta\sigma_T/\sigma_T)^2 + (\delta L/L)^2 \right.$$

$$\left. + (\delta\rho/\rho)^2 \right\} \qquad\qquad\qquad \text{III.4c}$$

In Table III.4, values for all parameters are given for the 12 rolls of film scanned by Stony Brook, with errors where applicable. For this data, $\sigma(pd, N \geq 3) = (56.91\pm1.01)$ mb. For the Carnegie-Mellon data available, $\sigma = (56.1\pm1.5)$ mb and taking a weighted average of the two, we find $\sigma = (56.7\pm0.8)$ mb. This cross section may be compared with published values at 100 GeV/c and 200 GeV/c[5] of (54.00 ± 2.00) mb and (55.1 ± 0.8) mb respectively. The odd-plus-even hd cross sections normalized to the appropriate $\sigma(hd, N \geq 3)$ are presented in Tables III.1 and III.3.

C. "Free Neutron-hn" Cross Sections

To first order, the corrected odd-prong multiplicity distribution should be an unbiased sample of neutron target events if the impulse approximation (App. G) is valid. Differences between the odd-prong and neutron distributions arise from coherent interactions (h + d → d + X), symmetry requirements on the final state wave-function[6] and rescattering (App.G), where both nucleons are involved in the interaction with subsequent deuteron break-up. Lys[2] derives Eq. III.5

TABLE III.4

TOTAL CROSS SECTION PARAMETERS

PARAMETERS	VALUES
s	11504 ± 107.26
f	0.9804 ± 0.0040
ϵ	0.99 ± 0.01
v	0.9992 ± 0.0003
E	11383 ± 163
B_c	11539 ± 107.41
F_s	23596
F_c	2333
B	116706 ± 1086
$\sigma_T(pd)$ (Ref. 4)	75.49 ± 0.08 mb
L	45.00 cm
N_0	6.0221×10^{-4} cm^2/mb
ρ	0.1364 ± 0.0007 gm/cm^3
A	2.0141
C	$1.7138 \pm 0.0084 \times 10^{-4}$ cm^{-2}

to extract the inelastic hn cross sections from the odd-prong events.

$$\sigma\ (hn,N) = K\left[\sigma(hd,N) - (f_d - 0.35\ f)\right.$$

$$\left.\cdot\ \sigma\ (hd,\ d + N)\right]\qquad\qquad III.5$$

N is defined to be odd, f to be the probability of a spectator proton to be invisible, f_d the corresponding probability for the final-state deuteron, and $\sigma(hd, d + N)$ the $(N + 1)$ - prong coherent deuteron cross section. In the derivation, it is assumed that rescattering and Glauber screening effects are multiplicity independent.[7] K normalizes the sum over all topologies to the inelastic hn cross section.

The hadron-neutron cross sections are presented in Table III.5 for both 100 and 400 GeV/c data. At 100 GeV/c, we use the measured pn total cross section[8] and assume the ratios of the elastic to total cross sections[4,9] for pp and pn to be equal, to arrive at our pn results. Invoking charge symmetry and using $\pi^- p$ data[4,9] as above, we obtain the $\pi^+ n$ cross sections. Corresponding to the 2 mm visibility cut-off made in the 100 GeV/c data, f=0.64 and f_d = 0.54. For the 400 GeV/c cross sections, we assume the inelastic pp[10,11] and pn cross sections to be equal with an additional 2% uncertainty in $\sigma_{IN}(pn)$, and use f and f_d equal to 0.76 and 0.75 respectively, matching the 5 mm visibility cut-off. Our $\sigma_{IN}(pn)$ may be compared with a value of (31.5±.3) mb extracted from data with neutron beams

TABLE III.5

hn CROSS SECTIONS

	100 GeV/c		400 GeV/c
N	σ(pn,N) mb	σ(π⁺n,N) mb	σ(pn,N) mb
1	2.81±0.50	1.17±0.25	1.62±0.40
3	6.17±0.37	3.88±0.38	3.82±0.23
5	7.73±0.37	5.00±0.36	4.96±0.29
7	6.53±0.34	4.55±0.34	5.66±0.29
9	4.38±0.27	2.69±0.28	5.33±0.27
11	2.47±0.21	1.93±0.23	4.29±0.24
13	1.15±0.16	0.95±0.15	2.84±0.19
15	0.43±0.10	0.47±0.11	1.99±0.16
17	0.11±0.06	0.04±0.04	1.17±0.13
19	0.06±0.03	0.02±0.02	0.61±0.10
21	0.03±0.01	0.02±0.02	0.36±0.07
23	0.01±0.01	———	0.077±0.046
25	———	———	0.072±0.036
27	———	———	0.015±0.010
29	———	———	0.005±0.005
TOTAL	31.88±0.44	20.72±0.15	32.8±1.2

incident on polyethelene (CH) and carbon (C) presented by T. Roberts.[12]
The cross section for reactions with a deuteron in the final state at
400 GeV/c are assumed to be equal to those values extracted[7] at
100 GeV/c from the p + d → d + X data available.[13]

The impossibility of scanning, measuring and fitting 1-prong
events requires us to make an estimate of the N=1 inelastic hn cross
sections. Using the appropriate same CM energy cross sections, pn
(π^+n) cross sections may be related to the pp (π^-p) cross sections via
the following set of equations[2], where N is defined as even.

$$\sigma(pn, N + 1) = (1 - X_N) \sigma (pp, N) + X_{N+2} \sigma(pp, N + 2) \qquad \text{III.6a}$$

$$\sigma(\pi^+n, N + 1) = (1 - Y_N) \sigma (\pi^-p, N) + Y_{N+2} \sigma(\pi^-p, N + 2) \qquad \text{III.6b}$$

The quantities X_N and Y_N may be interpreted as the probability that a
struck proton in an N-prong hp interaction remains a proton or yields a
hyperon-positive kaon pair. At 100 GeV/c, X_N and Y_N were consistent
with being equal to 0.6 and independent of N for N $\geq$ 4, so we assume

$$\sigma(pn, N=1) = (0.6 \pm 0.1) \sigma(pp, N=2) \qquad \text{III.7a}$$

$$\sigma(\pi^+n, N=1) = (0.6 \pm 0.1) \sigma(\pi^-p, N=2) \qquad \text{III.7b}$$

where all the above cross sections are inelastic. (We expect
$\sigma(\pi^-p, N=0)$ to be negligible.) Summing over all multiplicities, the
average values of X_N and Y_N are

$$\langle X_N \rangle = 0.5 \ (\langle N \rangle_{pp} - \langle N \rangle_{pn}) + 0.5 \qquad\qquad \text{III.8a}$$

$$\langle Y_N \rangle = 0.5 \ (\langle N \rangle_{\pi^- p} - \langle N \rangle_{\pi^+ n}) + 0.5 \qquad\qquad \text{III.8b}$$

where the $\langle N \rangle$ are the average inelastic multiplicities. With the values of $\langle N \rangle_{pn}$ and $\langle N \rangle_{\pi^+ n}$ found in Table III.6 and $\langle N \rangle_{pp}$ and $\langle N \rangle_{\pi^- p}$ calculated from pp and $\pi^- p$ data, $\langle X_N \rangle = 0.6 \pm 0.1$ and $\langle Y_N \rangle = 0.61 \pm 0.08$ at 100 GeV/c. If Eq. III.7a is valid at 400 GeV/c, the 400 GeV/c pn and pp data yield $\langle X_N \rangle = 0.54 \pm 0.09$, certainly consistent with the lower energy value. Figures III.1, .2 and .3 graphically compare the topological pp ($\pi^- p$) and pn ($\pi^+ n$) cross sections normalized to unity. The 100 GeV/c pp data are a compilation of the results from Refs. 10, 14 and 15 and the 400 GeV/c data from Refs. 10 and 11.

D. Mean Multiplicities

From Table III.5, the multiplicity moments may be calculated for hn events. For the hd samples, a 2-prong inelastic cross section must be estimated. No high energy bubble chamber experiment has measured this cross section, because of the difficulty in detecting 1-prong events and in separating quasi-elastic events, pd → ppn for example, from production events like pd → ppnπ^o. The following estimate[7] is used

$$P(hd, \ N=2) = 0.5 \ \Big[P(hn, \ N=1) + P(hp, \ N=2) \Big] \qquad\qquad \text{III.9}$$
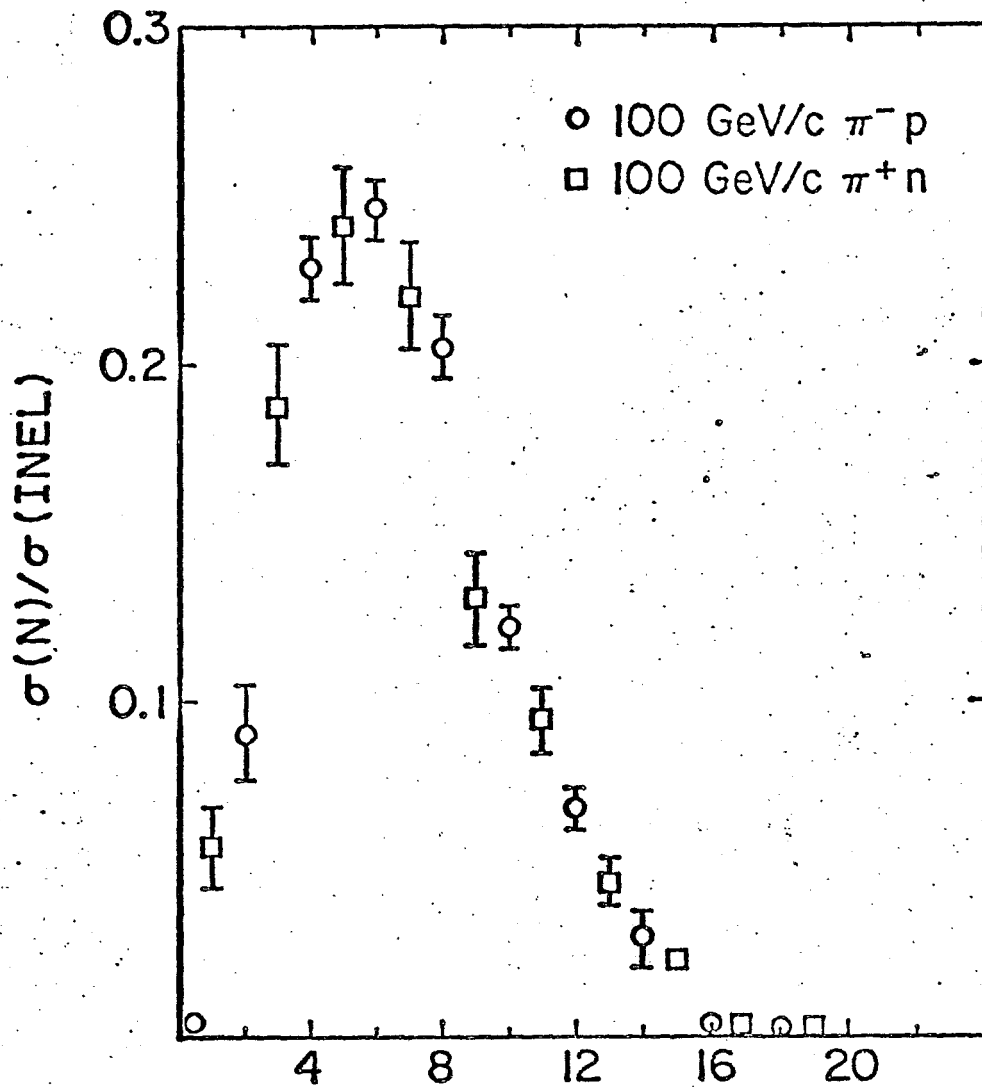
Fig. III.1
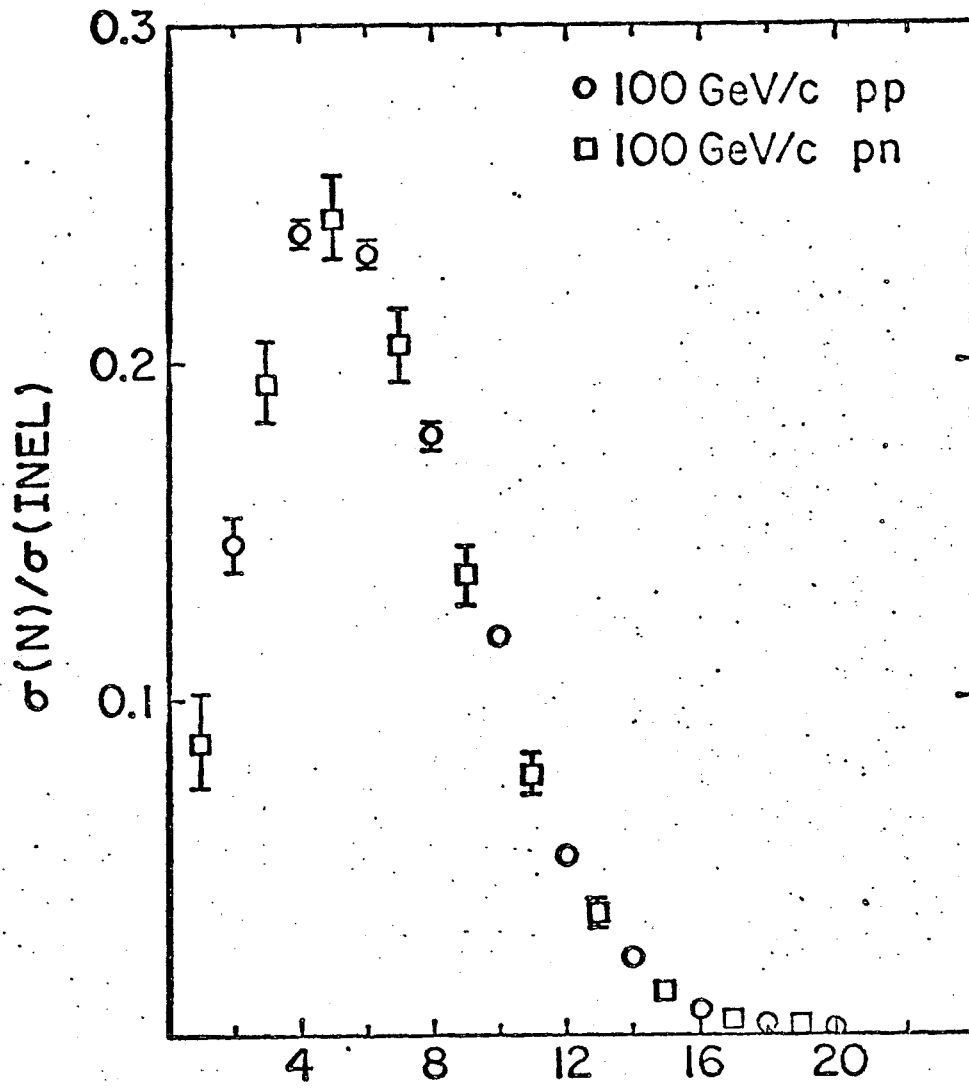
Fig. III.2
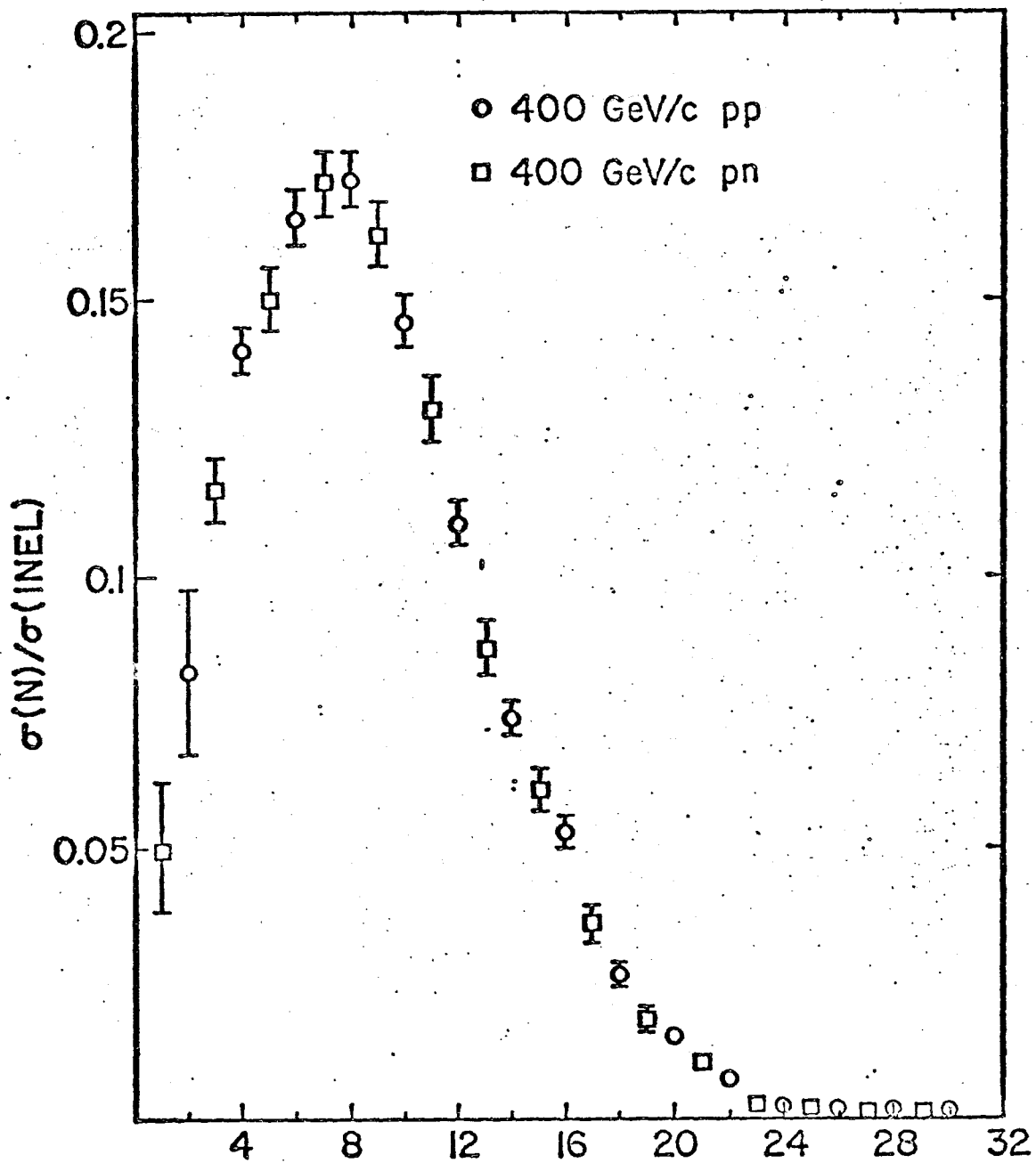
Fig. III.3

where P(hX, N=i) is the probability of having an inelastic i-prong collision, as in Eq. III.10.

$$P(hX,\ N=i)\ =\ \sigma(hX,\ N=i)\ /\sigma(hX,\ INEL) \qquad III.10$$

Eq. III.9 would be exactly true if the bubble chamber liquid were comprised of an unbound sea of protons and neutrons with equal cross section. Rescattering will cause a decrease in P(hd, N=2) but coherent effects might produce an increase. Use of a more complicated formula[16] taking these two effects into account yields the same results as Eq. III.9 within errors. Table III.6 presents the hn and hd multiplicity properties with the 1- and 2-prong cross section estimates, where D is the r.m.s. deviation and $f_2 = \langle N(N-1)\rangle - \langle N\rangle^2$, the second moment.

TABLE III.6

	100 GeV/c		400 GeV/c
	pd	π^+d	pd
$P(hd, N=2)$	0.117±0.010	0.075±0.080	0.066±0.013
$\langle N \rangle$	7.05±0.11	7.29±0.12	9.49±0.11
D	3.43±0.05	3.42±0.07	4.87±0.07
f_2	4.70±0.42	4.41±0.53	14.20±0.70

	pn	π^+n	pn
$P(hn, N=1)$	0.088±0.015	0.056±0.012	0.050±0.012
$\langle N \rangle$	6.20±0.11	6.57±0.13	8.61±0.12
D	3.38±0.07	3.38±0.09	4.62±0.08
f_2	5.25±0.51	4.89±0.59	12.70±0.80
$\langle X_N \rangle$	0.59±0.06	———	0.61±0.09
$\langle Y_N \rangle$	———	0.61±0.08	———

REFERENCES

1. S. Dado et al., Phys. Lett. 60B 397 (1976).

2. J.E.A. Lys et al., Phys. Rev. D16, 3127 (1977).

3. S. Dado et al., Phys. Rev. D (submitted for publication).

4. The total pd cross section σ_T(pd) was obtained from the extrapolation of 23 to 280 GeV/c data fit to the form
$$\sigma_T = a + b\ln s + c\ln^2 s$$
A.S. Carroll et. al., Phys. Lett. 61B, 303 (1976).

5. T. Dombeck et al., Argonne Report No. HEP-PR-76-62 (1976).

6. N.W. Dean, Phys. Rev. D5, 2832 (1972).

7. J.E.A. Lys et al., Phys. Rev. D15 , 1857 (1977).

8. P.V.R. Murthy et al., Nucl. Phys. B92, 269 (1975).

9. D.S. Ayres et al., Phys. Rev. D15, 3105 (1977).

10. C. Bromberg et al., Phys. Rev. Lett. 31 1563 (1973).

11. W.S. Toothacker, Univ. of Mich. Report No. UMBC 77-77 (1977).

12. T. Roberts, Bull. Am. Phys. Soc. 23, 635 (1978).

13. Y. Akomov et al., Phys. Rev. Lett. 35, 763 (1975);
    Y. Akimov et al., Phys. Rev. Lett. 35, 766 (1975).

14. J. Erwin et al., Phys. Rev. Lett. 32, 254 (1974).

15. W. M. Morse et al., Phys. Rev. D15, 66 (1977).

16. J.E.A. Lys, Phys. Rev. D16, 2181 (1977).

IV. THE REACTION $h+d \to h+p+p+\pi^-$

In this chapter, we present results on the reaction

$$h+d \to h+p+p+\pi^- \qquad\qquad \text{IV.1a}$$

for measured data from RUN 1. We isolate this reaction by kinematic fitting using the program SQUAW. A simple kinematic program was developed to check the results of the SQUAW fits. The cross section for Reaction IV.1a, with $h=\pi^+$, is the first to be measured at Fermilab energies. From the fitted event sample, we will extract the cross section for the free neutron dissociation reaction

$$h+n \to h+(p\pi^-) \qquad\qquad \text{IV.1b}$$

using two different methods yielding identical results. The cross section for Reaction IV.1b will then be compared with measurements of the same or equivalent reactions at several energies. From the energy dependence of the cross section we may infer the possible dominant production mechanisms.

A. SQUAW Results

Only 3- and 4-prong events that were beam tagged and had at least one track organized track were used as input to SQUAW. Corrections for the beam tagging efficiency and track organizing efficiency will be made when calculating cross sections. Four-prong events were fit to the mass hypothesis in Eq. IV.1a using

all four outgoing tracks. For the 3-prong events, the

hypothesis was fit by inserting an unseen spectator proton track

with a momentum of $p_x = p_y = p_z = 0$ and momentum error of

$\Delta p_x = \Delta p_y = 30$ MeV/c and $\Delta p_z = 40$ MeV/c. The Δp's are

approximately the average momentum an unseen spectator would have.

The z-component is largest, reflecting the poorer momentum

detection of bubble chamber measurements in the z-direction. At

lower energies, e.g. below the 30 GeV/c limit at the Brookhaven

AGS, the 3-prong fitted events in deuterium experiments were

considered to be less reliable[7,15], due to the higher possible

contamination from unseen π^o's allowed by the momentum errors of

the unseen spectator. Our larger errors on very fast tracks negate

this qualitative difference between the 3- and 4-prong event

samples. The angles of the beam were calculated by the PWGP

program after the beam track was swum to the vertex, and a

magnitude of 97.7 GeV/c, the value determined by the program

SURVEY, was assigned. The error was set equal to .8 GeV/c,

which is 25% larger than the root mean square sum of the .4 GeV/c

error in the mean momentum, also calculated in SURVEY, and the .5%

engineering momentum bite.

In Fig. IV.1 we show the χ^2 probability for events fit by

SQUAW to Reaction IV.1a. Proton and pion beam events are plotted

together, as the kinematic variables ϕ, s and k for tagged beam

tracks and track organized secondary tracks are independent of

mass and the fits are therefore independent of hadron type h.
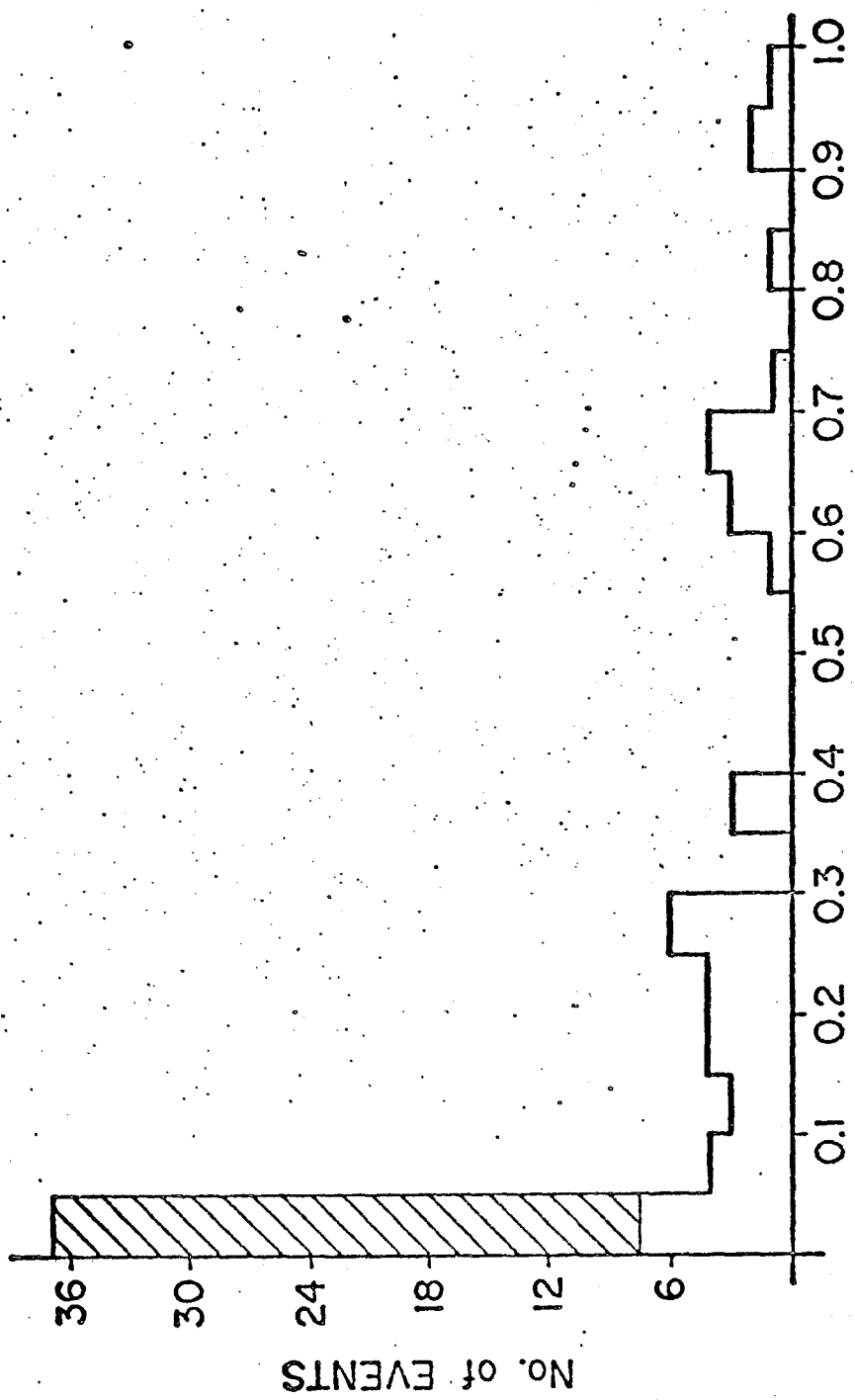
Fig. IV.1

Ideally, the χ^2 probability should be uniformly distributed. The shaded events in the lowest probability bin have a χ^2 probability less than 1% and we will use this value for our probability cut. After the cut, the probability distribution is still not quite uniform, and increasing the beam momentum error within reason (50%) did not remove the asymmetry. We did not change the errors for the secondary tracks because we believe that the error assignments as calculated by the TVGP – PWGP – TRKORG processing system are realistic. See App. E. Furthermore, we tested our SQUAW program by reproducing the fit results, on an event-by-event basis, from 147 GeV/c $\pi^- p$ data obtained from the Proportional Hybrid Consortium.[1,2] We therefore accepted these 44 events as the fitted event sample. Not included in the χ^2 probability plot are 4 events whose fitted mass hypotheses for tracks with a momentum less than 1.4 GeV/c did not match the ionization results. As the slow proton (not to be confused with the spectator proton) in 39 of the fitted events had a momentum of less than 1.4 GeV/c, this ionization check could be done for essentially the entire sample.

The Stony Brook and Fermilab fitted events were rescanned, double checking the ionization results for the slow tracks. Vees, converting photons and neutral particle interactions which could possibly be associated with the fitted event vertex were also searched for in this scan. None of these fitted events had any of the above associated.

B. Kinematic Cutting Program

An algorithm was developed to select events for Reaction IV.1a. It does not fit the track parameters and is therefore less sensitive to their error estimates. In being more simplistic than the SQUAW program, it is also more readily understandable. We found agreement between the results from this simple procedure and the kinematic fitting results of SQUAW. A detailed description of the algorithm follows:

In Section I.D, we discussed the fact that in our energy range, the cross section for Reaction IV.1a should be dominated by a diffractive production mechanism. Hence in most cases, the target will dissociate into a low mass system of particles, and the beam will exhibit the leading particle effect, i.e. it will keep its identity as a fast through-going track carrying a large fraction of the incident momentum. We therefore assign the fastest positive particle the mass of the beam particle. The remaining positive particles are assigned a proton mass hypothesis and the negative particle is assumed to be a pion. The proton with the smallest value of $\vec{p} \cdot \hat{x}$, where $\hat{x}$ is the beam direction, is chosen as the probable spectator proton in 4-prong events.

Three kinematic cuts

1) the "topology" cut

2) the "fragmentation" cut

3) the "transverse momentum balance" cut

are then made.

The topology cut requires an event to have a total momentum parallel to the beam ($p_{T_x} = \vec{p}_T \cdot x$) of at least 70 GeV/c (the beam momentum is 97.7 GeV/c), and insists that the event have an invariant mass squared (M^2_{vis}) for the visible particles, of at least 100 GeV^2, both p_{T_x} and M^2_{vis} being calculated from the detected final state particles. This M^2_{vis}-cut is well below the minimum s of 127 GeV^2 for a 97.7 GeV/c beam particle colliding with a neutron target having a momentum of 300 MeV/c in the beam direction. The cut reduces the 3-prong data by 63% and the 4-prong sample by 82%.

The fragmentation variable used had its origin in early cosmic ray experiments[3]. The variable $x_i \equiv (E-p_{//})_i/m_t$, the effective target mass fragment, is used where m_t is the mass of the target, E the energy of the ith particle, and $p_{//}$ the momentum of the ith particle in the beam direction. This is actually twice the Feynman scaling variable (see App.A.) calculated in the target rest frame for an infinite momentum beam. Using energy-momentum conservation we write

$$E_b + m_t = \sum_i E \qquad\qquad IV.2a$$

$$P_b = \sum_i P \qquad\qquad IV.2b$$

and by subtracting Eq. IV.2a from Eq. IV.2b, we get

$$Y_F \equiv \sum_i (E-p) = m_t . \qquad\qquad IV.3$$

if we have summed over all particles in the final state, including the spectator. We have also made the high energy approximation of $E_b \sim p_b$. The sum over all fragments x_i is equal to 1, but for our purposes, we can use Y_F to indicate how much of an event we have measured. Missing slow neutral particles will cause Y_F to be less than the target mass. (Fast neutral particles will hopefully be caught by our topology cut and the transverse momentum cut as yet to be made.)

For 3-prong events, Y_F should be the neutron mass, but it will be appreciably Fermi-smeared, so we require the absolute value of the difference $(Y_F - m_n)$ to be less than 220 MeV. In the 4-prong events, we presumably see the spectator proton and the target momentum is known. See App. G. We then use the difference $(Y_F - m_d)$, where m_d is the deuteron mass, and demand the absolute value be less than 140 MeV. Both the 3- and 4-prong cuts can be considered generous if we consider the Y_F distributions in Figs. IV.2 through IV.5. The maximum possible value for the 4-prong distribution is m_d, and the resolution of our measurement of Y_F for 4-prongs is then given by the high mass shoulder of the distribution in Fig. IV.4a, which is approximately 75 MeV wide. The same reasoning, applied to the 3-prong distribution in Fig. IV.2a, shows the resolution to be on the order of 125 MeV.

At this point, we can see that as well as requiring a fast particle system, the previous cut in M^2_{vis} selected only target fragmentation events. The unshaded events in Fig. IV.3 (before the

3-PRONGS

Fig. IV.2

3-PRONGS

Fig. IV.3

Fig. IV.4

Fig. IV.5

Fig. IV.2a

Fig. IV.4a
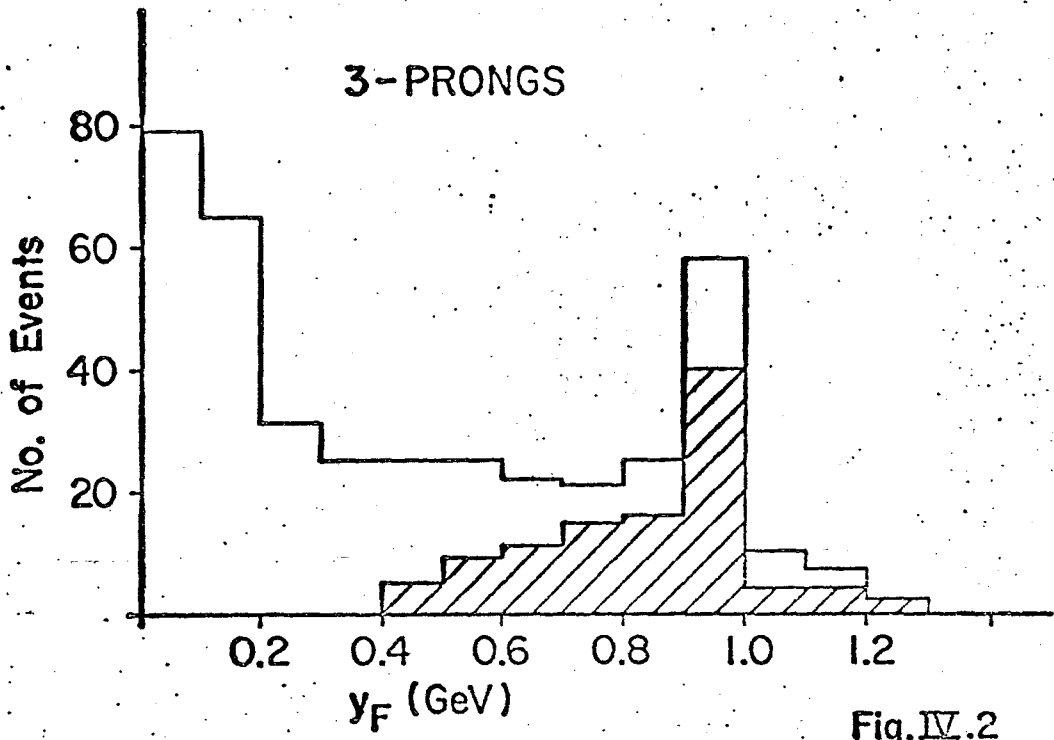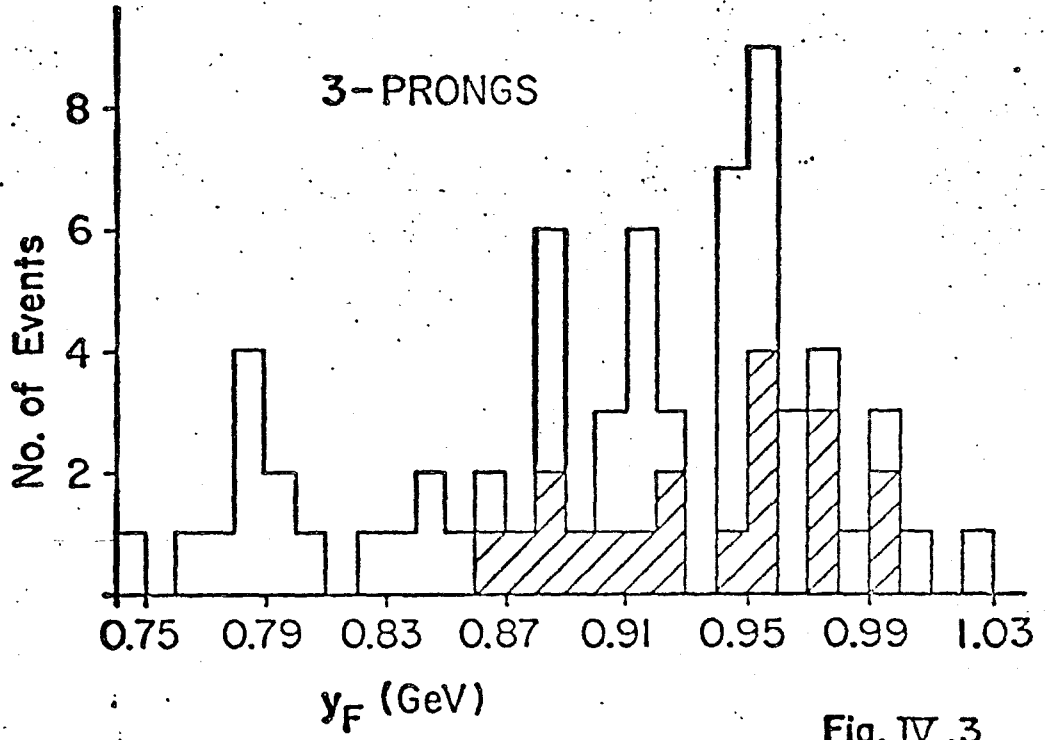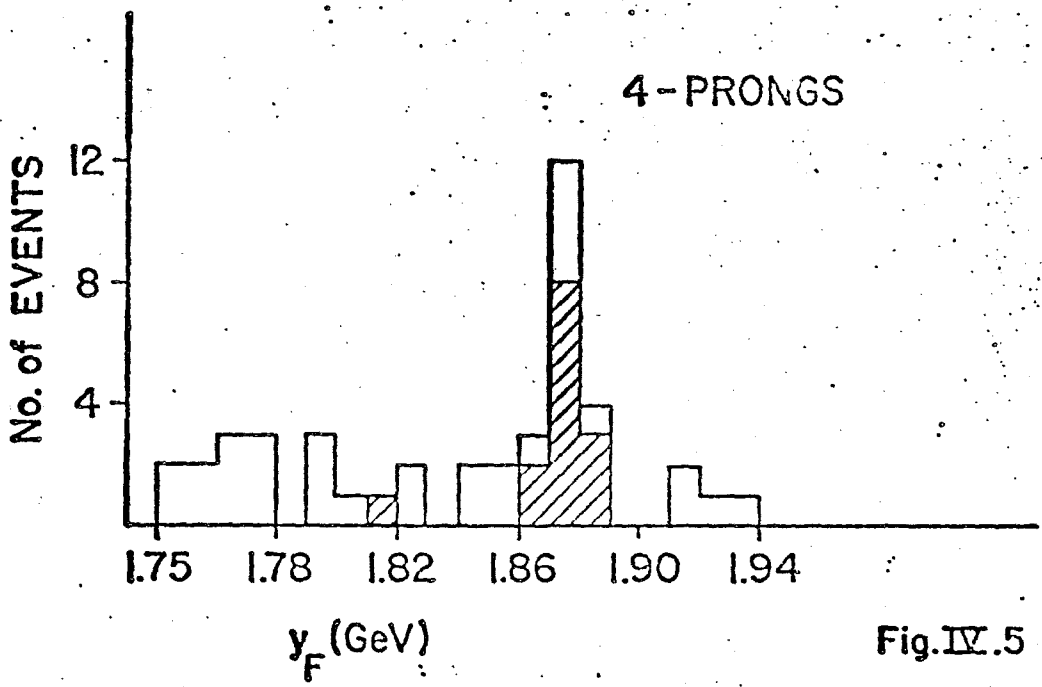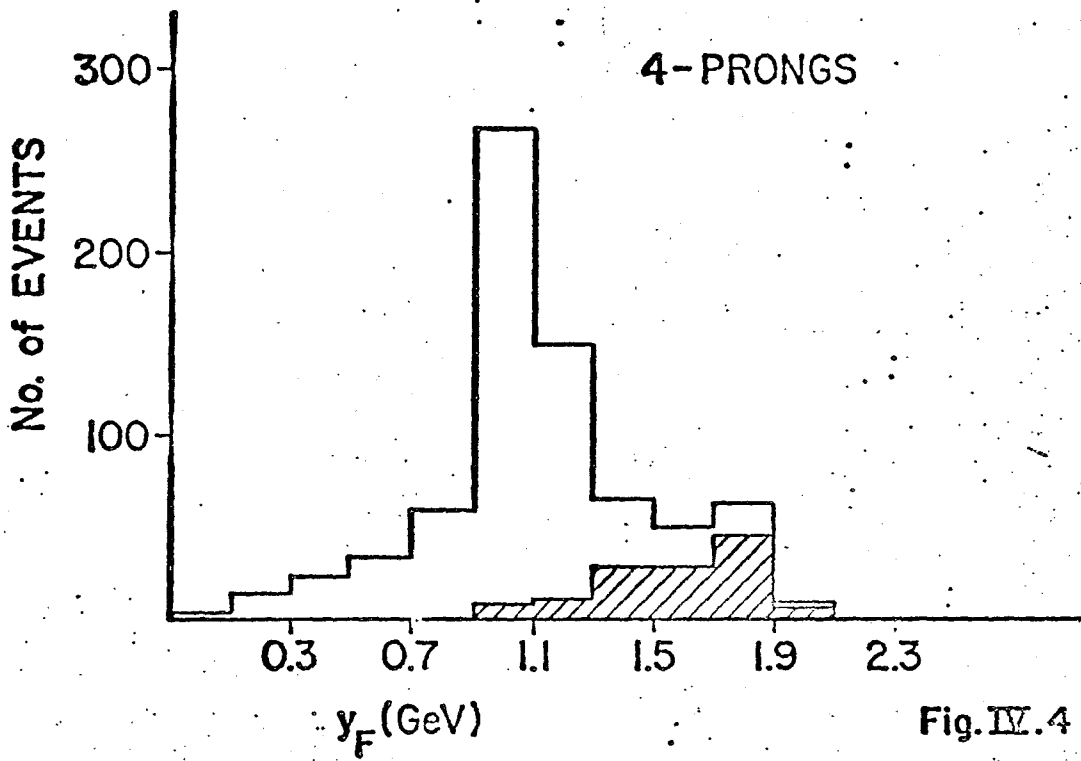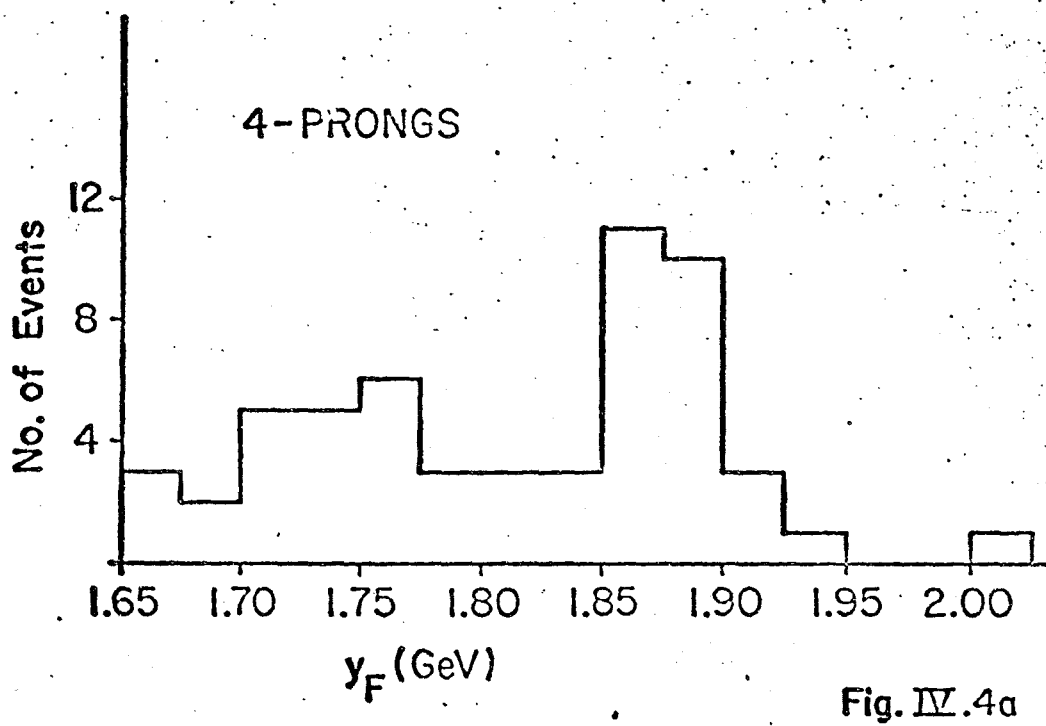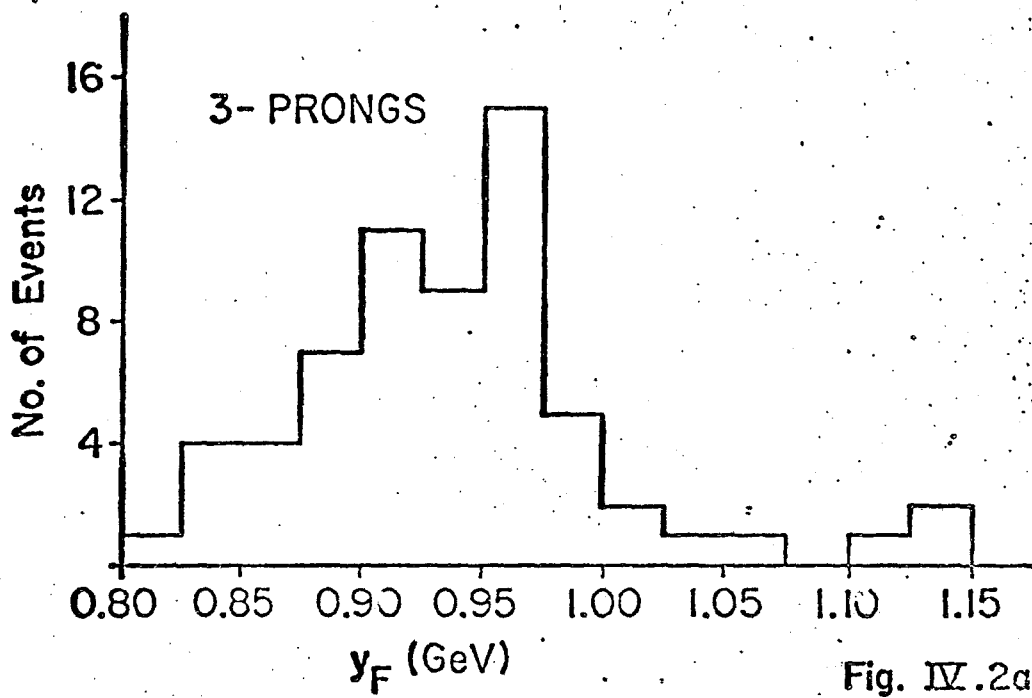
cut) show large spikes at $Y_F = 0$ (beam fragmentation) and at the
neutron mass (target fragmentation). The shaded histogram (after
the topology cut) shows no events in the beam fragmentation region,
as 3-prong beam fragmentation events, say pn → $(p\pi^+\pi^-)$n, have a
small value of s for the detected particles. In the 4-prong
distribution in Fig. IV.4, there is a pre-cut peak at the neutron
mass and a shoulder at the deuteron mass. The preponderance of
events at the neutron mass is caused by the large number of
proton target events measured at Carnegie-Mellon, and the 4-prong
neutron target (visible spectator) beam fragmentation events.
The s-cut is seen to enhance the deuteron shoulder.

The final cut is made on the transverse momentum imbalance
of the event, as calculated from the difference between the initial
state (beam plus target) and all observed final state particles.
Our transverse momentum resolution is much better than our
longitudinal momentum resolution. An event will be considered to
have conserved transverse momentum if the imbalance in transverse
momenta is less than our resolution. For the 3-prong events we use
a neutron target at rest in the LAB, and for the 4-prong events a
deuteron target. The cuts are made on p_{T_y} and p_{T_z}, the projections
of the total event momentum $\vec{p}_T$ on the y- and z-axes of the Beam
Coordinate System. In Figs. IV.6 through IV.11, we show the
resolutions Δp_{T_x}, Δp_{T_y} and Δp_{T_z} for 3- and 4-prong events separately.
For 3-prong events we require both p_{T_y} and p_{T_z} to be less than 120
MeV/c. The values used for the 4-prong events were 120 and 140
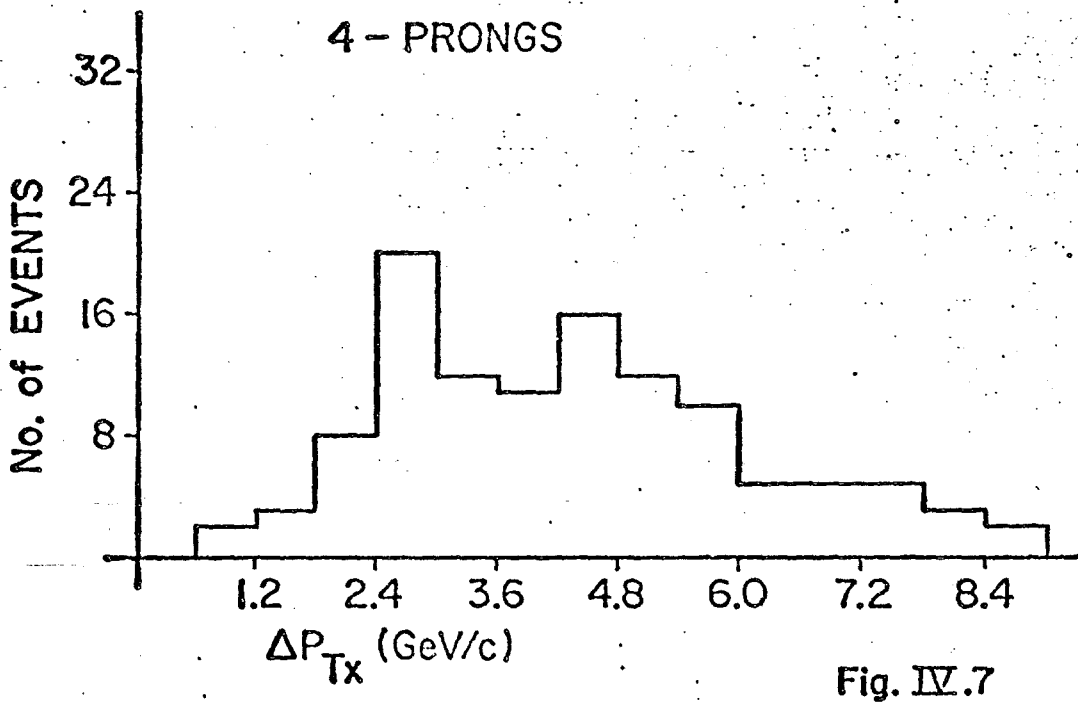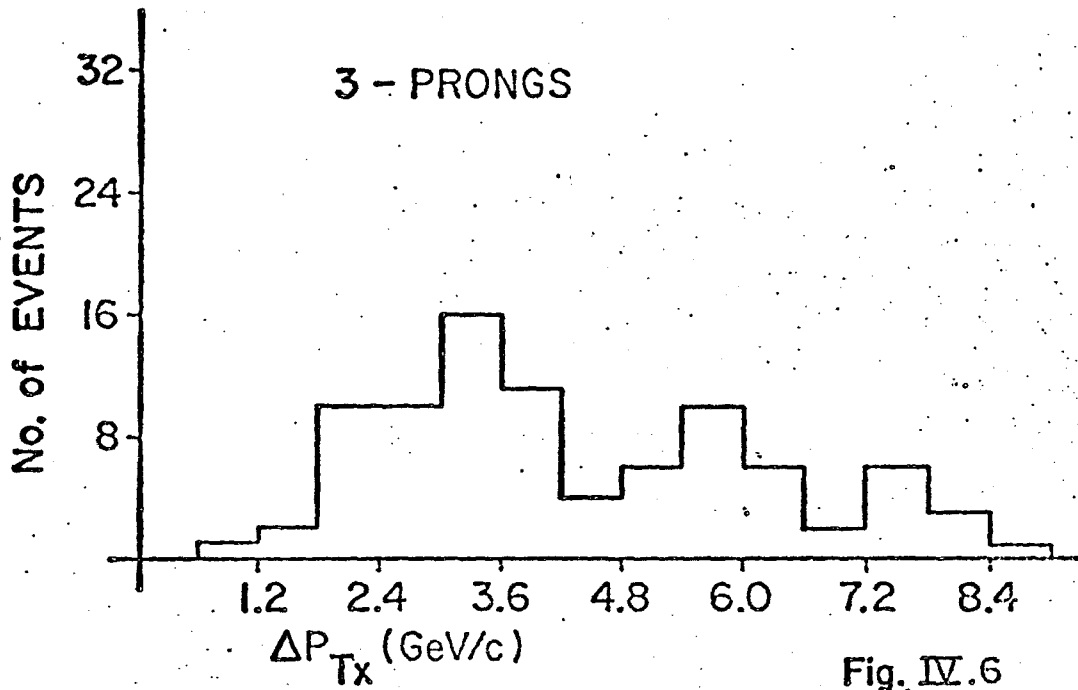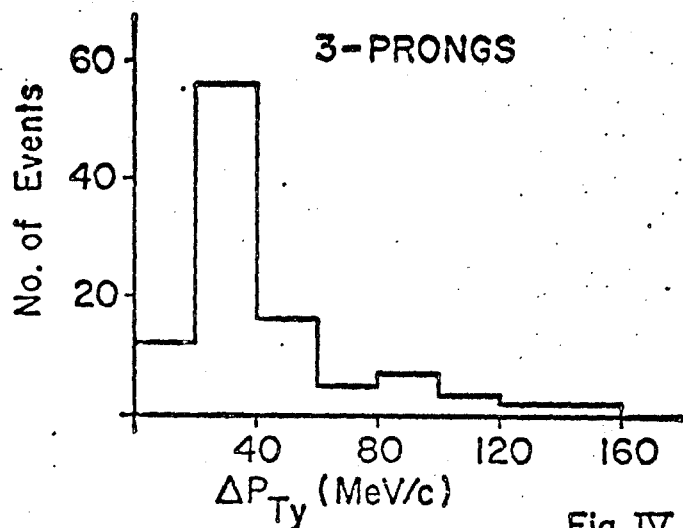
Fig. IV.6
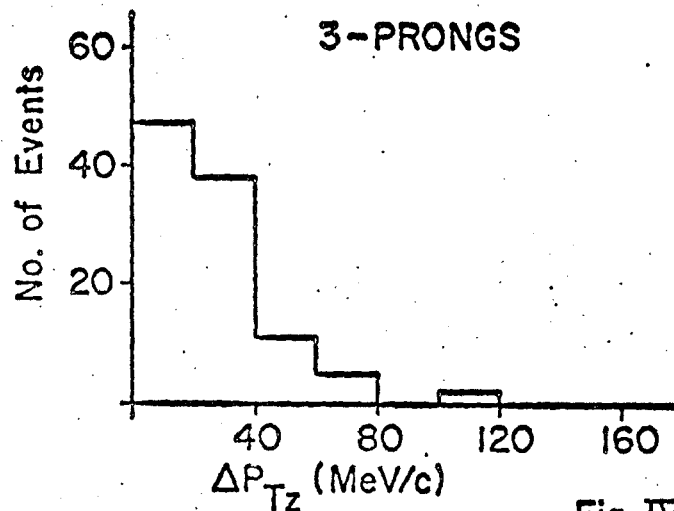
Fig. IV.7
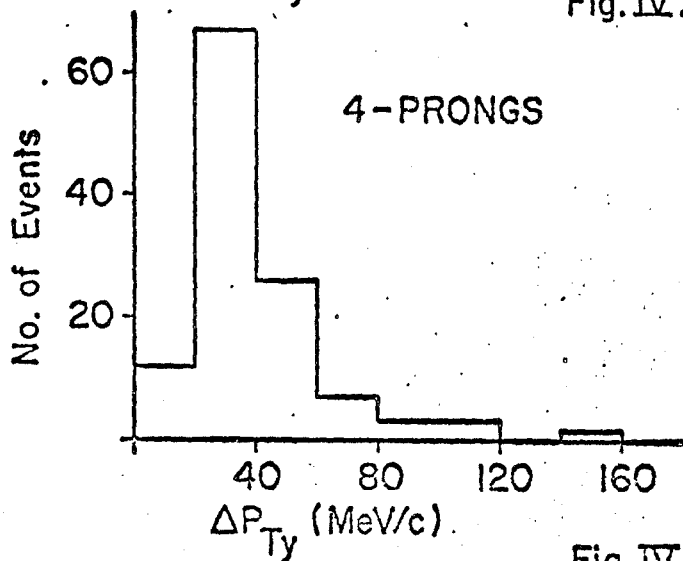
Fig. IV.8

Fig. IV.9

Fig. IV.10
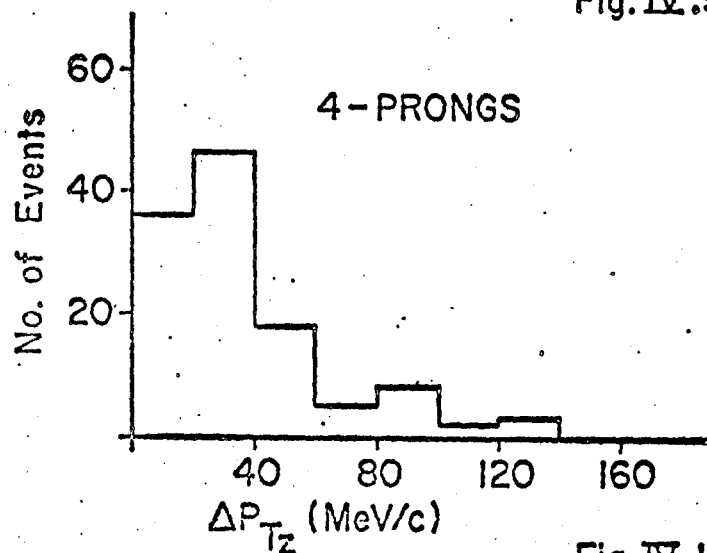
Fig. IV.11

MeV/c respectively. Figs. IV.3 and IV.5 show the Y_F distributions after the fragmentation cut (unshaded) and after the transverse momentum cut (shaded).

There is a distinct difference between the Δp_{T_y} and Δp_{T_z} distributions for both 3- and 4-prong events. One sees a sharper peak for Δp_{T_y} with very few entries in the lowest momentum bin. This is indicative of the dominance of the fast track errors from the TRKORG program. These fast tracks have a better z-component momentum resolution as discussed in Appendix E; hence the Δp_{T_z} has more entries below 20 MeV/c. The slight difference in Δp_{T_z} between 3- and 4- prong events can be accounted for if one considers that seen spectator protons are usually short stubs or high curvature tracks, and have a nearly symmetric distribution about the beam. See App. G. The projected track lengths are normally shorter than average secondary tracks, and the determination of the dip angle λ is poor. As p_z is roughly $p \cdot SIN\lambda$, the error in p_z, particularly for highly dipping tracks is large.

The missing mass squared for an event is defined in Eq. IV.4.

$$MM^2 = (\tilde{p}_b + \tilde{p}_t - \sum_i \tilde{p}_i)^2 \qquad\qquad IV.4$$

where $\tilde{p}_b$ is the beam momentum four-vector, $\tilde{p}_t$ is the neutron or deuteron momentum, and the sum is over all detected final state particle momenta. The unshaded MM^2 entries in Figs. IV.12 and IV.14 are the uncut data, the light-shaded events have survived the topology cut, and the dark-shaded events have survived the
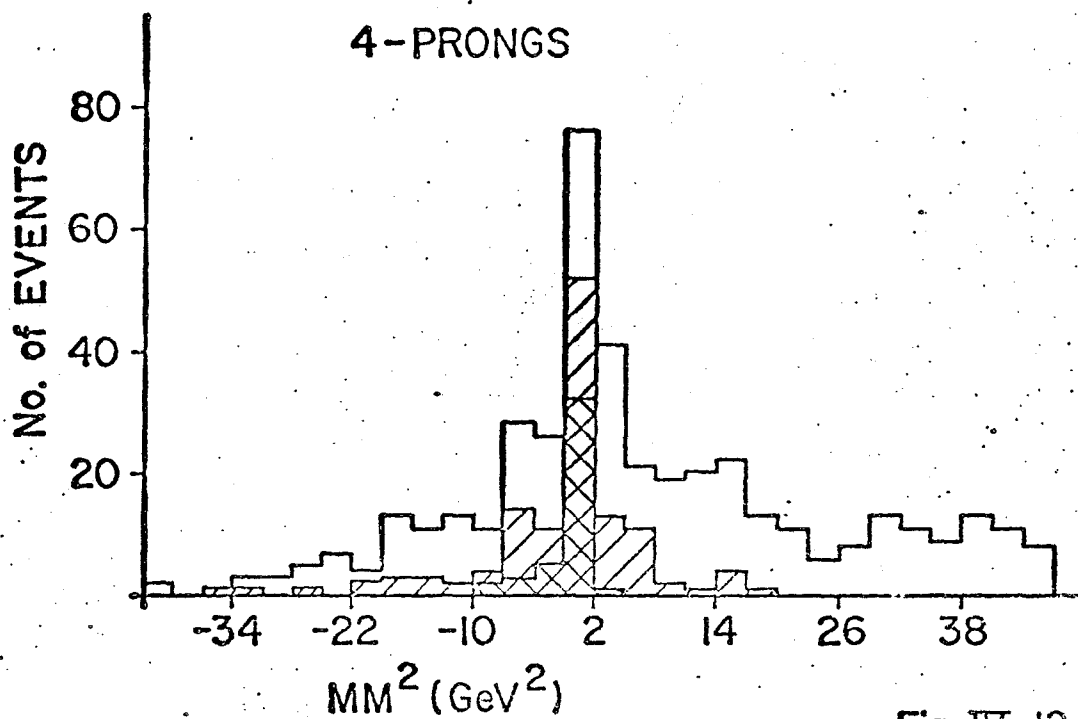
Fig. IV.12
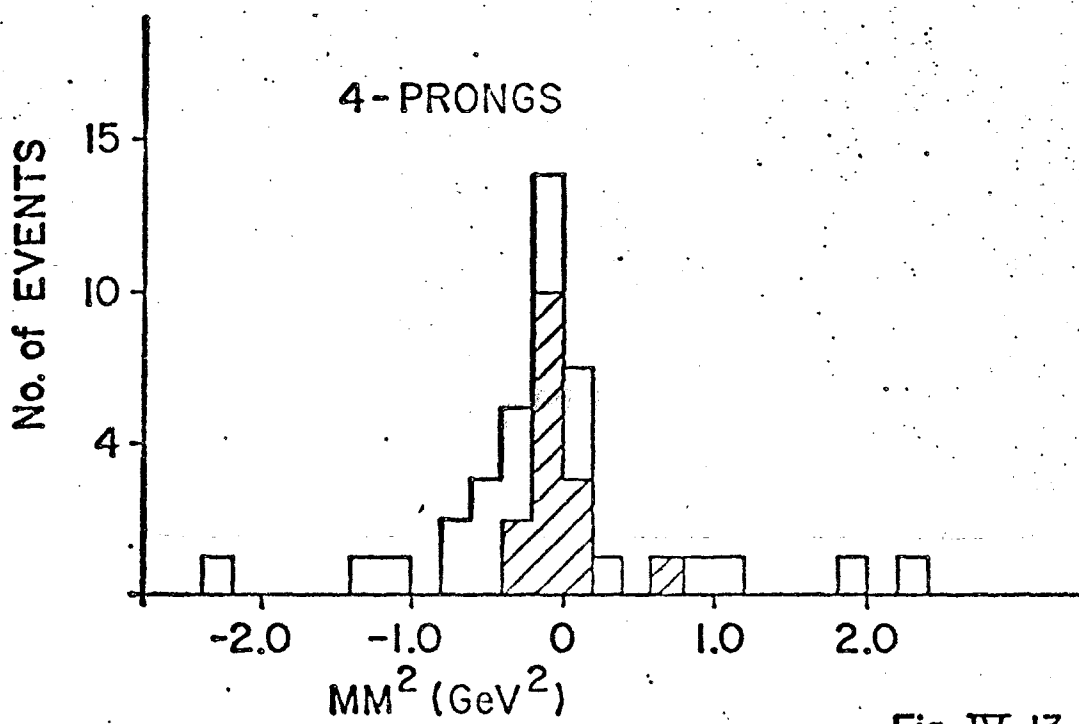
Fig. IV.13

Fig. IV.14

Fig. IV.15
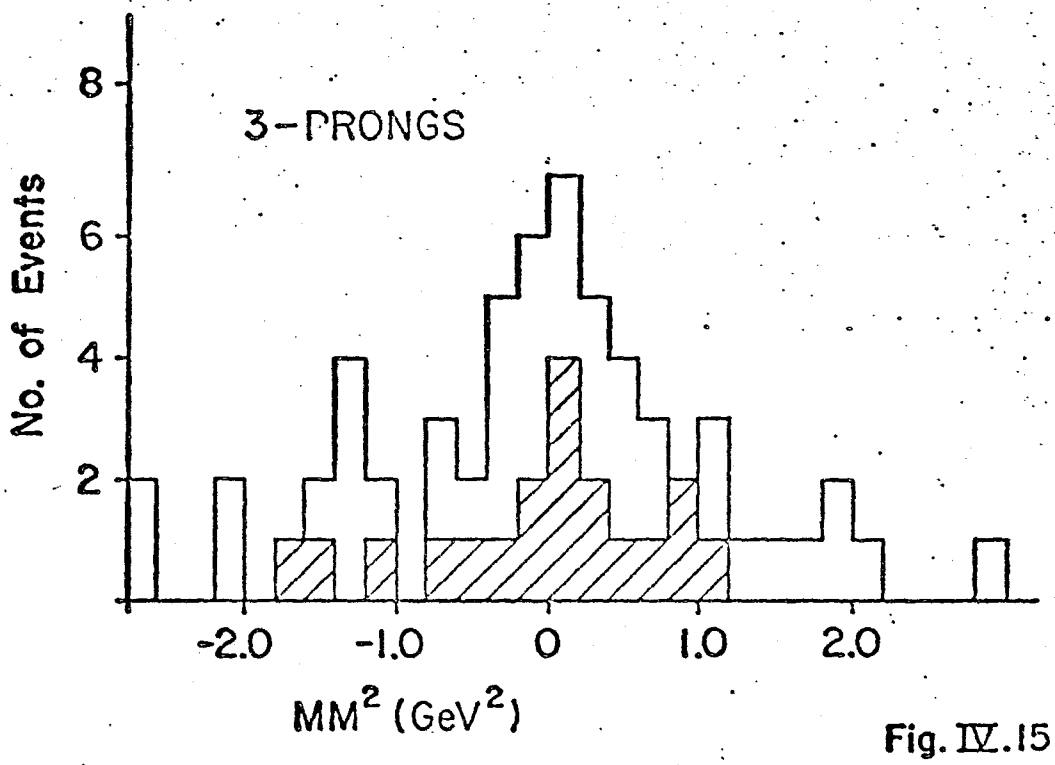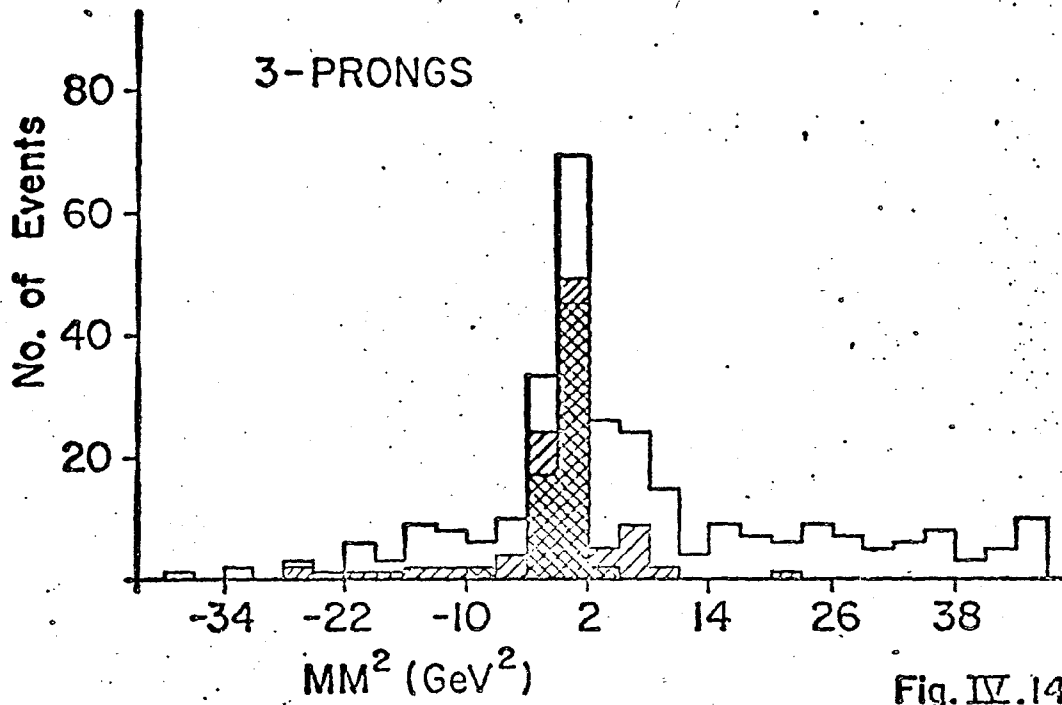
fragmentation cut. Figs. IV.13 and IV.15 show in greater detail the events surviving the fragmentation cut (unshaded) and the final sample (shaded) after the transverse momentum cuts.

Of the 44 events satisfying the ionization mass determinations and the 4C fit criteria of SQUAW, 28 passed the 3 kinematic cuts. The remaining 16 events were lost during the final cut. Note however that we have neglected the strong correlation between longitudinal and transverse momentum. By changing the momentum magnitude of the fast outdoing track within the limits of the longitudinal momentum resolution in Figs. IV.6 and 7 ($\sim$8 GeV), all 16 events survive the transverse momentum cuts.

In addition, the cutting program found only 2 events that did not pass SQUAW. Both were fit by SQUAW as three constraint events, the momentum magnitude of the stopping track in each event being considered a poorly measured quantity. (One was a very short stub with a large length error, the other a very long stopping track that failed the K-Prong curvature test. See Refs. 5 and 6 in Chapter II. These events will be included in the final event sample, bringing the total number of events to 46. A summary of the events is given in Table IV.1. Using our spectator model, $\sim$1/3 of the spectator protons should be visible. The 4-prong to total event ratios of .34$\pm$.09 and .41$\pm$.12 for the proton and pion beam samples are consistent with this figure.

TABLE IV.1

FINAL EVENT SAMPLE FOR REACTION IV.1

BEAM TYPE	PRONG COUNT	NO. of EVENTS
p	3	19
p	4	10
π^+	3	10
π^+	4	7

C. Cross Section Calculations

The calculation of the cross section for Reaction IV.1a is a straight forward procedure. Throughout this analysis, 4-prong events with visible stubs will be considered neutron target events, regardless of the stub length, unlike in Chapter III, where corrections for stub visibility are made. The cross section is given by Eq. IV.5,

$$\sigma(hd \to hpp\pi^-) = n_F \cdot \mu / (\epsilon_B \cdot \epsilon_T) \qquad \text{IV.5}$$

where n_F is the number of fitted events, μ is the microbarn-per-event equivalence for the sample of events containing the n_F fitted events, ϵ_B is the beam tagging efficiency and ϵ_T the track organizing efficiency. The fractional error for σ is given in Eq. IV.6.

$$(\Delta\sigma/\sigma) = \left[(\Delta n_F/n_F)^2 + (\Delta\mu/\mu)^2 + (\Delta\epsilon_B/\epsilon_B)^2 + (\Delta\epsilon_T/\epsilon_T)^2 \right]^{\frac{1}{2}} \qquad \text{IV.6}$$

The fitted event sample is discussed in Sections IV.A and B. We let $\Delta n_F = n_F^{\frac{1}{2}}$. Using $\sigma(hd, N=4)$ values found in Table III.1, n_s, the total number of scanned 3- and 4-prong events from which the measured sample was obtained, and the fractions of proton and pion beam events, f_p and f_π, for the 3- and 4-prong events as tagged by the PWGP program, μ may be written as

$$\mu = \sigma(hd, N=4)/(n_s \cdot f_h) \qquad \text{IV.7}$$

with the fractional error in μ given in Eq. IV.8 .

$$(\Delta\mu/\mu) = \left[(\Delta\sigma(hd, N=4)/\sigma(hd, N=4))^2 + (\Delta n_s/n_s)^2 + (\Delta f_h/f_h)^2 \right]^{\frac{1}{2}}$$

IV.8

The error in n_s is $n_s^{\frac{1}{2}}$. The beam tag efficiency is the ratio of tagged to total events processed by PWGP. We include 5- and 6-prong events in this sample in order to minimize the error in ϵ_B. (Tagging is independent of multiplicity.) The efficiency for track organizing is discussed in Section II.G.

The cross sections for the reaction in Eq. IV.1a are given in Table IV.3, and values of the quantities used in the calculations are summarized in Table IV.2. (An entry in only the pd column implies that the entry is used for both the proton and pion beam calculations.) These cross sections for deuteron break-up with single pion production should be used as a lower limit only. Rescatter events will normally not have a very slow or backwards spectator-like proton. Therefore some of these events were not measured because they did not satisfy the neutron-target criteria discussed in App. G. However, these missed events will not effect the free neutron cross sections calculated in the next section.

D. "Free" Neutron Target and Dissociation Cross Sections

The cross section for an unbound or "free" neutron target, $hn \to hp\pi^-$, may be calculated in two different manners. The first technique (Method 1) uses only the fitted three-prong events which

TABLE IV.2

PARAMETERS USED IN CALCULATING $\sigma(hn \rightarrow hp\pi^-)$

PARAMETERS	pd	π^+d
n_F	29 ± 5.4	17 ± 4.1
$\sigma(hd, N=4)$ mb	12.81 ± 0.58	7.57 ± 0.48
n_s	2769 ± 53	————
f_h	$(1037/1537) = 0.674 \pm 0.012$	$(481/1537) = 0.313 \pm 0.012$
μ $\mu b/ev$	6.86 ± 0.36	8.73 ± 0.67
ϵ_B^*	$(3145/3732) = 0.843 \pm 0.006$	————
ϵ_T	0.798 ± 0.070	————
n_3	19 ± 4.4	10 ± 3.2
$\sigma(hn, N=3)$ mb	6.17 ± 0.37	3.88 ± 0.38
n_{3s}	706 ± 27	————
μ_3 $\mu b/ev$	12.97 ± 0.94	17.56 ± 1.96
n_{nr}	28 ± 5.3	16 ± 4.0
n_{td}	28 ± 5.3	15 ± 3.9
G	0.947 ± 0.006	0.961 ± 0.004
R	0.792 ± 0.019	0.848 ± 0.026

* Corrected for parts of rolls where chambers malfunctioned and events were not included in the sample fed to SQUAW.

have a slow proton and by definition are not coherent events. A microbarn-per-event equivalence, μ_3, is calculated as in Eq.IV.7, but using the free neutron target cross sections for 3-prong events, $\sigma(hn, N=3)$, found in Table III.5. Instead of n_s, we use the total number of scanned three-prong events in our event sample, n_{3s}, corrected for coherent events using Eq. III.5. (The cross sections are converted to numbers of events.) The microbarn-per-event equivalence for free neutron target events is then μ_3 and $n_3 \cdot \mu_3 / (\epsilon_B \cdot \epsilon_T)$ is the free neutron target cross section. The advantage of this method is that we do not have to concern ourselves with rescattering. Our fitted event sample contains no rescatter events because rescatter events will have an even-prong count, and μ_3 is also calculated using just odd-prong events. The major drawback is that we do not use all the fitted data at our disposal by ignoring the 4-prong events.

In order to use the 4-prong events (Method 2), rescatter events in the fitted sample cannot be used, as they are not the result of a single target nucleon interaction. As previously mentioned, rescatter events will not have a readily recognizable spectator proton. In this case, backward spectator events may safely be assumed to not have rescattered. Events where the slowest proton is forward with respect to the beam but has a momentum less than 300 MeV/c will also be considered to not have rescattered. (The 300 MeV/c limit is larger than 98.5% of the spectator momenta according to our Hulthen spectator model of App. G.) Only one

event for each beam type for the fitted events could be considered
to have rescattered, each having a forward "spectator" momentum
greater than 500 MeV/c. This is less than the 20% (14%) of all
$pd(\pi^+d)$ events one expects to have rescattered, but as explained
in the previous section, rescatter events did not satisfy the
measuring rules at some institutions.

The cross section formula for Method 2 is given in Eq. IV.9

$$\sigma(hn \to hp\pi^-) = n_{nr}\mu/\varepsilon_T\varepsilon_B \; GR \qquad\qquad \text{IV.9}$$

G and R are the Glauber screening (see App. G) and rescattering
corrections respectively, and n_{nr} is the number of fitted 3-prong
plus non-rescattering 4-prongs events. The rescattering correction
is taken to be $(1-F_{rs})$, where F_{rs} is the rescattering fraction
defined in App. G. Using this method increases our statistics but
introduces the problem of recognizing a rescatter event and
correcting μ as to represent the proton + neutron target cross
section.

In Table IV.3, the cross sections for $hn \to hp\pi^-$ are
presented, M1 and M2 denoting which method was employed. The
results of the two methods are equal and we therefore claim we
know how to correct for the rescattering contribution, in order to
derive the free neutron target cross sections. In subsequent
analyses, we will use the results of Method 2, which yields smaller
overall errors.

The cross section for neutron target dissociation can be

TABLE IV.3

CALCULATED CROSS SECTIONS

REACTION	CROSS SECTION μb
$p + d \rightarrow p + p + p + \pi^-$	$> 296 \pm 63$
$\pi^+ + d \rightarrow \pi^+ + p + p + \pi^-$	$> 221 \pm 59$
$p + n \rightarrow p + p + \pi^-$ (M1)	366 ± 94
$p + n \rightarrow p + p + \pi^-$ (M2)	381 ± 82
$\pi^+ + n \rightarrow \pi^+ + p + \pi^-$ (M1)	261 ± 90
$\pi^+ + n \rightarrow \pi^+ + p + \pi^-$ (M2)	255 ± 71
$p + n \rightarrow p + (p\pi^-)$	381 ± 82
$\pi^+ + n \rightarrow \pi^+ + (p\pi^-)$	239 ± 68

TABLE IV.4

NON-CHARGE EXCHANGE FRACTION FOR $\sigma(pn \to pp\pi^-)$

REF.	P_{LAB} GeV/c	$f(Q=0)$
7	7.0	0.702 ± 0.012
8	11.0	0.744 ± 0.014
9	12.5	0.784 ± 0.008
10	19.0	0.819 ± 0.015
6	28.0	0.880 ± 0.040
THIS EXP.	97.7	> 0.917

calculated using Eq. IV.9, if one uses only the target dissociation events n_{td} contained in n_{nr}. At lower energies, target dissociation (non-charge exchange) events are selected using the minimum invariant mass (MIM)[5] method or the minimum rapidity difference (MRD)[6] method. The charge and non-charge exchange reactions are illustrated in Figs. I.2a and 2b.

The MIM method associates the produced π^- with either the fast hadron or the slow proton, whichever yields the smallest invariant mass for the system. See Eqs. IV.10a and 10b.

$$h + n \to h + (p \pi^-) \quad \text{if } M(p\pi^-) < M(h\pi^-) \qquad \text{IV.10a}$$

$$h + n \to (h\pi^-) + p \quad \text{if } M(p\pi^-) > M(h\pi^-) \qquad \text{IV.10b}$$

This criterion may not be valid in the pion beam sample as the mass of the pion beam is much smaller than the mass of the slow proton, but the large separation of the target and beam fragmentation regions at our energy, makes the mass difference unimportant.

The rapidity of a particle is given by Eq. IV.11.

$$y \equiv 1/2 \ln (E+p_{//})/(E-p_{//}) \qquad \text{IV.11}$$

Though not a Lorentz invariant quantity, the difference of rapidities between two particles is invariant along the direction of the transformation. Instead of using the invariant mass, we use the

rapidity differences to define the $h\pi^-$ and $p\pi^-$ systems in
Eqs. IV.10a and 10b.

From the entire fitted event sample, only one pion beam
event is found satisfying the charge exchange requirement of
Eq. IV.10b, using either the MIM or MRD method. The non-charge
exchange fraction for the pion beam cross-section is $(.938\pm.061)$ and
a lower limit of .917 (90% confidence level) is given for the
proton beam cross section. In Table IV.4 we list the non-charge
exchange fractions for the reaction $pn \rightarrow pp\pi^-$ measured in this
experiment and in experiments at lower energies. Our value is consistent
with the increase of the fraction with energy as seen in the
results of the other experiments.

For the proton beam events $n_{td} = n_{nr}$ as no charge exchange
events were found, and $n_{td} = 15$ was used for the pion beam sample.
The neutron dissociation cross sections (Reaction IV.1b) are given
in Table IV.3. It is interesting to note that the ratio r

$$r \equiv \sigma(\pi^+ n \rightarrow \pi^+(p\pi^-))/\sigma(pn \rightarrow p(p\pi^-)) = .627\pm.140 \qquad \text{IV.12}$$

is very close to the ratio of total $\pi^+ n$ and pn cross sections,
$\sigma_T(\pi^+ n)/\sigma_T(pn) = .616\pm.002$, calculated from the total cross sections
given in Ref. 4. In analogy to the similar scaling of inclusive
cross-sections as discussed in Section I.C, the scaling of the above
exclusive cross sections indicates that any model used to describe
neutron dissociation should be factorizeable. Finally, our value
for the cross section is higher than but not inconsistent with

values between 260 and 280 μb measured by Biel[17] in the same energy region.

E. **The Energy Dependence of $pn \to p(p\pi^-)$**

The cross sections for the neutron dissociation in Reaction IV.10a and the charge symmetric nucleon dissociation

$$p + p \to p + (n\pi^+) \qquad \text{IV.13}$$

have been measured over a large range of incident beam momenta. For direct comparison, the cross section for the charge symmetric dissociation should be divided by 2 as either proton could dissociate. Figs. IV.16a through 16c give a convenient representation of the amplitudes that are responsible for the above reactions and single pion production in any nucleon-nucleon collision. The symbol $M_I^{I_x}$ will be used to represent the amplitude where I_x is the isospin exchanged and I is the isospin of the produced $N'\pi$ system. For example, diffractive processes would be contained in the $M_{1/2}^0$ amplitude, whereas Δ (isospin 3/2) production would be contained exclusively in the $M_{3/2}^1$ amplitude.

It was shown by Koba, Møllerund and Veje[20] that the three isospin amplitudes squared and the three interference terms, integrated over the available phase space and summed over helicities, are uniquely defined by the seven independent nucleon-nucleon reactions for single pion production. See Eqs. IV.14a through 14g. (The helicity summation and phase space integrations are implicit.)

$$M^O_{1/2} = $$

$I_x = 0$

$I = 1/2$

Fig. IV.16a

$$M^1_{1/2} = $$

$I_x = 1$

$I = 1/2$

Fig. IV.16b

$$M^1_{3/2} = $$

$I_x = 1$

$I = 3/2$

Fig. IV.16c

$$\sigma_1 = \sigma(pp \to n(p\pi^+)) = \frac{2}{3} |M^1_{3/2}|$$

<div align="right">IV.14a</div>

$$\sigma_2 = \sigma(pp \to p(n\pi^+)) = \frac{2}{3} \left| M^0_{1/2} - \frac{1}{3} M^1_{1/2} + \frac{1}{3} M^1_{3/2} \right|^2$$

<div align="right">IV.14b</div>

$$\sigma_3 = \sigma(pp \to p(p\pi^0)) = \frac{1}{3} \left| M^0_{1/2} - \frac{1}{3} M^1_{1/2} + \frac{2}{3} M^1_{3/2} \right|^2$$

<div align="right">IV.14c</div>

$$\sigma_4 = \sigma(pn \to p(p\pi^-)) = \frac{2}{3} \left| M^0_{1/2} + \frac{1}{3} M^1_{1/2} - \frac{1}{3} M^1_{3/2} \right|^2$$

<div align="right">IV.14d</div>

$$\sigma_5 = \sigma(pn \to (p\pi^-)p) = \frac{2}{27} \left| 2M^1_{1/2} + M^1_{3/2} \right|^2$$

<div align="right">IV.14e</div>

$$\sigma_6 = \sigma(pn \to p(n\pi^0)) = \frac{1}{3} \left| M^0_{1/2} + \frac{1}{3} M^1_{1/2} + \frac{2}{3} M^1_{3/2} \right|^2$$

<div align="right">IV.14f</div>

$$\sigma_7 = \sigma(pn \to (n\pi^0)p) = \frac{4}{27} \left| M^1_{1/2} - M^1_{3/2} \right|^2$$

<div align="right">IV.14g</div>

The notation $N_1 N_2 \to N_3(N_4 \pi)$ associates the produced pion with nucleon N_4. Unfortunately, only σ_1 through σ_5 were measurable by bubble chamber techniques at lower energies, as σ_6 and σ_7 have too many undetectable neutral particles in the final state. Five of the amplitude terms can be empirically measured as a function of the remaining term. Refs. 7 and 10 studied the energy dependence of the amplitudes and interference terms as a function of $m_{13} \equiv \text{Re}\langle M^1_{1/2} M^1_{3/2}\rangle$. It was argued that m_{13} should be approximately 0.0 because of the very different mass distributions of the isospin 1/2 and 3/2 states, and as a result, empirically found that

$$m_3 \equiv |M^1_{3/2}|^2 \sim p^{-1.87}_{LAB} \qquad \text{IV.15a}$$

$$m_1 \equiv |M^1_{1/2}|^2 \sim p^{-1.37}_{LAB} \qquad \text{IV.15b}$$

$$m_0 \equiv |M^0_{1/2}|^2 \sim p^{-0.33}_{LAB} \qquad \text{IV.15c}$$

$$m_{01} \equiv Re\langle M^0_{1/2} M^1_{3/2}\rangle \sim 0.0 \qquad \text{IV.15d}$$

$$m_{03} \equiv RE\langle M^0_{1/2} M^1_{1/2}\rangle < 0.0 \qquad \text{IV.15e}$$

Here p_{LAB} is the effective beam momentum in the LAB. As a function of energy, M_{03} approached 0.0 with an increase in energy and at 28 GeV/c was down to only 10% the size of m_0. We note the charge exchange amplitudes m_1 and m_3 fall rapidly with energy but that m_0 amplitude, containing diffractive processes, has a much slower energy dependence. The data used in obtaining Eqs. IV.15a through 15e were all at a p_{LAB} less than 30 GeV/c, except for one point in the ISR region[19] used by Ref. 10 in their analysis.

In our energy region, we expect σ_2 and σ_4 to be dominated by m_0. The energy dependence of the remaining terms will make them negligible. Indeed, if we look at the $(p\pi^-)$ mass distribution in Fig. IV.17, we see events clustered between 1.35 and 1.50 GeV/c, well above the $\Delta(1236)$ isospin $-\frac{3}{2}$ region, and near the $N^*(1470)$ isospin $-\frac{1}{2}$ resonance.

We plot the cross sections for σ_2 and σ_4 as a function of
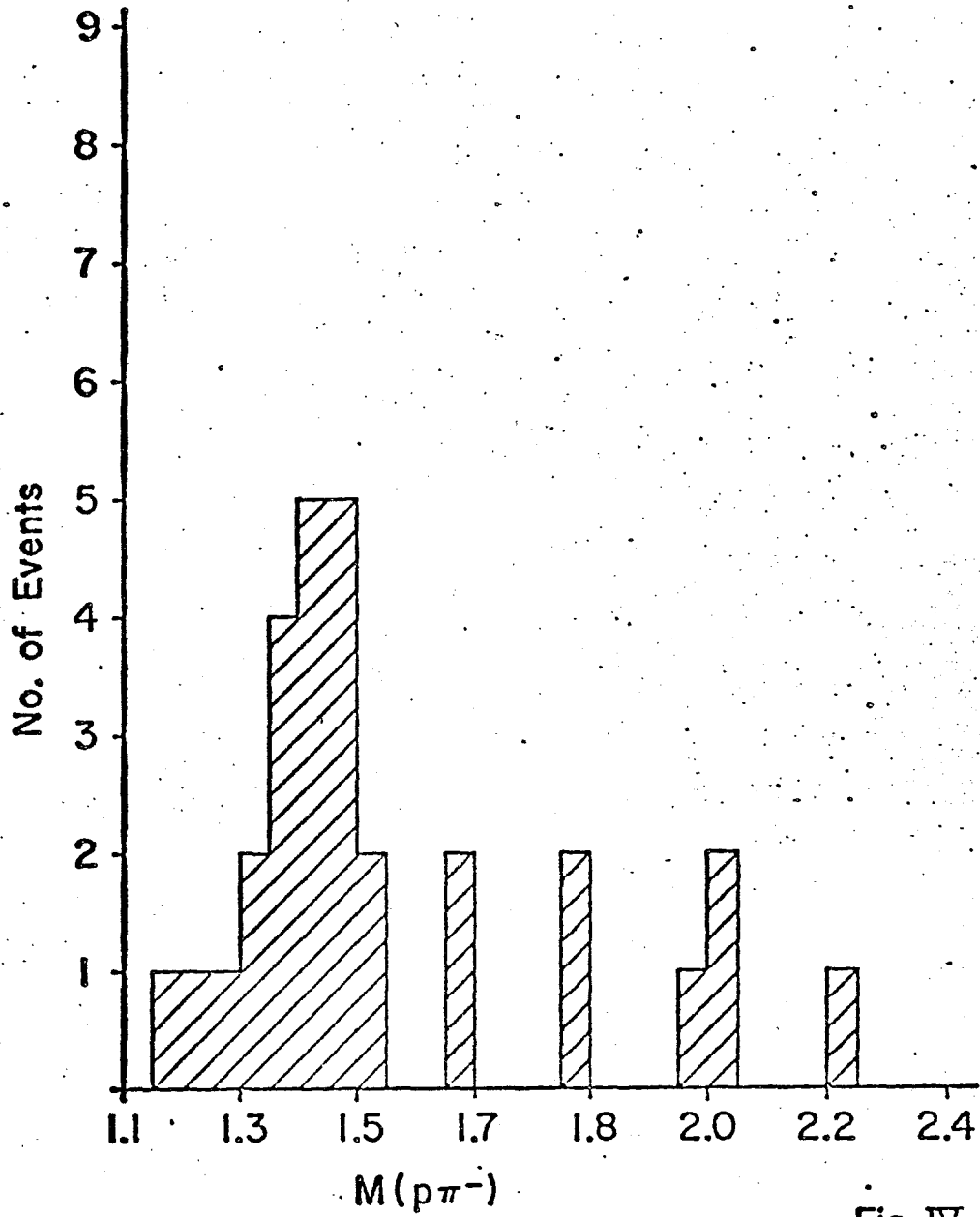
Fig. IV.17

P_{LAB} in Fig. IV.18 for all data now available. Cross sections measured with deuterium beams or targets have been corrected for Glauber screening (if not already done so) and rescattering to obtain a free neutron cross section. We use a value of G equal to .95 as G has been found to be constant down to an incident momentum of 7 GeV/c.[4,7,10] The rescattering fraction for pd events, F_{rs} =.2, is constant above 28 GeV/c[11]. We then naively correct all deuterium data using R = 1-F_{rs} ≃ .8. The summary of the values plotted and their references are given in Table IV.5.

The energy dependence of the cross section was fit to the functional form $\sigma = Ap^{-n}$. The best fit yields n = 0.41±0.04 with a χ^2 of 74.1 for 21 degrees of freedom. Our value of n is larger than, but consistent with, values of (0.36±0.05) and (.30±0.07) for the exponent of the m_0 term from Refs. 10 and 19 respectively. In order to study the sensitivity of the slope n to our rescattering corrections, we have done the same fit, but using uncorrected deuterium data. We obtain n = (.33±.04) for a χ^2 of 97.6, close to previously quoted values yet still consistent with our overall result.

One might argue that we should restrict our fit to higher energy data where the m_0 term will surely dominate. Fits using data taken at 19 GeV/c or 28 GeV/c and greater yield, the same value of n. However, the energy dependence of the cross section above P_{LAB} = 40 GeV/c may flatten out. In particular, if one uses only data above 28 GeV/c, one obtains a much smaller value for n,
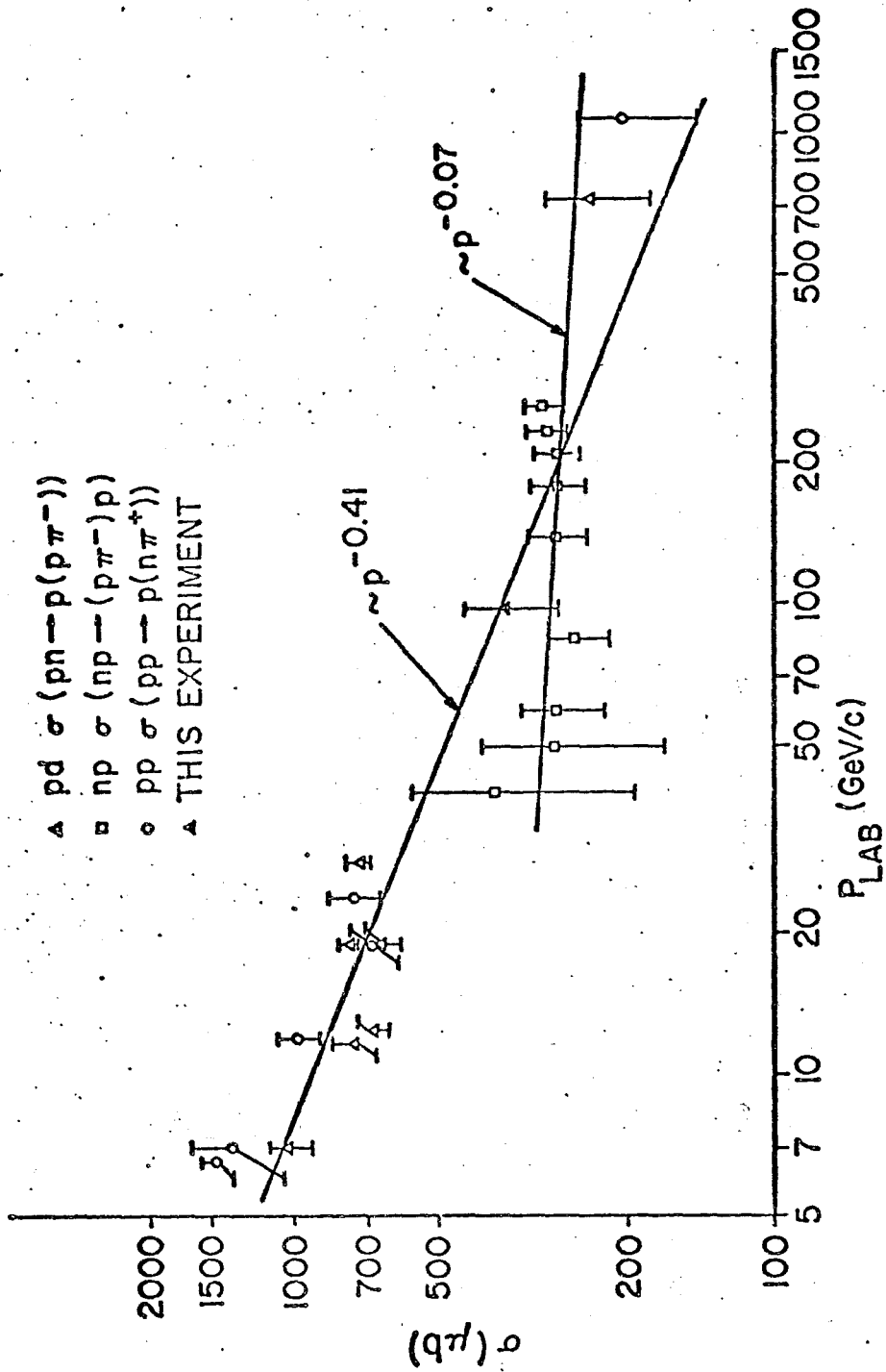
Fig. IV.18

TABLE IV.5

CROSS SECTIONS PLOTTED IN FIG. IV.18

REF.	P_{LAB} GeV/c	σ µb
12 (pp)	6.6	1470±95
7 (pn)	7.0	1026±105
7 (pp)	7.0	1350±300
8 (pn)	11.6	763±75
13 (pp)	12.0	985±100
9 (pn)	12.5	688±62
14 (pp)	19.0	685±75
10 (pn)	19.0	655±39
6,15 (pn)	19.0	765±21
13 (pp)	24.0	755±90
6,15 (pn)	28.0	729±41
16 (pn)	<40.0>	385±190
16 (pn)	<50.0>	290±120
16 (pn)	<60.0>	285±60
17 (pn)	<85.0>	260±39
THIS EXP.	97.7	381±82
17 (pn)	<140.0>	282±38
17 (pn)	<180.0>	289±35
17 (pn)	<208.0>	285±32
17 (pn)	<235.0>	299±31
17 (pn)	<265.0>	304±29
18 (pn)	729.0	239±59
19 (pp)	1079.4	200±55

The (pp) cross sections used here are ½ the total cross section values.

n = .07. This might suggest that in this energy range the cross section is almost entirely diffractive, i.e. it shows little dependence on energy. We note that for $p_{LAB} > 40$ GeV/c, the data are dominated by np experiments.

F. Conclusions

Using bubble chamber techniques and a deuterium target, we have successfully extracted a free neutron cross section for the reactions $pn \to pp\pi^-$ and $\pi^+ n \to \pi^+ p\pi^-$. The cross section for the proton beam reaction is seen to have a fractional contribution from non-charge exchange processes consistent with the rise of this contribution at lower energies. In addition, the absolute value of the cross section for neutron dissociation is consistent with cross sections measured in the same energy range using neutron beam techniques. If the energy dependence for this cross section is parametrized at Ap^{-n}, we obtain an n equal to .41, but the fit is poor.

The fitted value includes new data at Fermilab[17] and ISR[18] energies and significant corrections to the deuterium data to account for rescattering. The poor fit for n is caused by a possible change in energy dependence above 40 GeV/c. Data in this region suggest a more constant cross section, and more accurate measurements, particularly in the region from 30 to 70 GeV/c, would help clarify the exact nature of the energy dependence at this cross section.

REFERENCES

1) D.G.Fong et al., Experimental Results Presented at the
International High Energy Physics Conference, Tbilisi, 1976;
P.Lucas et al., Bull. Am. Phys. Soc. 21, 545 (1976).

2) D.G.Fong et al., Nuovo Cimenta 34A, 659 (1976).

3) N.G.Birger and Yu.A. Smorodin, JETP 9, 823 (1959);
N.G.Birger and Yu.A.Smorodin, JETP 10, 964 (1960).

4) A.S. Carrol et al., Phys. Lett. 61B, 307 (1976).

5) G.Alexander et al., Phys. Rev. 173, 1322 (1968).

6) W.Burdett et al., Nucl. Phys. B48, 13 (1972).

7) G.Yekutieli et al., Nucl. Phys. B38, 605 (1972);
G.Yekutieli et al., Nucl. Phys. B40, 77 (1972).

8) D. Hochman et al., Nucl. Phys. B80, 45 (1974).

9) J.W.Cooper et al., Nucl. Phys. B79, 259 (1974);
J.W.Cooper, Thesis - "Diffraction Dissociation of Nucleons
in dp Interactions at 25 GeV/c", UMBC 75-2 (University of
Michigan, 1975).

10) E.Dahl-Jensen et al., Nucl. Phys. B87, 426 (1975).

11) J.Hanlon et al., SUSB-BCG-78-07 (State University of New
York at Stony Brook, 1978) and to be published.

12) N.C.Colton et al., Nuovo Cimento 11A, 590 (1972).

13) K.Bockmann et al., Nucl. Phys. B81, 45 (1974).

14) H.Böggild et al., Phys. Lett. 30B, 369 (1969);
H.Böggild et al., Nucl. Phys. B32, 119 (1971).

15) J.Hanlon et al., Phys. Rev. D12, 673 (1975).

16) A.Babaev et al., Nucl. Phys. B116, 28 (1976).

17) J.Biel, Thesis — "A Study of the Dissociation Reaction $n + p \rightarrow p\pi^- + p$ For Neutron Momenta Between 50 and 300 GeV/c", UR-614 (Univ. of Rochester, 1977).

18) G.C.Mantovani et al., Phys. Lett. 64B, 471 (1976).

19) W.DeKerret et al., Phys. Lett. 63B, 477 (1976).

20) Z.Koba, R.Møllerund and L.Veje, Nucl. Phys. B26, 134 (1971).

V. SLOW PROTON PRODUCTION

The production of protons slow in the LAB will be studied
in this chapter. Absolute cross sections for the reaction

$$h + n \to p_{s1.} + X \qquad\qquad V.1$$

are measured using new 100 GeV/c data from RUN 3 and 400 GeV/c data
from RUN 2. The differential cross sections are presented and
discussed in terms of a Mueller-Regge formalism with explicit
isospin exchange. Protons produced from neutron dissociation in
a $(p\pi^-)$ system should not be included in the Mueller-Regge analysis.
We therefore study such contamination. A specific model, a
Reggeized-One-Pion-Exchange (ROPE), is shown to be a poor
approximation of the slow proton data if one assumes the off mass-
shell correction parameter to be 0.0. If the parameter is not zero,
as suggested by Bishari,[1] the ROPE model will not describe the data
at all.

A. Absolute Cross Sections

The absolute cross sections for Reaction V.1 were
calculated using the Stony Brook and Fermilab data samples from
RUN 2 and RUN 3. The formula for calculating the cross section
is written as

$$\sigma(hn \to pX) = \sigma(hn, N\geq3) \cdot f \qquad\qquad V.2a$$

$$\Delta\sigma(hn \rightarrow pX)/\ \sigma(hn \rightarrow pX) = \left[\ (\Delta\sigma(hn,N\geq 3)/\ \sigma(hn,N\geq 3))^2 \right.$$
$$\left. +\ (\Delta f/f)^2 \right]^{1/2} \qquad\qquad \text{V.2b}$$

where $\sigma(hn,N\geq 3)$ is the inelastic hn cross section for events with

3 or more prongs and f is the fraction of the neutron target event

sample with a slow proton ($p\leq 1.4$ GeV/c), excluding the spectator

proton. The cross section for slow protons produced from 1-prong

neutron target events has been neglected in our experiment but

will be shown to be small at Fermilab energies. We require that

$|t|$, the absolute value of the square of the four-momentum trans-

ferred between the target and slow proton, be less than 1 GeV.^{2}

(The target momenta are defined using the impulse spectator model of

App.G). This value of $|t|$ is less than the maximum values of

1.2 GeV^2 for a 1.4 GeV/c proton with a neutron target at rest, and

1.1 GeV^2 for the same proton with the neutron target having a

momentum of 120 MeV/c in the beam direction. The Fermi-smearing

of t will therefore not affect the absolute cross sections

measured.

The total hn inelastic cross sections may be obtained from

Table III.5. The 1-prong estimates may be subtracted to obtain

$\sigma(hn,N\geq 3)$ and the error on the total inelastic cross section is

used for $\Delta\sigma(hn,N\geq 3)$. To determine f, we define n_A, the absolute

cross section sample, as all odd-prong events plus even-prong

events with spectator protons tracks less than 5mm in length. The

most "backwards" proton, as described in Section IV.B, is
considered the spectator in even-prong events. This sample
contains only non-rescattering neutron target events and it is
then appropriate to use the free neutron cross sections,
$\sigma(hn, N \geq 3)$, in the cross section calculations. However, there is
some coherent event contamination to this sample, i.e. $hd \to dX$
from 3- through 6-prong events. This is a result of the measure-
ment of all neutron target type events with these multiplicities,
regardless of whether there was a slow ($p < 1.4$ GeV/c) non-spectator
track. Using the coherent cross section estimates in Ref. 2, we
find that less than 3% of either the pn or $\pi^+ n$ total sample is
coherent and this contamination will be neglected.

All events in n_A with a slow non-spectator proton such that
$|t|$ is less than 1.0 GeV^2, will be included in n_p, the number of
slow proton events. Hence, $f = n_p/n_A$. There is no coherent
contamination to n_p, as there is an identifiable proton in the
event besides the (invisible) spectator proton. Odd-prong
coherent events won't have a slow proton and even-prong coherent
events won't have 2 identifiable protons.

Both n_A and n_p are weighted numbers of events, reflecting
the processing efficiencies for measuring neutron target type events.
Table V.1 contains these processing weights and shows that these
weights are close to unity. In Table V.2, we give the values of
$\sigma(hn, N \geq 3)$, n_A and n_p used to calculate the inclusive cross sections
for Reaction V.1, also given in the table. From Ref. 3, we obtain

TABLE V.1

ABSOLUTE CROSS SECTION PROCESSING WEIGHTS

	RUN2 (400 GeV/c)		RUN3 (100 GeV/c)	
N	SUNY	FNAL	SUNY	FNAL
3	1.016	1.000	1.064	1.000
4	1.021	1.000	1.056	1.025
5	1.005	1.005	1.114	1.011
6	1.014	1.003	1.072	1.010
7	1.000	1.008	1.027	1.020
8	1.000	1.003	1.048	1.020
9	1.000	1.003	1.026	1.000
10	1.012	1.000	1.050	1.000
11	1.000	1.007	1.076	1.000
12	1.011	1.000	1.136	1.000
13	1.029	1.014	1.097	1.000
14	1.024	1.000	1.085	1.000
15	1.014	1.029	1.052	1.000
16	1.048	1.000	1.227	1.000
17	1.053	1.000		
18	1.094	1.000		
19	1.000	1.024		
20	1.142	1.000		
21	1.000	1.000		
22	1.000	1.000		
23	1.111	1.167		
24	1.000	1.000		
25	1.000	1.200		

TABLE V.2

PARAMETERS FOR CALCULATING $\sigma(hn \rightarrow p X)$

PARAMETER	100 GeV/c		400 GeV/c
	$\pi^+ n$	pn	pn
$\sigma(hn, N \geq 3)$ (mb)	19.55 ± 0.15	29.07 ± 0.44	31.2 ± 1.2
n_A	1130.04	674.40	5896.84
n_p	199.98	132.06	1044.44
f	0.177 ± 0.11	0.196 ± 0.015	0.177 ± 0.005
$\sigma(hn \rightarrow p X)$ (mb)	3.46 ± 0.22	5.69 ± 0.44	5.52 ± 0.26
$\sigma(hn \rightarrow p X)$ (mb) RUN 1	3.9 ± 0.3	5.7 ± 0.3	————
$<\sigma(hn \rightarrow p X)>$ (mb)	3.61 ± 0.18	5.70 ± 0.30	5.52 ± 0.26
n_p^v	673 ± 26	875 ± 30	1592 ± 40
μ (μb/ev)	5.48 ± 0.36	6.51 ± 0.36	3.47 ± 0.18

the slow proton cross sections previously obtained from the data
of RUN 1. The weighted averages of the 100 GeV/c cross sections
will be used in the subsequent analyses of the 100 GeV/c data.

The inclusive cross sections for proton production from a
neutron target, have also been measured for protons and pions incident
at 195 GeV/c.[8] Values of (5.15±0.25) mb and (3.4±0.3) mb are
quoted ($|t|<1.0$ GeV^2) for the proton and pion beam samples
respectively, which are slightly lower than our cross sections at
both 100 and 400 GeV/c. The value for the slow proton cross
section from 1-prong proton beam events is (0.02±0.014) mb,
showing this contribution to the total inclusive cross section to
be negligible at Fermilab energies. (Ref. 8)

At a beam momentum of 11.6 GeV/c,[9] the pn $\rightarrow$ pX cross section
was found to be ($5.1^{+0.4}_{-0.1}$) mb, for $|t|<.82$ GeV^2. If we make the
same t-cut, our cross-sections are (5.34±0.23) mb and (5.15±0.23) mb
at 100 and 400 GeV/c, equal to the cross section at the much lower
energy. The inclusive cross sections exhibit very little energy
dependence. This will be discussed further in Section V.C.

B. The Total Event Sample and Differential Cross Sections

To study the kinematic distribution of events, we will use
a larger slow proton event sample, n_p'. Included in n_p' are events
from all collaborating institutions for all RUNS, that are either
odd-prong events with a slow proton or even-prong visible
spectator events with a slow proton. The visible spectator may be
either forward or backwards with respect to the beam direction,

but must have a momentum less than 300 MeV/c. The number of events (n_p) and μ, the microbarn-per-event equivalence, are given in Table V.2 for the 100 GeV/c pn and π^+n and the 400 GeV/c pn total samples.

Figures V.1 through .4 display the slow proton cross section as a function of t and t', where $t' = t - t_{min}$. The minimum allowed value of t, discussed in App. A, is calculated using Eq. V.3.

$$t_{min} = -2 \cdot (E_t^* \cdot E_p^* - p_t^* \cdot p_p^*) + m_t^2 + m_p^2 \qquad V.3$$

The t and p subscripts indicate target and proton variables respectively. In Fig. V.1, we present dσ/dt as a function of t. The similarity in shape of the hn cross sections implies that the t-dependence is independent of beam energy and type. Also shown is the t-dependence of the cross section for slow proton production from pp collisions at 400 GeV/c from Ref. 3. At small values of t, dσ/dt falls off faster for the pp data, indicative of the diffractive nature of the pp processes in this region of phase space. At large t, there is still a difference in absolute values between the pp and pn cross sections. This perhaps indicates differences in the proton production process outside the pp $\rightarrow$ pX diffractive region at phase space.

The uncertainty in t for any t-bin is dominated by Fermi-smearing (App. G) and not our measurement errors, which are small for particles slow in the LAB. See App. E. Using a Fermi-
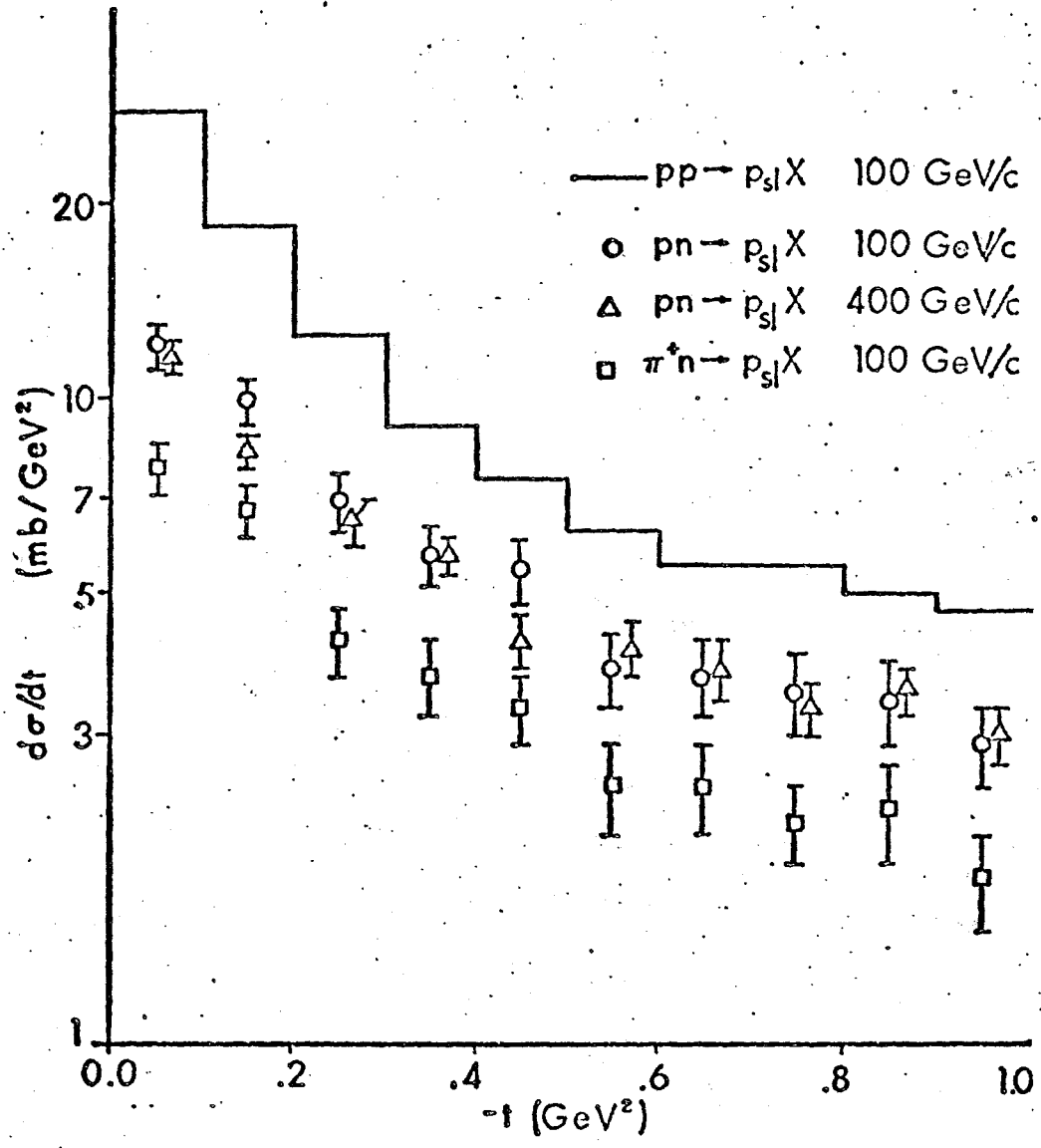
Fig. V.1

smeared ROPE model as an approximation of the data, discussed in Section V.D and App. F, we calculate our resolution Δt to be between .016 GeV^2 and .057 GeV^2. These numbers correspond to the error in the lowest and highest $|t|$ regions. The resolution is better than the bin width of the smallest (.1 GeV^2) t-bins used in our analysis.

Restricting our attention to the region $M^2/s < .2$, we may directly compare our results with those of the deuterium gas jet experiment of Ref. 4. Fig. V.2 shows $d\sigma/dt$ for our data in this region. The straight lines have an exponential slope of 10 and are normalized to the areas under the pn and π^+n data points. The fitted slopes for the 100 GeV/c π^+n and pn data were (9.55±1.07) and (9.12±0.85) GeV^{-2} with a χ^2 per degree of freedom of 0.65 and 0.33 respectively. The slope for the 400 GeV/c data was found to be (10.57±0.68) GeV^{-2} with a $\chi^2/d.o.f. = 0.25$. Within errors, the cross sections have the same t-dependence in this M^2/s region. A slope of 8 is roughly estimated in Ref. 4. Both this slope and ours are markedly steeper than the e^{6t} dependence for pp → pX reactions[5,6] for incident momenta from 50 to 400 GeV/c. (A cut is made at very small M^2/s in the pp data to eliminate events in the diffractive pp peak.)

The t' plots are presented in Figures V.3 and V.4. The use of t' eliminates the effects of the t_{min} boundary at large M^2/s. Compare these figures with Fig. V.1. The hn → pX cross section may be fit to the form $e^{bt'}$ over the entire t' range; the
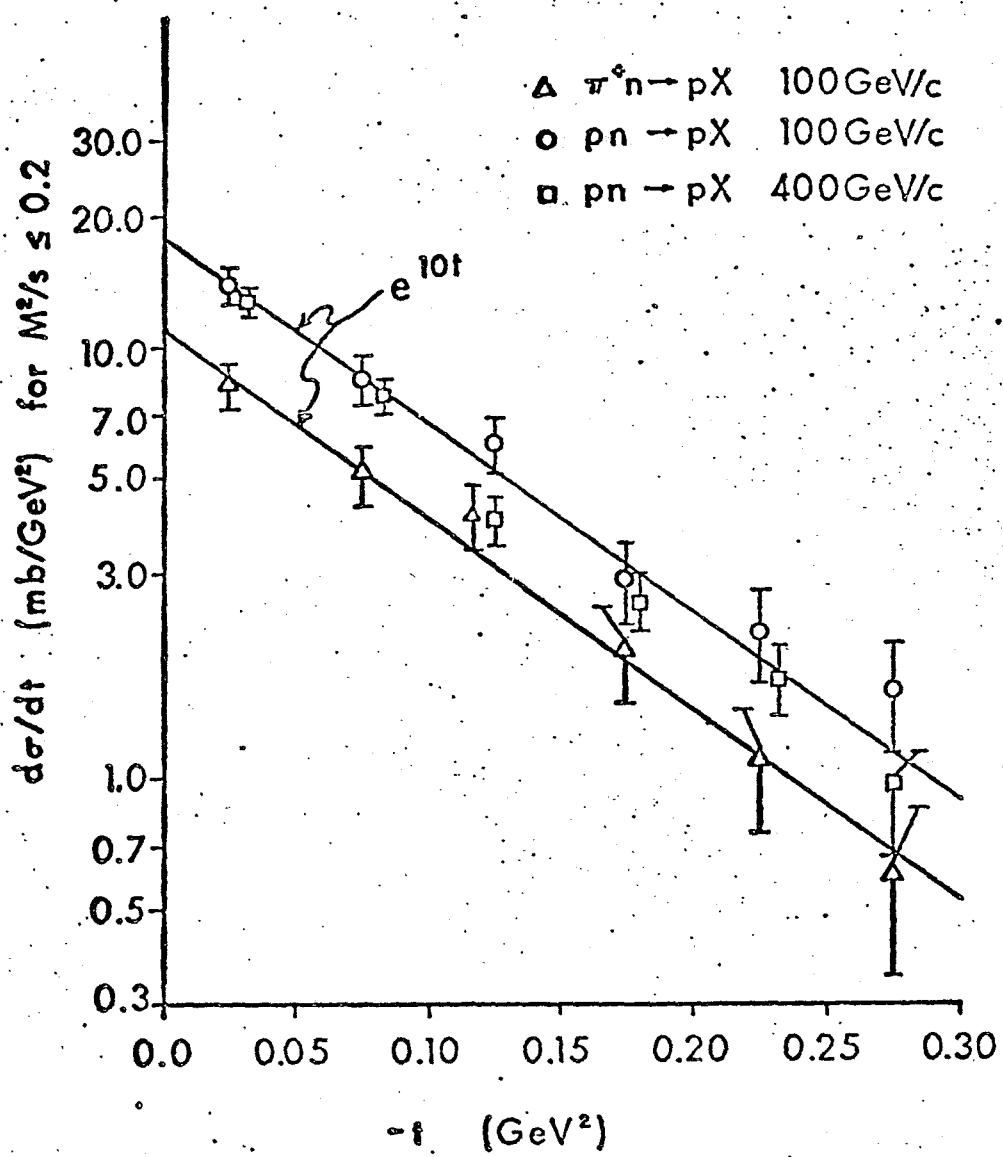
Fig. Ⅴ. 2
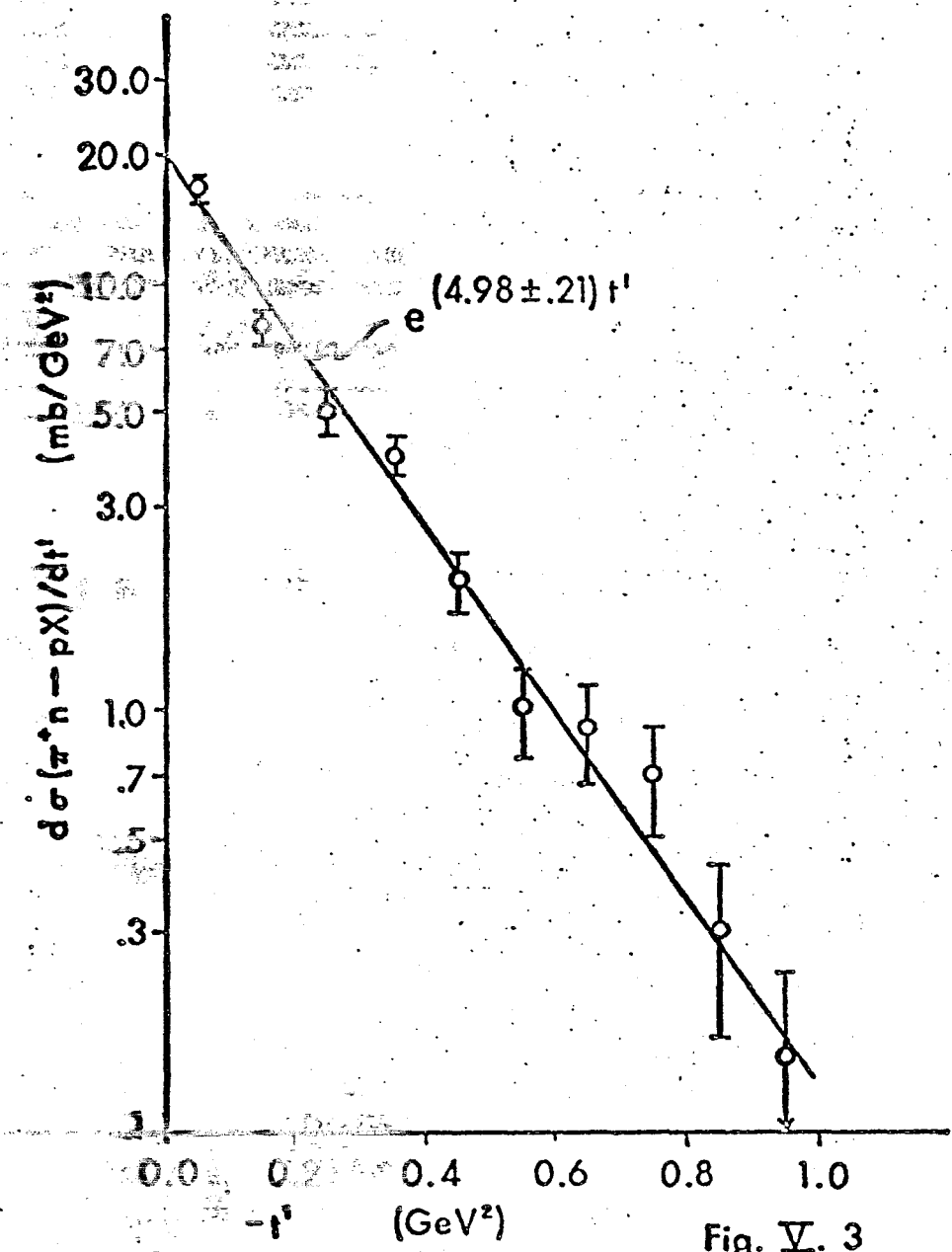
Fig. V. 3
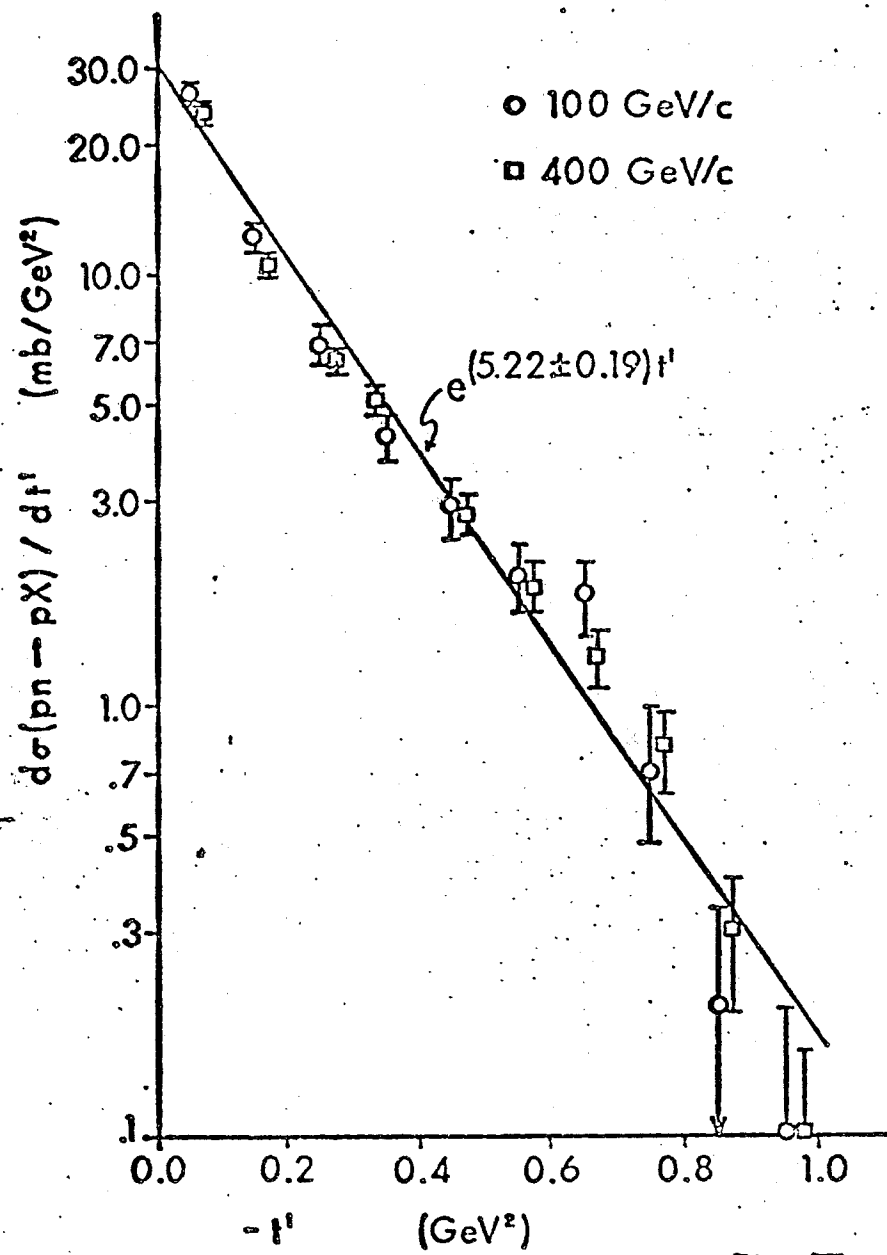
Fig. $\overline{\mathbb{V}}$. 4

best fits to the 100 GeV/c data are given on each graph. The
best fit for the 400 GeV/c data yields $b = (5.07\pm0.14)$ GeV^{-2}. All
values of b are equal within errors.

The M^2/s dependences of the cross sections for Reaction V.1
are displayed in Figures V.5 through .7. (The 100 GeV/c pn
cross section has been calculated in M^2/s bins off-set by 1/2 the
bin width for display purposes.) Again using the Fermi-smeared
ROPE model, we may estimate our M^2/s resolution. It is found to be
a function of t. The biggest uncertainty is $\Delta(M^2/s) = 0.025$ in the
lowest $|t|$ bin. This is 1/2 of our plotted bin width. Our
calculated resolution is actually a lower limit. Firstly, we
have neglected measurement errors which significantly contribute
to $\Delta(M^2/s)$ at high M^2. Secondly, this estimate does not explain
the large negative M^2/s spill-over in Fig. V.5 through V.7.

The 100 and 400 GeV/c cross sections in Fig. V.5 scale with
respect to M^2/s over its entire range, and are consistent with the
bubble chamber measurements at 195 GeV/c of Ref. 8. The low M^2/s
diffractive peak, characteristic of pp → pX data, is absent. See
Fig. V.7 for a comparison at M^2/s dependences of the pp and pn
cross sections at 400 GeV/c. As in the dσ/dt comparison outside
the diffractive pp → pX region, there is a difference in shape
and absolute value between the two cross sections. A 12% difference
in the absolute values can be attributed to the higher allowed
momentum transfer $(|t|<1.08$ GeV$^2)$ in the pp data plotted. However,
this does not account for the difference in shape and the total pp
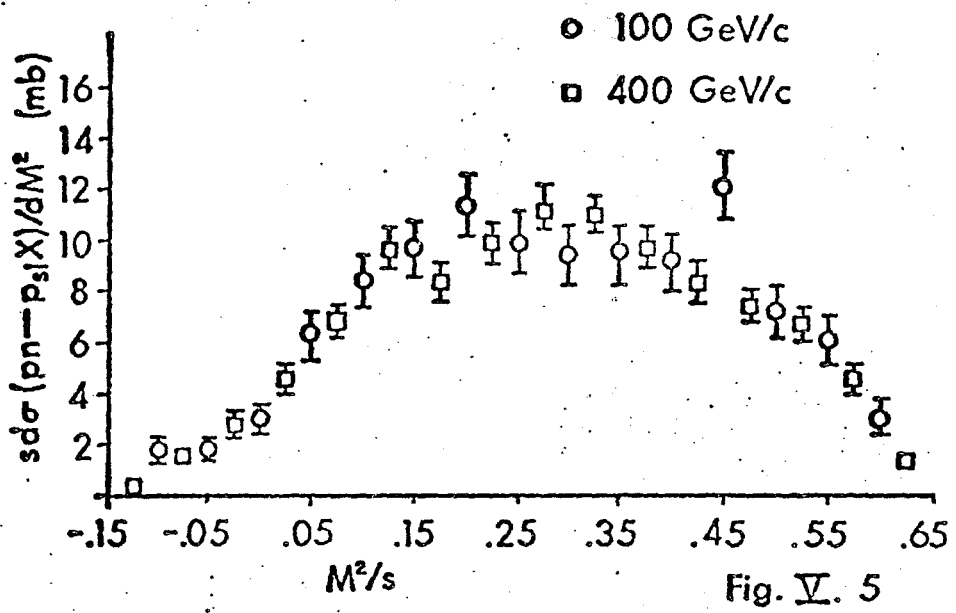
Fig. V. 5
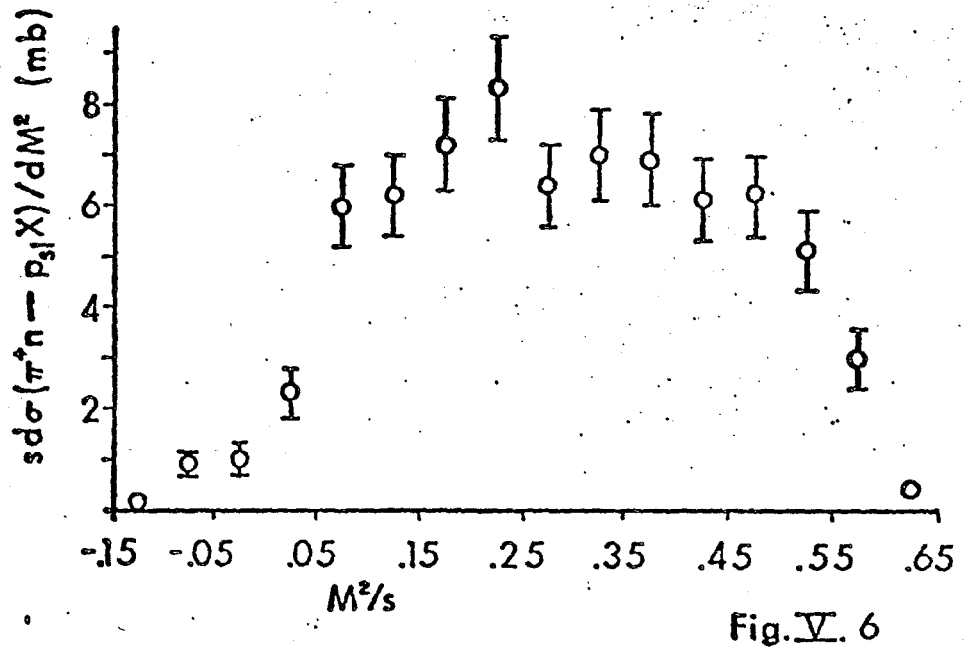
Fig. V. 6
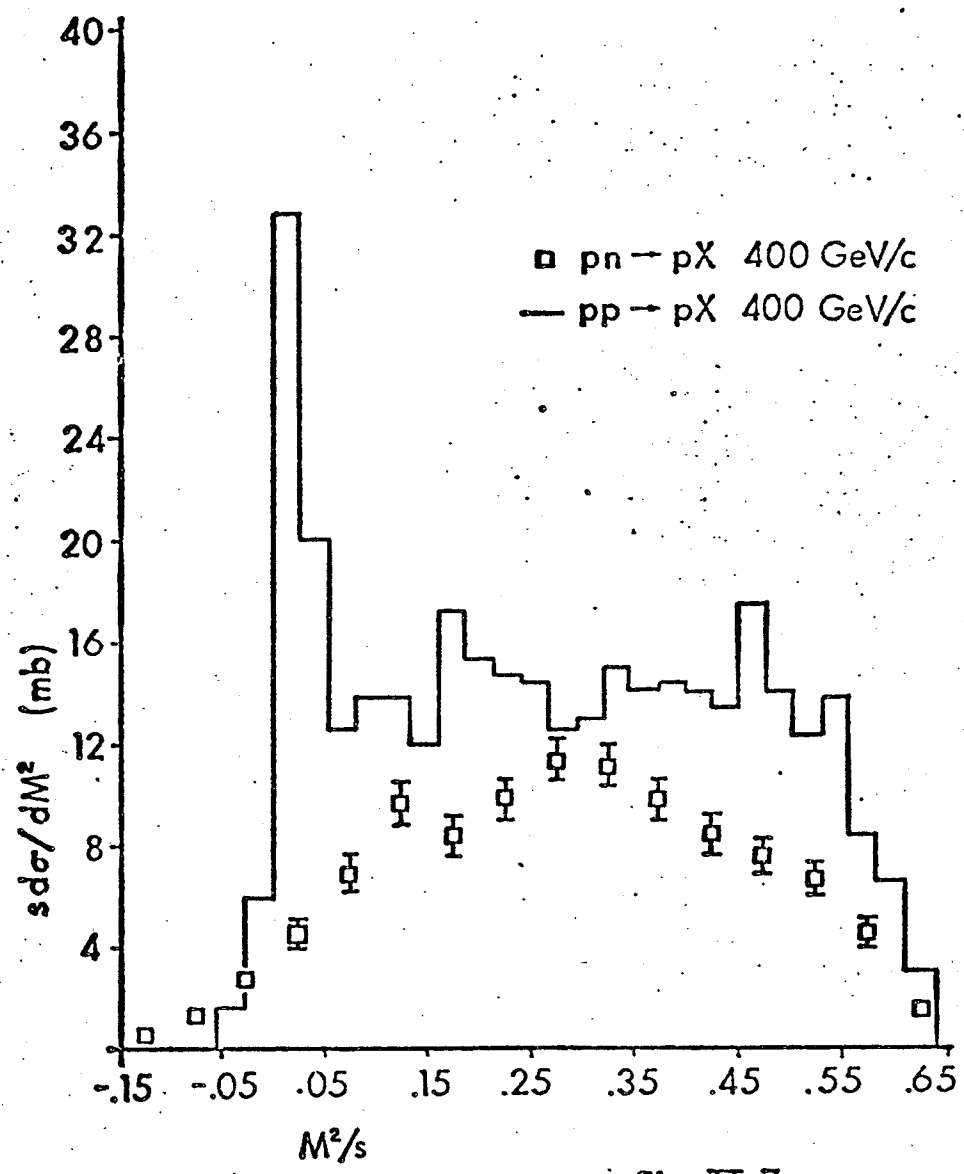
Fig. V.7

cross section excess.

The π^+n cross section in Fig. V.6 is seen to have the same form as the pn data, and Fig. V.8 shows that the ratio of the pion to proton beam inclusive cross sections is constant with respect to M^2/s. It is roughly equal to the ratio of the total cross sections. The ratio of the 100 to 400 GeV/c pn $\rightarrow$ pX cross sections is illustrated in Fig. V.9 and is about 1.0. The above scaling suggests that the production mechanisms are energy independent and independent of beam type.

The cross sections may also be studied as functions of M^2/s and t simultaneously. Figures V.10 through .12 show the M^2/s dependence as a function of t. The average value of $-t$ ($<-t>$) is given near each set of data points. The curves in Figures V.11 and .12 are predictions of the Fermi-smeared ROPE model. Those in Fig. V.10 have been drawn to guide the eye and are not model predictions. (The total $\pi\pi$ cross section is needed to apply the ROPE model to pion beam data, and it is not a directly measurable quantity.) We observe that the data in each t-bin has roughly the same shape for the different cross sections. In Figures V.13 and .14, where we have plotted both the 100 and 400 GeV/c pn $\rightarrow$ pX data, this effect is more strikingly seen. These cross sections scale with respect to M^2/s and t together. This is a much stronger statement of scaling than the previously observed scalings of the integrated cross sections with respect to M^2/s and t separately. A comparison of the π^+n to pn cross sections

$$R = \frac{d\sigma(\pi^+ n \to pX)/dM^2}{d\sigma(pn \to pX)/dM^2}$$

- - - - - $\dfrac{\sigma(\pi^+ n \to pX)}{\sigma(pn \to pX)}$

M^2/s

Fig. V. 8

$$R = \frac{d\sigma(pn \to pX, 100)/dM^2}{d\sigma(pn \to pX, 400)/dM^2}$$

- - - - - - - $\dfrac{\sigma(pn \to pX, 100)}{\sigma(pn \to pX, 400)}$

M^2/s
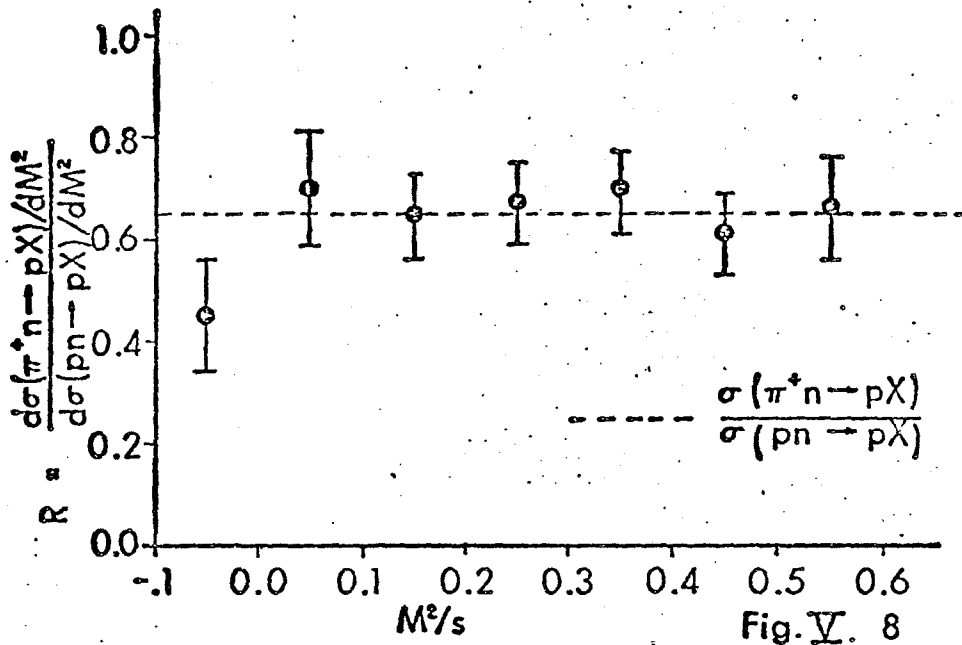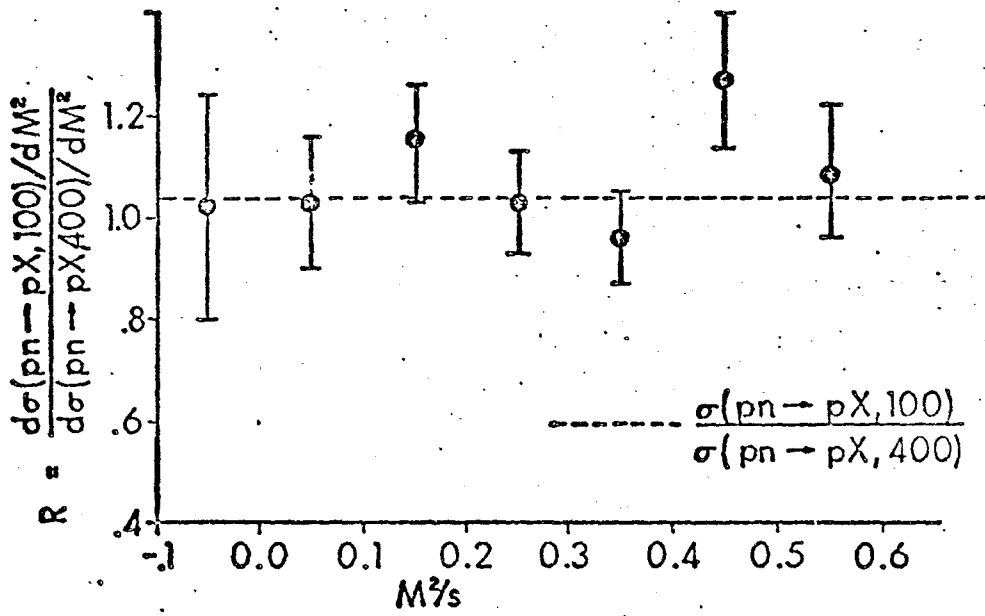
Fig. V. 9
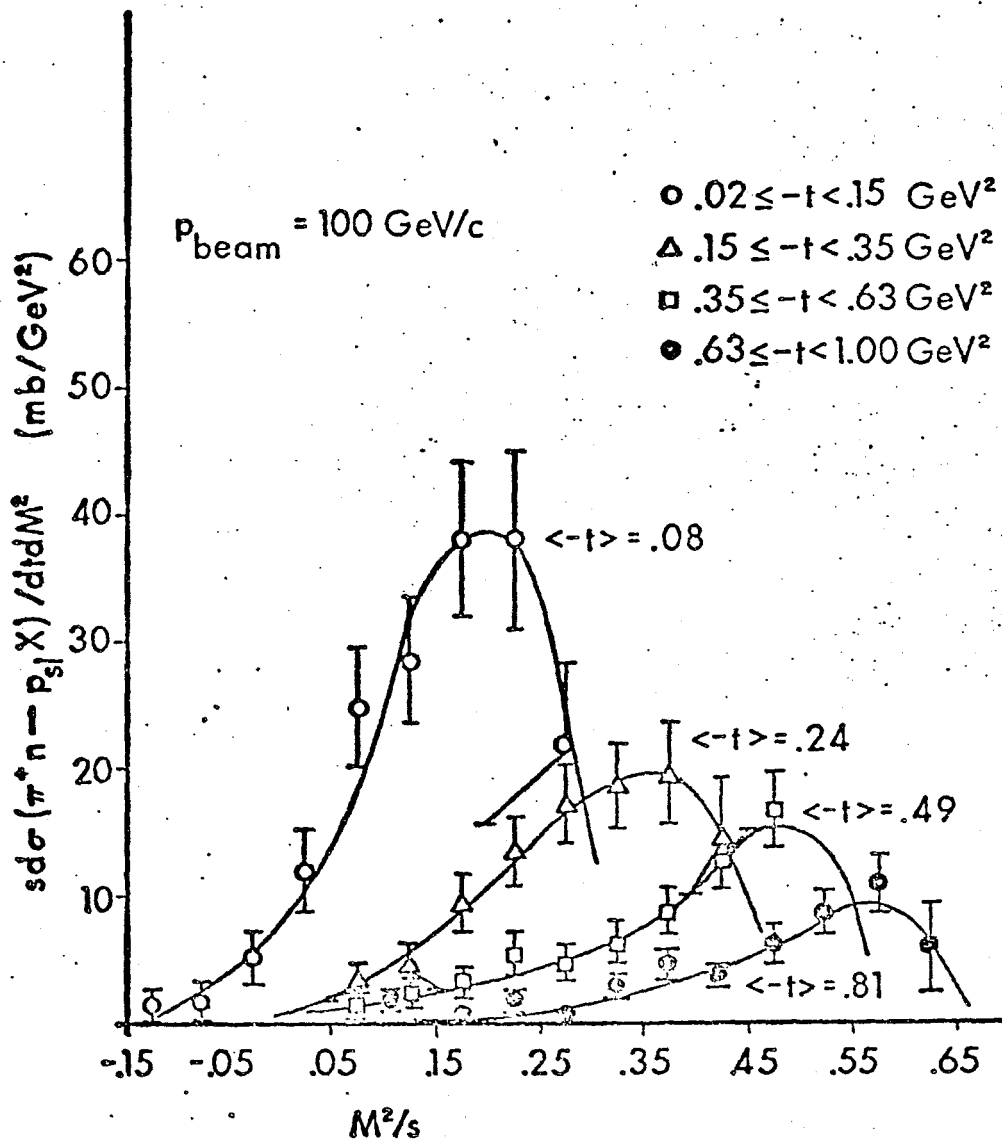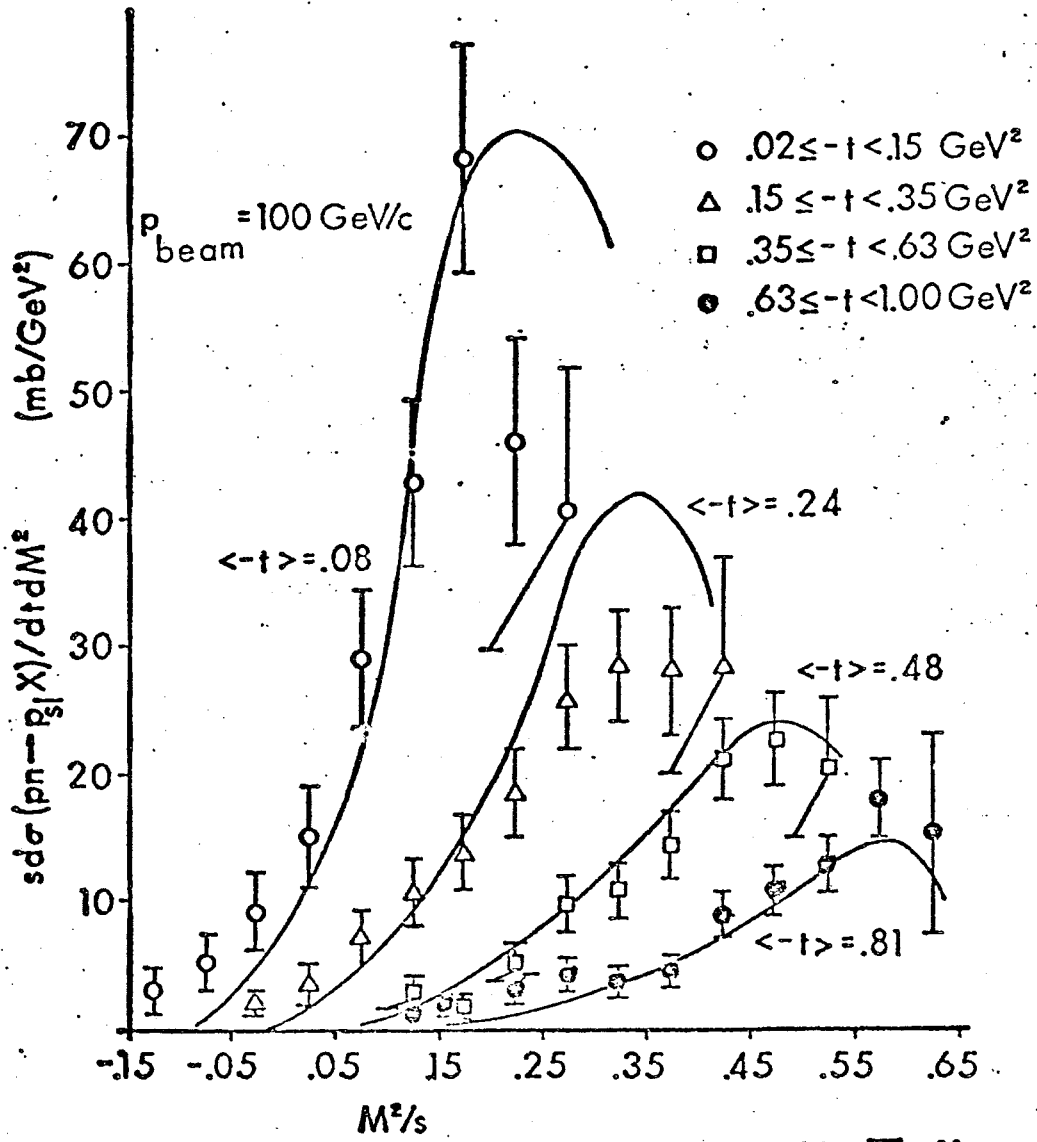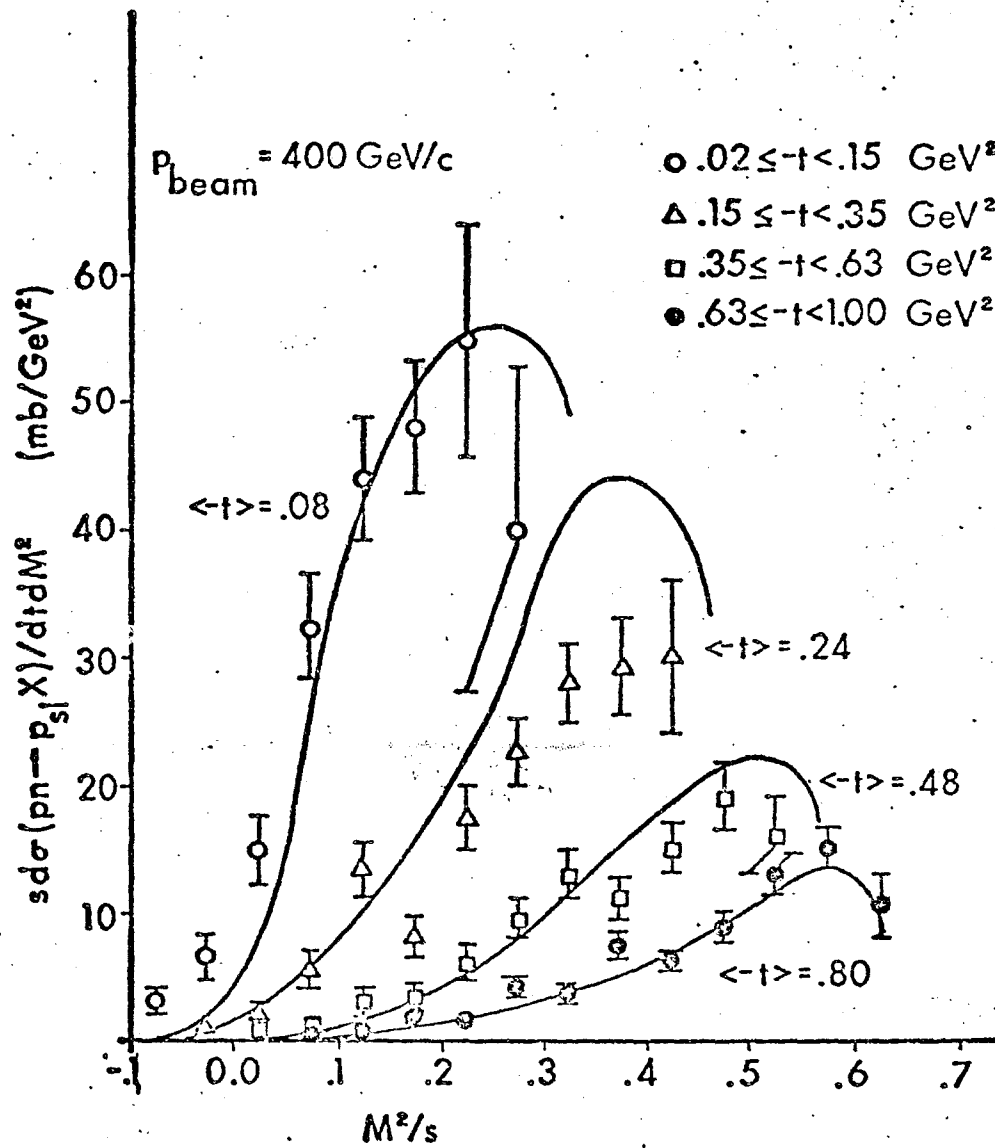
Fig. Ⅴ. 10

Fig. V. 11

Fig. $\underline{V}$. 12
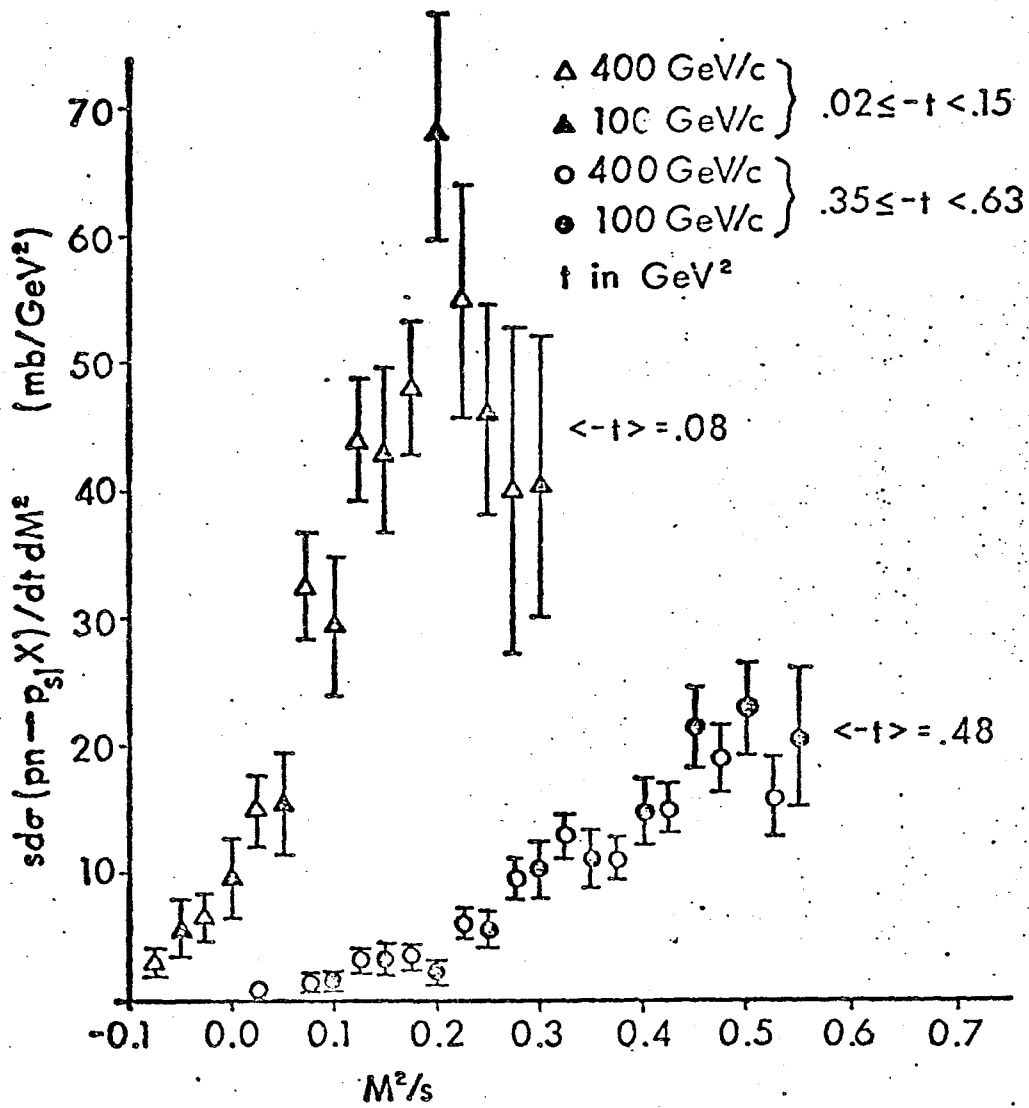
Fig. V. 13
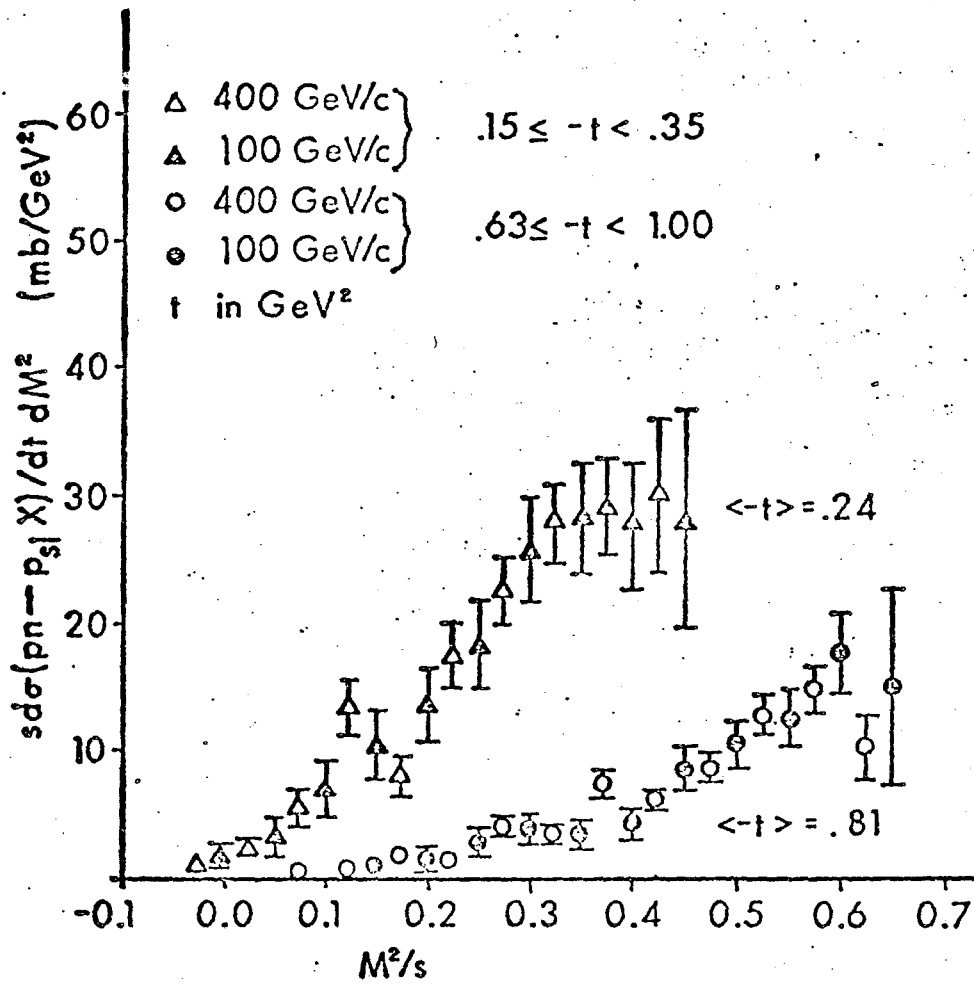
Fig. V. 14

made in the same manner, shows scaling in the ratio of $\sigma(\pi^+ n \to pX)/ \sigma(pn \to pX)$, as expected from factorization of the scattering amplitude.

The scaling has been observed at other energies as well. We present our results with those of Ref. 4 in M^2/s and t regions common to both experiments. See Fig. V.15 . The cross sections from the 2 different experiments scale nicely over a large range of beam momenta from 50 to 400 GeV/c. As our $\pi^+ n$ to pn cross section ratio satisfies the factorization hypothesis, and strong interactions are isospin invariant, we expect the cross section for pp → nX to equal our pn → pX cross section. However, ISR measurements[9] of the charge symmetric reaction are smaller by a factor of ~1/3. See Fig. V.16.

C. Mueller-Regge Analysis

1. Energy Dependence and Trajectories

In Appendix F, the Mueller-Regge phenomenology is briefly outlined. A general expression, Eq. V.4, is given for $sd\sigma/dtdM^2$ in the triple-Regge limit where $M^2 \to \infty$, $s/M^2 \to \infty$ and s, $M^2 >> t$.

$$sd\sigma/dtdM^2 = \frac{1}{s} \sum_{ijk} G_{ijk}(t)(s/M^2)^{\alpha_i(t) + \alpha_j(t)} (M^2)^{\alpha_K(0)} \qquad V.4$$

The α's are Regge trajectories and $G_{ijk}(t)$ contains the t-dependence of the triple-Regge couplings. We may integrate Eq. V.4 over M^2. The lower limit is m_b^2, the mass squared of the beam particle,
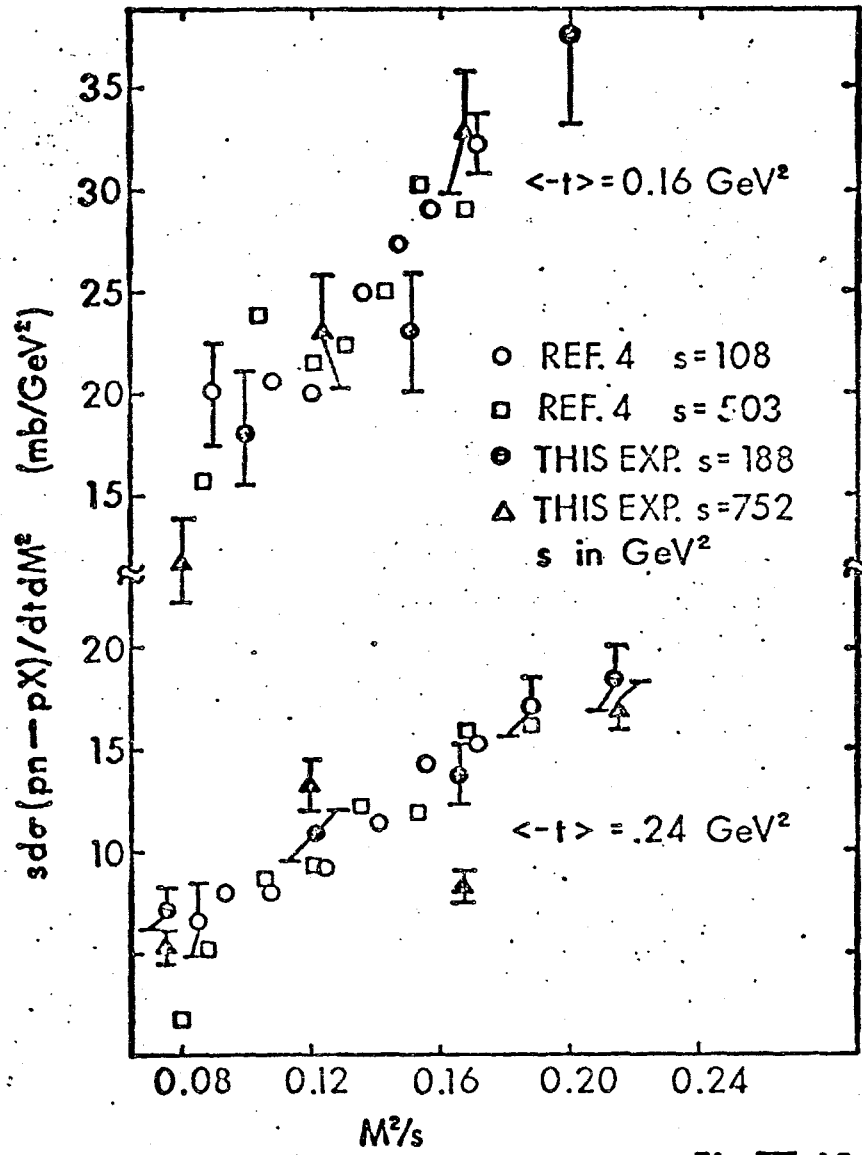
Fig. V. 15
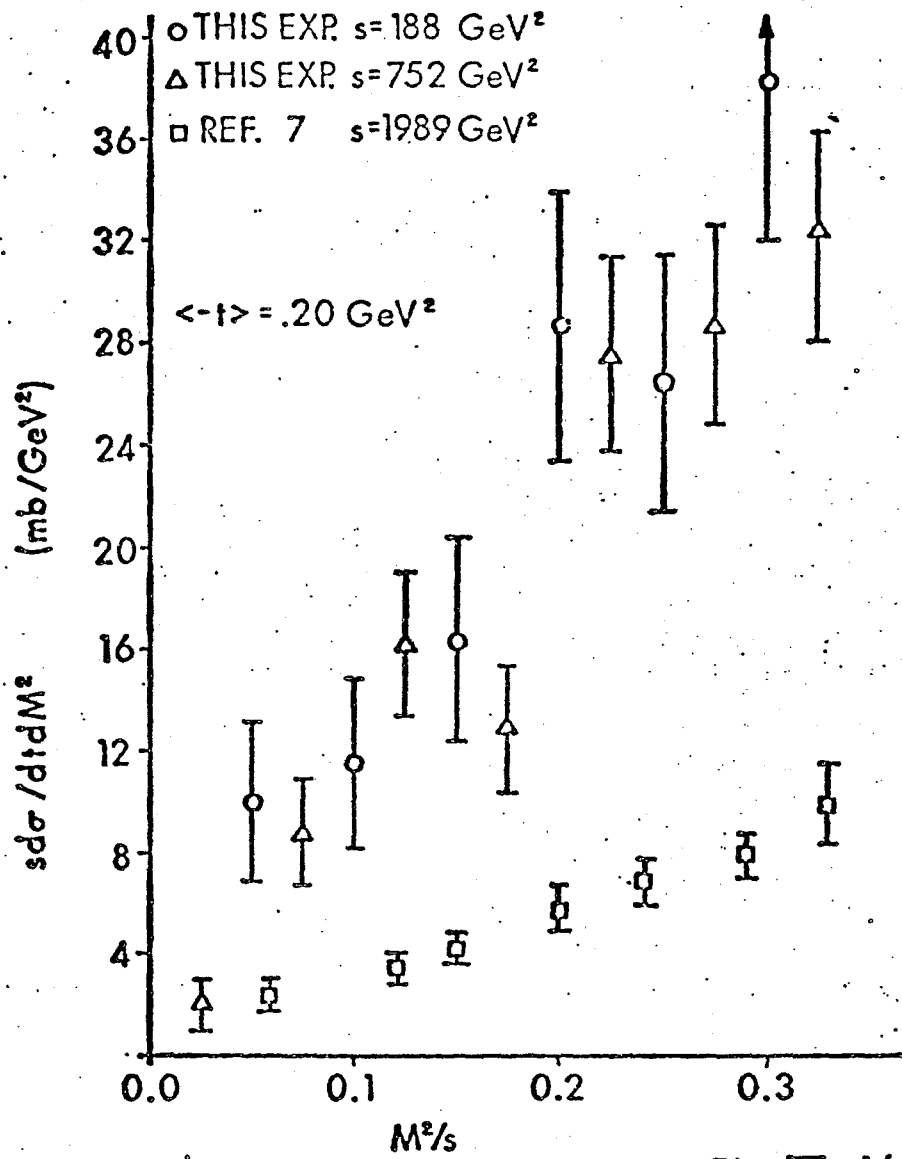
Fig. Ⅴ. 16

and the upper limit is cs, assuming the upper limit for M^2 to be proportional to s. The resulting $d\sigma/dt$ is given in Eq. V.5

$$d\sigma/dt = \sum_{ijk} \left[G_{ijk}(t)/ \delta(t) \right] c's^{\alpha_k(0)-1} \qquad \text{V.5}$$

where

$$\delta(t) \equiv \alpha_K(0) - \alpha_i(t) - \alpha_j(t) + 1 \qquad \text{V.6}$$

and $c' = c^{\delta(t)}$. The lower limit may be neglected as long as $\delta(t) > 0$, which will be true in our physical t-region for i, j or k being the pomeron (P), π or ρ trajectories given in Eq. F.15. Therefore, the energy dependence of $d\sigma/dt$ is determined solely by t the identity of the k-reggeon. Integrating over t does not effect the energy dependence, and we may write the following results:

$$\sigma \sim \text{constant} \qquad \text{if } k = P \qquad \text{V.7a}$$

$$\sigma \sim 1/s^{\frac{1}{2}} \qquad \text{if } k = \rho/A_2 \qquad \text{V.7b}$$

$$\sigma \sim 1/s \qquad \text{if } k = \pi \qquad \text{V.7c}$$

The constancy of the hn $\to$ pX cross sections throughout the Fermilab energy range indicates the dominance of ijP terms in Eq. V.4., where $\alpha_P(t)$ is assumed to have an intercept of 1.

A detailed study of the contributions from different triple-Regge couplings to high energy inclusive reactions, has been made

by Field and Fox.[10] They were unable to get a qualitative estimate of the importance of the interference terms, where $i \neq j$. For simplicity we assume α_i and α_j to be the same trajectories. It then follows that the double differential cross section in Eq. V.4 becomes

$$s d\sigma/dt dM^2 = \sum_i G_{iiP}(t) \; (s/M^2)^{2\alpha_i(t) - \alpha_P(0)} \qquad \text{V.8}$$

where $\alpha_P(0) = 1$.

If any one exchange trajectory α_i dominates, the s/M^2 dependence will reflect this dominance, and we then try to fit our data to the form.

$$s d\sigma/dt dM^2 \sim (M^2/s)^{1-2\alpha_E(t)} \qquad \text{V.9}$$

where $\alpha_E(t)$ is the effective trajectory.

2. Protons From Neutron Dissociation

In the above analysis leading to our decision to fit the data to the form in Eq. V.9, we have assumed that an "isolated" proton is produced via some charge exchange mechanism. See Fig. V. 17a. However, in Chapter IV we have shown that 3- and 4- prong proton beam events have a .3mb cross section for producing a slow proton in a $(p\pi^-)$ system from neutron dissociation. This process involves no charge exchange, as illustrated in Fig. V.17b. One would hope to be able to isolate these events from our charge

$$\Delta Q = 1$$
$$\Delta I = 1$$

Fig. $\underline{V}$. 17a

$$\Delta Q = 0$$
$$\Delta I = 0,1$$
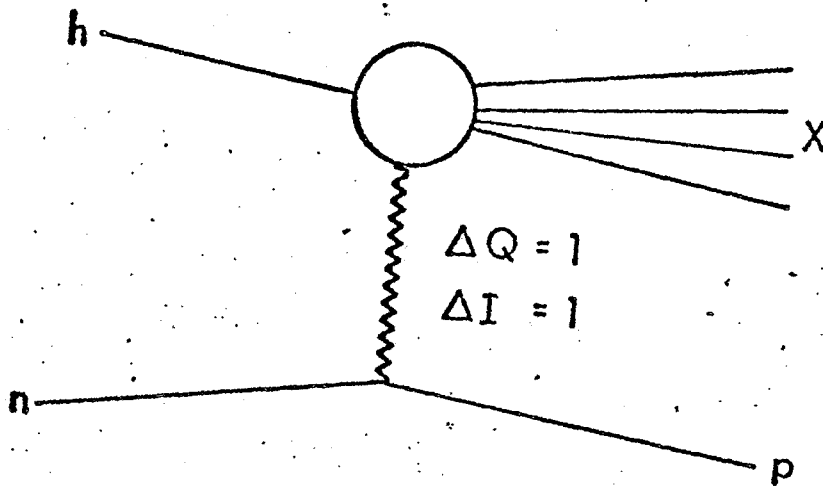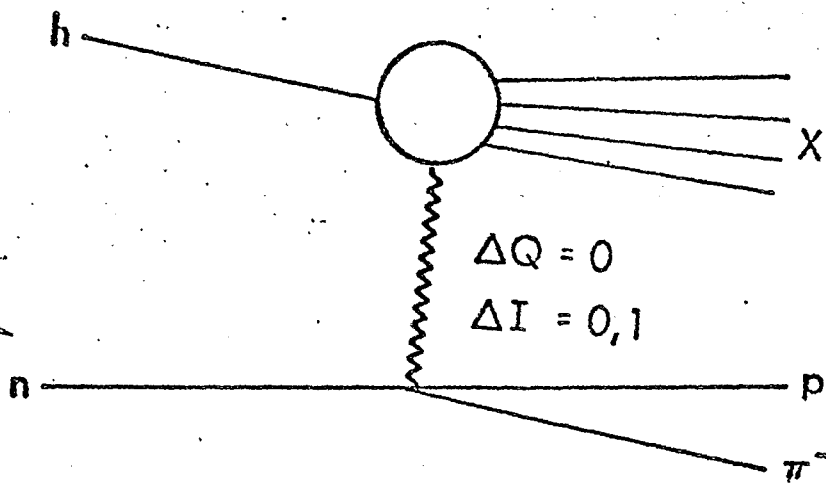
Fig. $\underline{V}$. 17b

exchange data, regardless of multiplicity.

Using our entire 3- and 4-prong neutron target (proton beam) event sample at 100 GeV/c, we have plotted the invariant mass of the ($p\pi^-$) system in Fig. V.18. We require both particles to be in the backwards CM hemisphere. A peak is seen in the $\Delta(1236)$ region, corresponding to an I=1 isospin exchange, and the majority of the remaining events are in the N^* (1470) region. Fig. V.19 shows the square of the missing mass recoiling from the ($p\pi^-$) system. A low mass peak is clearly seen and events in this peak ($MM^2 < 12.5$ GeV^2) are defined to have an unambiguous resonant ($p\pi^-$) system, which was produced by neutron dissociation. An $sd\sigma/dtdM^2$ plot is then made for these events, where M^2/s and t are calculated from the slow proton. See Fig. V.20. (The errors on the individual data points are large, on the order of 25%). It was hoped that these dissociation events would be found at large M^2/s values for each t-bin, as M^2 would be large for a system with a slow π^- and several fast other particles. Unfortunately, a clean M^2/s cut cannot be made on the data in Fig. V.20 and these events are included in the analysis.

3. Extracting the Effective Trajectory

An explicit attempt is made to account for the Fermi-smearing of the data when fitting for the effective trajectory. To do this, we have Fermi-smeared the $sd\sigma/dtdM^2$ form in Eq. V9.

For any particular α, we begin by generating a target momentum using a Monte Carlo program that reproduces a Hulthen
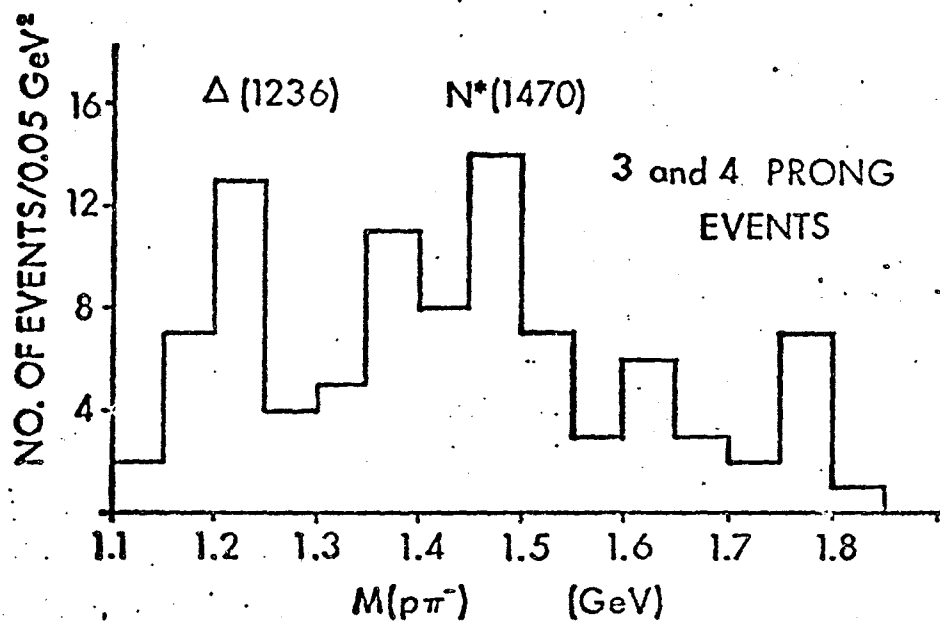
Fig. V. 18
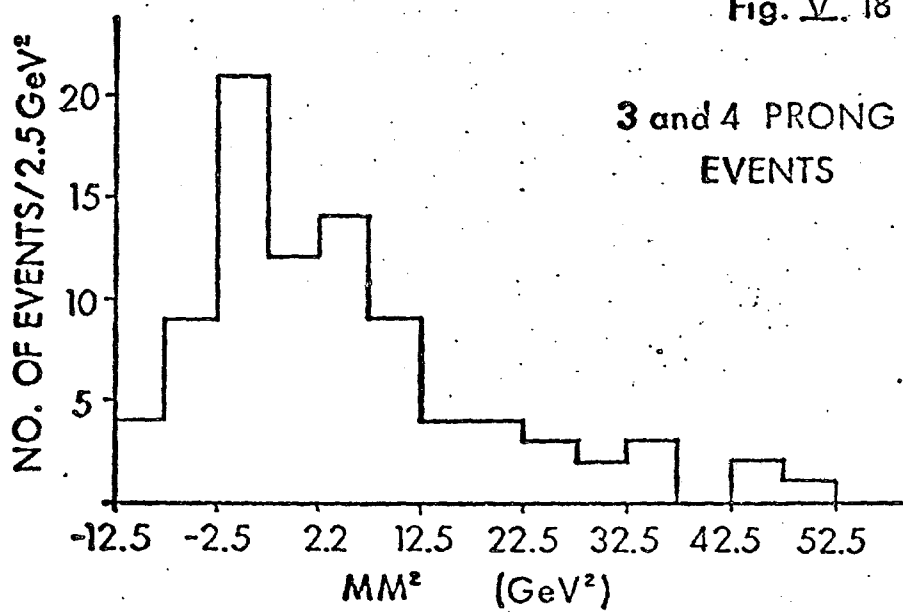
Fig. V. 19
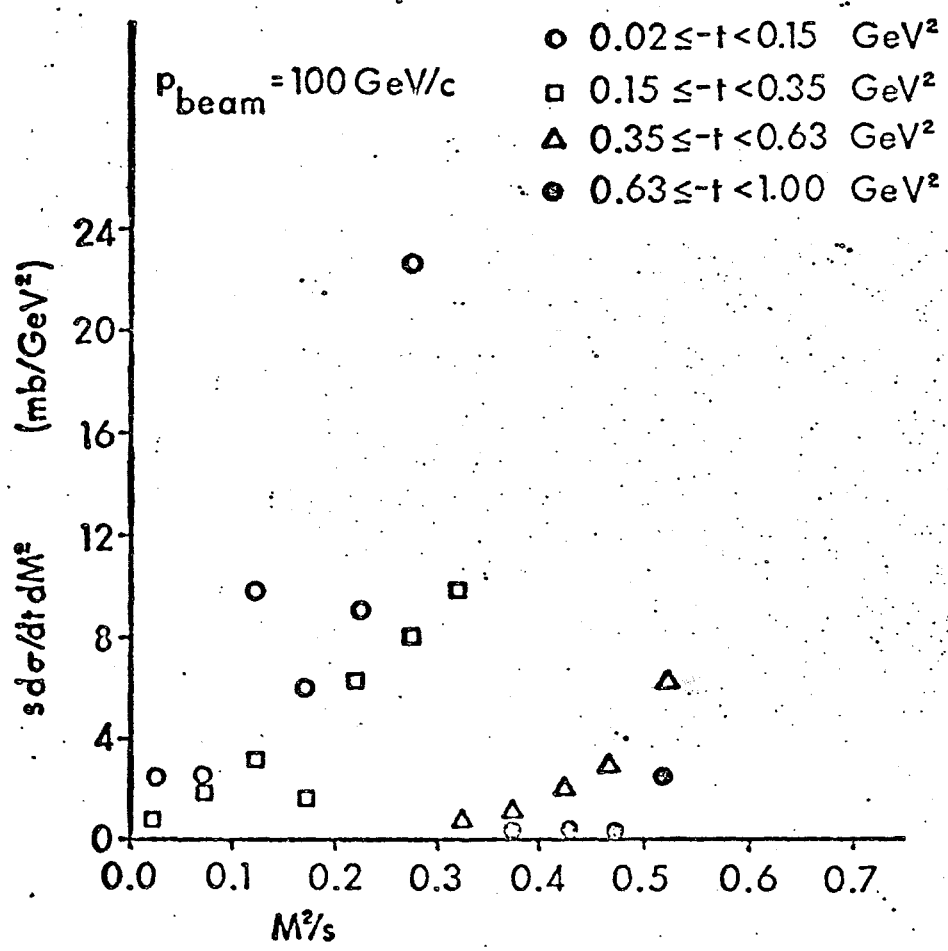
Fig. V. 20

target distribution. Using this target momentum and the measured beam momentum, s is calculated and a physical M^2 and t region can be defined. Values of M^2 and t are chosen as to uniformly populate this M^2 and t region, and these values uniquely define the slow proton momentum in the CM, up to an arbitrary azimuthal rotation about the beam. This azimuthal angle is uniformly generated, because it is needed to recalculate the kinematic variables for a stationary target as done below. Each generated Monte Carlo event is given a weight proportional to $sd\sigma/dtdM^2$ ($W=(M^2/s)^{1-2\alpha}$), and can be plotted at the true values of M^2/s and t.

In our experiment, however, the spectator proton is generally not seen if it has a momentum less than 80 or 100 MeV/c. As we assume the target to be at rest in these situations when processing the data, we recalculate s_o, t_o and M_o^2 in the same fashion, using a target at rest. The Monte Carlo event is then plotted with the true cross section weight, but at the smeared values of M_o^2/s and t_o. This smears the $sd\sigma/dtdM^2$ form of Eq. V.9.

The Fermi-smeared $sd\sigma/dtdM^2$ distributions are then fit to a quadratic polynomial for each t-bin. The fit, $F(M^2/s, <t>|\alpha)$, is made only over the range of M^2/s corresponding to the range of the data that will be used, and is normalized to unity. We identify F as being a normalized probability distribution for the chosen value of α. A summary of the t-bins and corresponding M^2/s ranges is given in Table V.3. The minimum M^2/s cut at 0.02 ensures that

TABLE V.3

t AND M^2/s CUTS

$<-t>$ [*]	$-t_{min}$	$-t_{max}$	$(M^2/s)_{min}$	$(M^2/s)_{max}$
0.057	0.02	0.10	0.02	0.20
0.147	0.10	0.20	0.02	0.29
0.263	0.20	0.33	0.02	0.38
0.418	0.33	0.51	0.02	0.45
0.618	0.51	0.73	0.02	0.52
0.857	0.73	1.00	0.02	0.58

[*] All values for t are in GeV^2, and the mean value for $-t$ is that of the combined 100 and 400 GeV/c $pn \rightarrow pX$ data.

TABLE V.4

FITTED EFFECTIVE TRAJECTORIES

DATA	a	b	χ^2/d.o.f.
$pn \rightarrow pX$, 100 GeV/c	0.27 ±0.07	1.18±0.16	1.45
$pn \rightarrow pX$, 400 GeV/c	0.25 ±0.06	1.03±0.13	1.93
$pn \rightarrow pX$, ALL	0.26 ±0.04	1.07±0.18	1.18
$\pi^+ p \rightarrow pX$, 100 GeV/c	0.29 ±0.08	0.98±0.18	2.05

M^2 be at least four times larger than the maximum value of t. The maximum cuts restrict us to a rectangular region of phase space for each t-bin below t_{min}, thus negating the effects of the t_{min} boundary.

For 6 different t-bins, curves were generated for α's ranging from -1 to +1 in steps of 0.01. For each t-bin and value of α we may use the normalized probability function to calculate a maximum likelihood[11] as in Eq. V.10.

$$\ell (X|\alpha) = \prod_i F(X_i|\alpha) \qquad\qquad \text{V.10}$$

The symbol X represents the total data set as a function of M^2/s for a particular <t>, and X_i is one particular observation (event) in that set. As shown in Table III.1, the processing weights for the data are close to unity and all events will be considered to have unit weight. The value of α with the maximum value of ℓ, α_{max}, is the most likely value of the Regge trajectory at t = <t>.

If the distribution of $L(X|\alpha) \equiv \log \ell(X|\alpha)$ is parabolic with respect to α, it means that $\ell(X|\alpha)$ has a Gaussian shape. We then take the error in α_{max} to be

$$\Delta\alpha = \alpha_{max} - \alpha_{1/2} \qquad\qquad \text{V.11a}$$

where

$$L(X|\alpha_{1/2}) \equiv L(X|\alpha_{max}) - \frac{1}{2} \qquad\qquad \text{V.11b}$$

This is equivalent to choosing a 68.3% confidence interval. For a non-parabolic $L(X|\alpha)$, this estimate of the error can be shown to be appropriate as long as $L(X|\alpha)$ is continuous and has only one maximum in the α-region of interest.

The values for α_{max} are plotted at the average values of t taken from the data. The deviation of <t> due to Fermi-smearing was found to be negligible. The resulting effective trajectories for the pn → pX data from this experiment are shown in Figs. V.21a and V.21b. The straight lines through the data are the results of least squares fits of the form $\alpha = a + bt$. These are summarized in Table V.4. The fact that the 100 and 400 GeV/c beam momentum trajectories are equal is to be expected because of the scaling exhibited by the data with respect to M^2/s and t. The trajectory for the 100 and 400 GeV/c pn data together is given in Fig. V.21c. The pion beam data yield a similar trajectory. This further supports the idea that the scattering amplitude factorizes into two functions depending only on the particles coupling at the beam and target vertices separately as in Fig. V.17a.

Most important, the intercepts of the trajectories are non-zero. A zero intercept and slope of 1.0 would indicate the dominance of pion exchange in charge exchange reactions at Fermilab energies. The trajectories have intercepts lying between the ρ/A_2 and π trajectories, and have a slope consistent with 1.0. See Fig. V.22 for the pn data trajectory. This contradicts the conclusions of analyses done in Refs. 7 and 8, where pion dominance was concluded,

100 GeV/c   pn → pX

(GeV²)

Fig. V. 21 a

400 GeV/c   pn → pX

(GeV²)

Fig. V. 21 b

100 and 400 GeV/c   pn → pX

(GeV²)
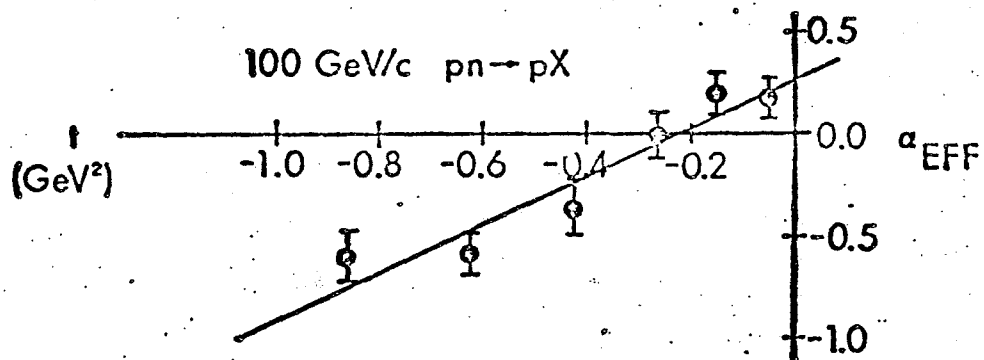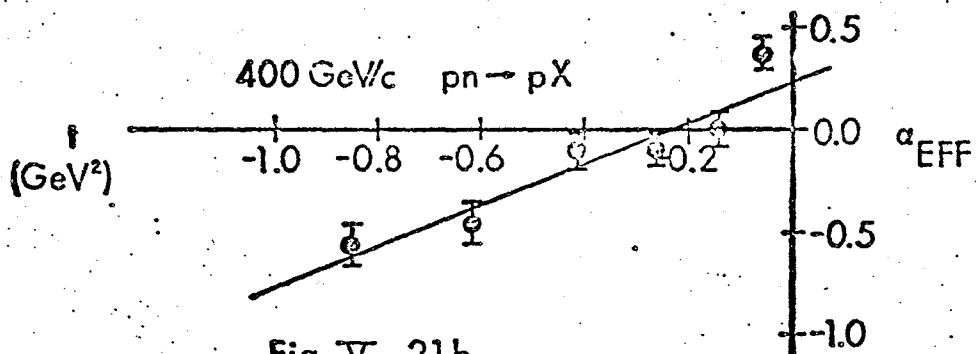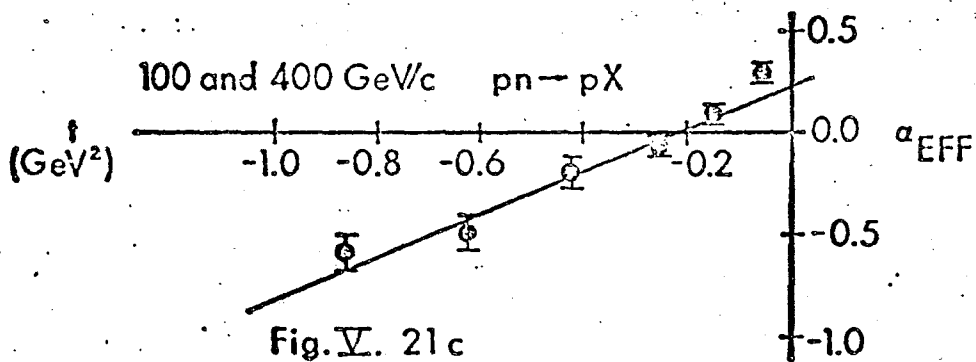
Fig. V. 21 c
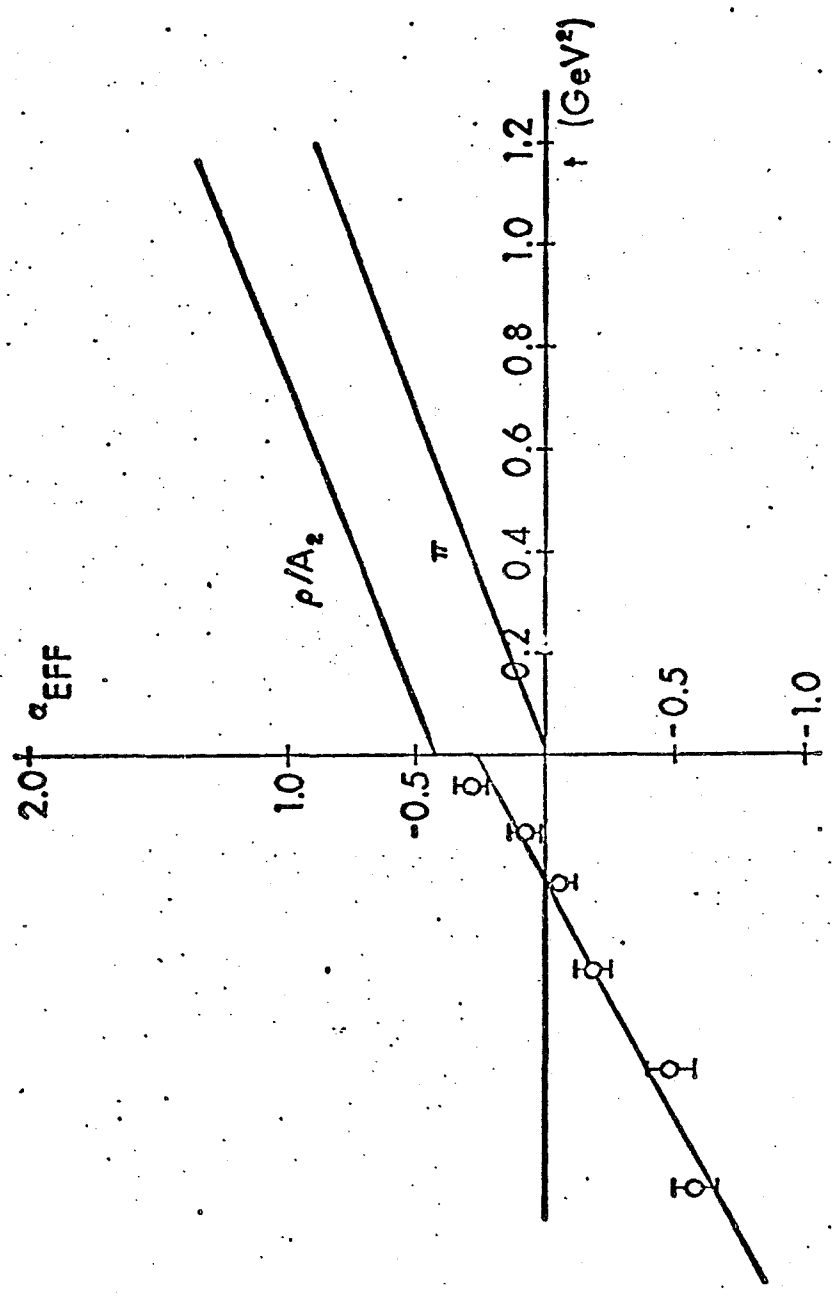
Fig. $\underline{V}$. 22

though the shapes of the M^2/s distributions were consistent with ours.

D. The ROPE Model

In previous work[1,2] at 100 GeV/c, we have compared the ROPE model (App. F) with our pn → pX data. For our reaction we use the form of the cross section given by Bishari.[1]

$$s d\sigma/dt dM^2 = \frac{1}{4\pi} \cdot \frac{g^2}{4\pi} \cdot \sigma_T(\pi p) \cdot \exp a(t - m_\pi^2)$$

$$\cdot \frac{|-t|}{(t - m_\pi^2)^2} (s/M^2)^{2\alpha_\pi(t) - 1}$$

V.12

Eq. V.12 is exactly Eq. F.18, where the beam particle is now a proton, the target a is a neutron, and c, the slow outgoing particle in the target fragmentation region, is a proton. It is identical to the triple-Regge prediction with just $\pi\pi\underline{P}$ and $\pi\pi R$ terms.

If the off-mass shell correction parameter a is assumed to be 0, Eq. V.12 gives a fair quantitative prediction of the data in Figs. V.11 and .12. The formula is Fermi-smeared, in a procedure similar to that described in the previous section, to produce the curves. While doing the smearing, we have calculated the r.m.s. and average deviations between the "true" and smeared values of M^2/s and t. The r.m.s. deviations are then used as estimates of our experimental resolution for M^2/s and t. For $\sigma(\pi p)$, we use the parametrization b + cM, where b = 22.48 mb and c = 17.16 mb/GeV. For g, the π-n-p coupling constant, we use a value

twice that of the pp coupling constant, because of isospin considerations. Therefore, $g^2_{\pi np}/4\pi \sim 29.0$.

On the other hand, Bishari suggests likely values for a to lie between 4 and 6 GeV^{-2}. In this case, at larger and larger values of t, the cross section given by Eq. V.12 would fall too rapidly and be inadequate in describing the large M^2/s data. The inclusion of RRP and RRR terms, e.q. ρ/A_2 trajectories, would help eliminate the cross section deficiency. We therefore contend that while the ROPE model with no off-mass-shell correction can approximate the data to some degree it is not a proof of pion exchange dominance. The best description of data was found to not have a pion trajectory. Furthermore, the effective trajectory extracted in Section V.C does not represent any known isospin exchange trajectory, and is at best the result of a mixing of the π and ρ/A_2 trajectory contributions.

E. Conclusions

The absolute cross section for the production of slow protons from a neutron target has been obtained for both pion and proton incident beam particles at 100 GeV/c, and for proton beams incident at 400 GeV/c. The cross sections are seen to have little energy dependence when compared with cross sections measured at other energies. They are also found to scale as a function of M^2/s and t in the ratio of the total inclusive cross sections. In an analysis of the proton beam data in terms of a general triple-Regge model, an effective Regge trajectory has been extracted.

The trajectory of $\alpha(t) = t + 0.25$ extracted is not a pion trajectory, and shows that at high energies proton production from a neutron target is not dominated by pion exchange. This contradicts the conclusions of the analyses of other experiments at high energies, though their data is similar in shape, if not in absolute normalization, to ours. We believe that our analysis has been the only one sensitive enough to accurately predict the non-zero intercept from the data available.

REFERENCES

1) M. Bishari, Phys. Lett. 38B, 510 (1972).

2) J.E.A. Lys et al., Phys. Rev. D16 3127 (1977).

3) W. S. Toothacker III, Thesis - "Proton-Proton Interactions at 400 GeV/c", UMBC 77-77 (University of Michigan, 1977).

4) B. Robinson et al., Phys. Rev. Lett. 34, 1475 (1975).

5) K. Abe et al., Phys. Rev. Lett. 31, 1527 (1973).

6) R.D. Schamberger, Jr. et al., Phys. Rev. D17, 1268 (1978).

7) J. Engler et al., Nucl. Phys. B84, 70 (1975).

8) Y. Eisenberg et al., WIS-77/33 Ph. (Weitzmann Institute of Science, Rehovot, Israel, 1977).

9) A. Engler et al., Nucl. Phys. B81, 397 (1974).

10) R.D. Field and G.C. Fox, Nucl. Phys. B80, 367 (1974).

11) W. T. Eadie et al., "Statistical Methods in Experimental Physics" (North-Holland Publishing Co., Amsterdam, 1971).

12) J. Hanlon et al., Phys. Rev. Lett. 37, 967 (1976).

APPENDIX A

Notation and Kinematics

A.1) <u>Physical Units</u> – In all calculations, we use a system of units where $h = c = 1$. Energy will be given in multiples of electron volts, e.g. 1 GeV = 10^9 eV. In this case, the corresponding units for momentum and mass are GeV/c and GeV/c^2.

A.2) <u>Four-Vectors</u> – Four-vectors are defined as

$$\tilde{a} \equiv (a_s, a_1, a_2, a_3) \qquad\qquad A.1$$

with the scalar product of two four-vectors

$$\tilde{a} \cdot \tilde{b} = a_o b_o - a_1 b_1 - a_2 b_2 - a_3 b_3 \qquad\qquad A.2$$

being invariant under a general Lorentz transformation or spatial rotation.[1] The four-momentum of a particle is

$$\tilde{p} = (E, p_x, p_y, p_z) \equiv (E, \vec{p}) \qquad\qquad A.3$$

the first vector component being the particle energy and the remaining three components its three-momentum.

A.3) <u>Coordinate Systems</u> – All coordinate systems used are orthogonal right-handed systems. The three used in the text are the wire chamber (WCCS), bubble chamber (BCCS) and the beam (BCS) coordinate systems. The physical orientations of the WCCS and BCCS are discussed in detail in Section II.C and Appendix D. The BCS is defined as having an x-axis parallel to the beam direction; the

136

y and z directions are perpendicular. The orientation of the z-axis is chosen to be roughly parallel to the bubble chamber z-axis. Note:

A beam track points in the general direction of the negative x-axis in the bubble chamber system.

A.4) Reference Frames — The two reference frames most referred to are the laboratory (LAB) and center-of-mass (CM) frames. The LAB is the frame in which the deuteron is at rest, e.g. $\tilde{P}_d = (m_d, 0)$, where m_d is the mass of the deuteron. (This is not the same as the rest frame for either an internal proton or neutron target.) The CM may be defined by the condition

$$\vec{P}_b^* + \vec{P}_t^* = 0 \qquad\qquad A.4$$

where the b and t subscripts indicate the beam and target vectors and the * superscript the use of CM values. No superscript will normally mean LAB values.

A.5) Coordinate Variables — The nomenclature for angles is as follows. ϕ and λ will signify the azimuthal angle in the film (x-y) plane and the dip the angle out of the plane, towards or away from the cameras. See Figure A.1. Three momentum components can be written as

$$P_x = p \cos \lambda \cos \phi \qquad\qquad A.5a$$

$$P_y = p \cos \lambda \sin \phi \qquad\qquad A.5b$$

$$P_z = p \sin \lambda \qquad\qquad A.5c$$
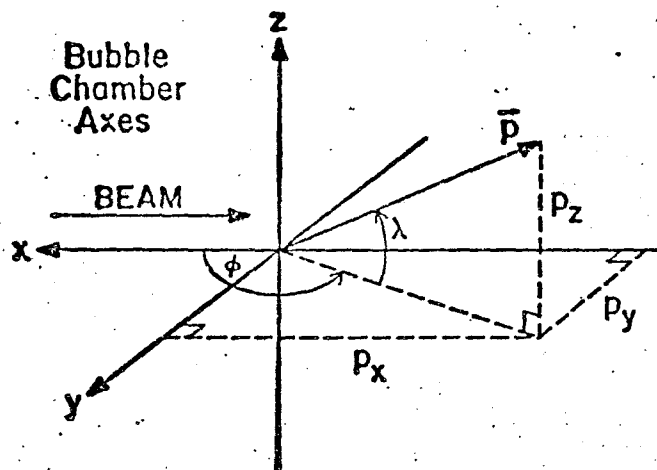
Fig. A.1
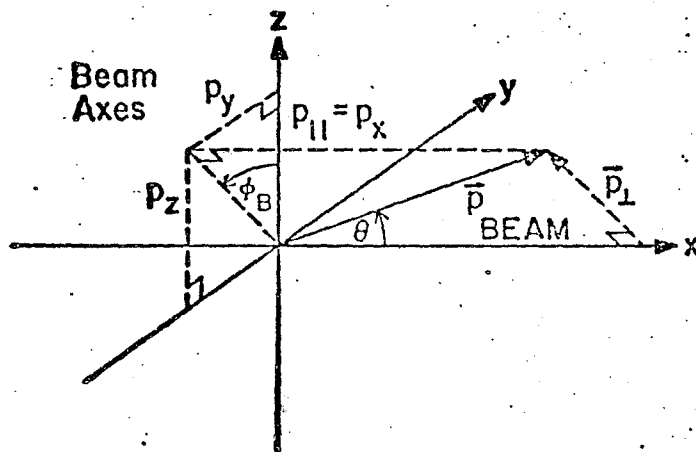
Fig. A.2

where p is the three-vector magnitude.

Two additional angles may be specified with respect to the beam system, ϕ_b and θ. In Figure A.2, ϕ_b is measured radially about the beam in the y-z plane from the z-axis and θ is the angle between a vector and the x-axis (beam direction).

A.6) TVGP and SQUAW Variables — the TVGP and SQUAW programs use variables picked to minimize the correlations in their errors. They are

$$\phi = \phi \qquad\qquad \text{A.6a}$$

$$s = \tan \lambda \qquad\qquad \text{A.6b}$$

$$k = 1/ (p \cdot \cos\lambda) \qquad\qquad \text{A.6c}$$

or azimuth, slope and curvature of a track. The azimuth is the same as described in Section A.5. The variable s is the slope of the track out of the film-plane. The curvature of a charged particle in a constant magnetic field is inversely proportional to its momentum, such that k may be thought of as the track curvature projected in the film-plane.

A.7). Longitudinal and Transverse Components — The components of momenta parallel and perpendicular to the beam in any frame for a particle with momentum $\vec{p}$ in that frame are

$$P_{\parallel} = \vec{p} \cdot \hat{P}_B \qquad\qquad \text{A.7a}$$

and

$$\vec{P}_{\perp} = \vec{p} - (\vec{p} \cdot \hat{P}_B) \, \hat{P}_B \qquad\qquad \text{A.7b}$$

where p_B is the unit vector in the direction of the beam momentum.

A.8) Total CM Energy —

$$E^*_{TOT} \equiv \sqrt{s} = \left[(\tilde{p}_b + \tilde{p}_t)^2 \right]^{\frac{1}{2}}$$

A.8

It is a Lorentz and rotationally invariant quantity.

A.9) Momentum Transfer and Missing Mass — In studying inclusive reactions of the type

$$b + t \rightarrow c + X$$

A.9
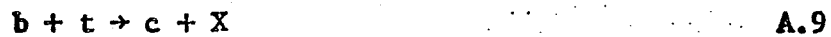
where c can be a single particle or system of particles and X designates the remaining particles, two particularly useful invariant quantities can be defined.

$$t = (\tilde{p}_t - \tilde{p}_c)^2$$

A.9a

$$M^2_X = (\tilde{p}_b + \tilde{p}_t - \tilde{p}_c)^2$$

A.9b

The four-momentum transferred between the target and c, the system of interest, is t, and M^2_X is the mass squared of system X recoiling against particle c (missing mass squared).

M^2, t and s uniquely define the kinematics of reaction A.9, up to an arbitrary rotation about the beam direction. For given values of s and M^2_X, t has a minimum possible value. Fig. A.3 shows the t-min boundary as a function of M^2_X for 100 and 400 GeV/c beam particles incident on neutron targets at rest. This kinematic
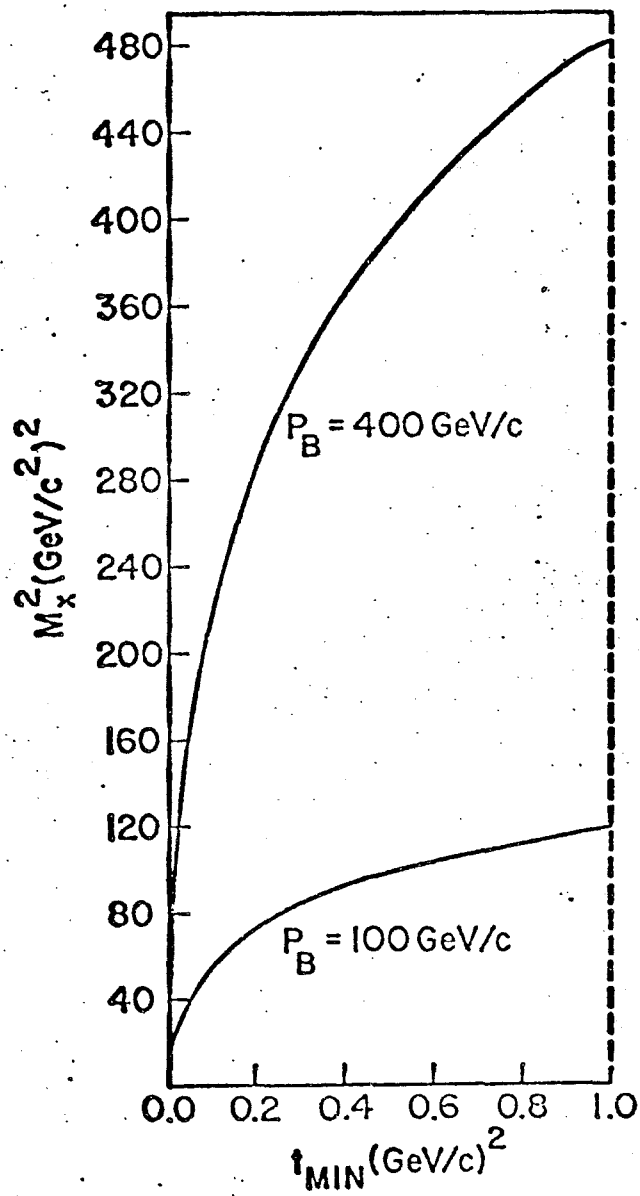
Fig. A.3

boundary is taken into account during data analysis.

A.10) Feynman x_F - The Feynman scaling variable is used to define particle momentum spectra in much of the literature.

$$x_F \equiv 2p_\parallel^* / \sqrt{s} \qquad \text{A.10}$$

The maximum and minimum longitudinal momenta in the CM is $\pm p_b^*$ giving x_F a range from -1.0 to 1.0. It may also be related to the missing mass by expression A.11 at high energies (large s).

$$x_F \approx 1 - M_x^2 / s \qquad \text{A.11}$$

A.11) Invariant Cross Sections - The Lorentz invariant phase space element is $d^3\vec{p}/E$ where $\vec{p}$ has the components

$$\vec{p} = (p_\parallel, \; p_\perp \cdot \sin \phi_b, \; p_\perp \cdot \cos \phi_b) \qquad \text{A.12}$$

in the beam coordinate system. If the beam and target are unpolarized we may assume isotropy with respect to ϕ_b. Integrating over ϕ_b, equivalent Lorentz-invariant phase space elements may be defined.

$$\int_0^{2\pi} (d^3\vec{p}/E) \; d\phi_b = \frac{\pi dp_\parallel d^2 p_\perp}{E} = \frac{\pi \sqrt{s}}{2E} dx d^2 p_\perp = \pi d(M^2/s)dt \qquad \text{A.13a}$$

For reaction A.9, a Lorentz-invariant differential cross section may then be written in terms of t, s and M^2.

$$f_{bt}(\tilde{p}_c) = E_c \frac{d^3\sigma}{d^3\vec{p}} \; (b+t \to c+x) \quad = \frac{1}{\pi} \frac{d^2\sigma}{d(M^2/s)dt} \qquad \text{A.13b}$$

(The π^{-1} factor will be omitted when quoting the invariant cross sections of this form in the text.)

A.12) <u>Means</u> – The mean of the value x for a data set will be

$$\langle x \rangle \equiv \sum_i x_i W_i \ / \ \sum_i W_i \qquad\qquad \text{A.14}$$

where we sum over the entire set and W_i is the weight for that particular value. The root mean square (r.m.s.) deviation from the mean and the error in the mean are given in Eqs. A.15.

$$\text{rms }(x) = \left[\sum_i W_i \, (x_i - \langle x \rangle)^2 / \sum_i W_i \right]^{\frac{1}{2}} \qquad\qquad \text{A.15a}$$

$$\delta \langle x \rangle = \text{rms }(x) \ / \ (\sum_i n_i)^{\frac{1}{2}} \qquad\qquad \text{A.15b}$$

where n_i is the number of unweighted events at each value x_i.

REFERENCES

1. The following are two general references on relativistic

    kinematics:

    R. Hagedorn, "Relativistic Kinematics" (W.A. Benjamin,

    Reading, Mass., 1973);

    E. Byckling and K. Kajante "Particle Kinematics" (John

    Wiley and Sons, New York, 1973).

APPENDIX B

SURVEY

The program SURVEY determined the values R_i defined in Section II.C by using the wire chamber information from 526 "good" beam tracks with the magnetic field turned off. By "good" beam tracks we mean those that are non-interacting and cause only one wire hit in each plane. As planes 4, 5, 11 and 12 are used to define the x-axis, they have R_i's of 0.0 and the beam tracks have a straight trajectory which may then be calculated using the hits on these planes. The hits on the remaining planes may then be used to calculate the non-zero R values. See Table B.1 for x, $\dot{R}$ and ω values for each plane as defined in Section II.C.

The uncertainty in the R values based on statistics should be about ± 50 microns. However, values of R can be affected by as much as 120μ by the residual field in the magnet, estimated to be as much as 42 gauss. We then assign an uncertainty of 120μ.

We may also feed the SURVEY program "good" field-on beam track data once the values for the PWC plane parameters have been determined, and use this data to determine an average beam momentum value. Two straight trajectories are calculated, one for the upstream chambers and one for those downstream, which are not within the magnetic field. The upstream

trajectory with a momentum estimate is the swum through the field and a fit made to the downstream trajectory. The momentum yielding the best fit is the momentum for that beam track. A value of 97.7 ± 0.4 GeV/c was obtained for RUN 1, the largest contribution to the error coming from the uncertainty in the R values.

TABLE B.1

WIRE CHAMBER PARAMETERS

PLANE	x (m)	R (m)	ω (rad)
4	−175.3640	0.00000	3.66519
5	−175.3320	0.00000	2.61799
6	−175.3000	−0.00096	1.57080
7	−15.8640	−0.00715	4.19810
8	−15.8320	−0.00275	3.15090
9	−15.8000	0.00449	2.10370
10	−2.5760	0.00047	1.04400
11	−2.5440	0.00000	−0.00320
12	−2.5120	0.00000	5.23280
13	1.9345	−0.00670	3.14136
14	1.9562	0.00751	0.00000
15	1.9948	−0.00603	2.09424
16	2.0329	0.00169	1.04712
17	2.2818	−0.00342	3.92700
18	2.3199	−0.00830	2.87900
19	2.3580	−0.00400	1.83326
20	2.9250	−0.00823	3.66492
21	2.9630	−0.00921	2.61800
22	3.0080	0.00023	1.57068
23	3.0300	0.00060	4.71204
24	5.7508	0.00890	4.58229
25	5.7889	0.04385	3.53510
26	5.8111	−0.04330	0.39349
27	5.8492	0.03602	2.48790
28	5.8714	−0.03504	5.62940

APPENDIX C

FIDROT

To align the bubble chamber and PHS to the high degree of accuracy required, non-interacting beam tracks in a field-on bubble chamber are measured. Given the beam momentum and plane coordinates as determined by the program SURVEY, FIDROT generates new translation constants and a rotation matrix. The beam tracks are swum upstream and downstream from the bubble chamber using the initial translation and rotations in Section II.C and generate wire hits on all wire chamber planes. By adjusting the input rotation and translations, FIDROT minimizes the discrepancies between the actual and generated hits.

This procedure was done for one hundred beam tracks. Table C.1 lists the results for transforming from the wire chamber to the bubble chamber reference system, the rotation by π around the z-axis not being included in the rotation matrix. These numbers are part of the input to PWGP where the reconstructed wire chamber tracks must be put into the bubble chamber system. One should note that an error in 1 mrad at the center of the bubble chamber is a 6 mm or 3 wire discrepancy in the last downstream chamber.

TABLE C.1

FIDROT PARAMETERS

$y_{PWC} - y_{BC}$ 0.0788 m

$z_{PWC} - z_{BC}$ -0.1847 m

$$\text{ROT (PWC} \rightarrow \text{BC)} = \begin{pmatrix} 0.9999789 & 0.0031280 & 0.0019956 \\ -0.0031407 & 0.9999351 & 0.0066358 \\ -0.0019757 & -0.0063642 & 0.9999438 \end{pmatrix}$$

Rotation matrix is in radians.

APPENDIX D

Scan Corrections

Several corrections must be applied to the raw scan data in order to produce the final multiplicity distributions. The net effect of all corrections is to lower the mean multiplicity defined in Eq. D.1

$$N = \sum_N NW_N / \sum_N W_N \qquad\qquad D.1$$

where N is the event multiplicity and W_N the number of events with that multiplicity, by an amount comparable to the error in the mean. For simplicity, the error in W_N is taken to be the square-root of W_N.

D.1 Uncountable Event Error Assignments

In assigning error quantities to the distributed uncountable events, we should take into account possible systematic errors; the total error should be larger than the statistical error. See Section II.D for a treatment of these uncountable events. An estimate of the systematic error may be obtained by using only the lowest odd or odd-plus-even prong counts in the prong estimates. One half the difference of the means will be called the "systematic" error. This number will be small if the range over which the prong number is estimated is small and vice-versa. It is therefore a qualitative measurement of the "goodness" of the prong estimates.

On a multiplicity-by-multiplicity basis for uncountable events, the statistical error for each multiplicity class is

multiplied by a single factor such that the error in the mean will equal the root mean square sum of the statistical and and systematic errors. At 400 GeV/c, a factor of 2.9 is required for the odd prongs, and 3.6 for the odd-plus-even prongs to reproduce systematic errors of .54 and .69 respectively. These factors are large but effect only the 10% of the scanned data that is incountable.

D.2 Short Stub Correction

To eliminate possible biases in the odd-prong multiplicity distribution arising from a multiplicity dependent visibility function for proton stubs, all even n-prong events with stopping tracks less than 5 mm in length will be considered (n-1)-prong events. This increases the odd-to-even prong event ratio from .25 to .28 but has no effect on the odd and hd (odd + even) mean multiplicities. Table D.1 contains the probability distribution for an even prong event to have a stub, used in correcting the scan data. It was taken from our measured inclusive data sample. The high value for $p(4)$ may be attributed to a sizeable 4-prong coherent deuteron cross section.[1]

D.3 Missed Dalitz Pair Correction

To calculate the number of Dalitz pairs in the sample, we calculate n_{π^0}, the number of produced π^0's, using a parametrization[2] of π^0 production in pp events as a function of the negative particle multiplicity. See Eq. D.2.

TABLE D.1

SHORT STUB PROBABILITY

PRONGS	P_{SHORT} (%)
4	13.6±1.1
6	9.3±0.9
8	10.0±0.9
10	9.1±0.9
12	7.9±0.9
14	10.1±1.2
16	8.4±1.4
18	8.4±1.8
20	4.9±1.8
22	1.4±1.4
24	0.0
26	4.5±4.5

$$\langle n_{\pi^0} \rangle = .70 \langle n_- \rangle + 1.5 \qquad \text{D.2}$$

For an hd reaction where the beam h is positively charged

$$n_- = (n_N - 2)/2 \qquad \text{D.3}$$

where n_N is the event multiplicity, and Eq. D.4 follows.

$$\langle n_{\pi^0,N} \rangle = \langle .35 n_N \rangle + .5 \qquad \text{D.4}$$

The number of expected or TRUE Dalitz pairs is then

$$n_D^{TR} = n_{\geq 3} \cdot BR \cdot \langle n_{\pi^0} \rangle \qquad \text{D.5}$$

where $n_{\geq 3}$ is the number of events in our sample and BR the branching ratio for $\pi^0 \rightarrow \gamma e^+ e^-$. The fraction of Dalitz pairs missed is

$$f_D^M = (n_D^{TR} - n_D^{OB})/ n_D^{TR} \qquad \text{D.6}$$

the superscript OB meaning observed events. Using Eqs. D.4 and D.6, the true number of N-prong primary events corrected for missed Dalitz pairs is written as

$$n_N^{OB} = n_N^{TR} - n_N^{TR} \cdot n_{\pi^0,N} \cdot f_D^M \cdot BR$$

$$\qquad \text{D.7}$$

$$+ n_{N-2}^{TR} \cdot n_{\pi^0,N-2} \cdot f_D^M \cdot BR$$

The correction to n_N^{OBS} to produce n_N^{TR} is given in Eq. D.8

$$\Delta n_N \equiv n_N^{TR} - n_N^{OB} = f_D^M \cdot BR \cdot (n_N^{TR} \cdot n_{\pi^o,N} - n_{N-2}^{TR} \cdot n_{\pi^o,N-2})$$

$$\simeq f_D^M \cdot BR \cdot (n_N^{OB} \cdot n_{\pi^o,N} - n_{N-2}^{OB} \cdot n_{\pi^o,N-2})$$

D.8

The missed fraction of Dalitz pairs is large, on the order of .7, but only lowers the odd and hd multiplicities by 0.06.

D.4 Vee Corrections

Vee corrections are made in the same manner as the Dalitz corrections. Equation D.4 can be used to find the γ multiplicities

$$<n_{\gamma,N}> = 2 \cdot <n_{\pi^o,N}> = .7n_N + 1.0$$

D.9

and from Ref. 2, Fig. 86 we find that

$$<n_{K^o_S,N}> = .01<n_N> + .14$$

D.10a

and

$$<n_{\Lambda,N}> = .10$$

D.10b

independent of multiplicity.[3,4,5] The mean lives ($c\tau$) in centimeters are 2.68 and 7.73 for K^o_S and Λ respectively, with Feynman x_F distributions peaking at 0.0 for the kaons at 100 and 300 GeV/c and $x_F = \pm 0.5$ (0.3) for lambdas at 100 (405) GeV/c.

Using a Lorentz transformation

$$\begin{pmatrix} E \\ P \\ \vec{P} \end{pmatrix} = \begin{pmatrix} \gamma & -\eta & 0 \\ -\eta & \gamma & 0 \\ 0 & 0 & 1 \end{pmatrix} \begin{pmatrix} E^* \\ P^*_{\parallel} \\ \vec{P}_{\perp} \end{pmatrix}$$

D.11

in the beam direction, we find the average kaon/lambda momenta in the LAB. For a K_S^0 in 100 GeV/c pp interactions

$$P = -\eta E^* + \gamma P^*_{\parallel} = (p_B/\sqrt{s}) \, m_{K_S^0}$$

$$\sim 3.5 \text{ GeV/c}$$

D.12

and at 400 GeV/c, p $\sim$ 7.0 GeV/c. In this case, the center-of-mass is the kaon rest frame and $\eta_{K_S^0}$ to go to the kaon rest frame is just $p_B/\sqrt{s}$ or 7.0 (14.0) at 100 (400) GeV/c.

Assuming that half the Λ's are at each maximum in x_F, and expecting to see decay only those in the backwards CM hemisphere, η_Λ to transfer to the lambda rest frame is 1.8 (3.8) at 100 (400) GeV/c.

Knowing $\eta_{K_S^0}$, the probability that a K_S^0 will decay visibly within ℓ cm of the vertex is

$$P_{K_S^0}(\ell) = BR_v \cdot \left[1 - \exp(-\ell/c\tau\eta_{K_S^0}) \right]$$

D.13

BR_V being the visible branching ratio, e.g. $K_S^o \rightarrow \pi^+ \pi^-$.

For $\ell < c \tau \eta_{K_S^o}$, we expand the exponential, multiply by the

average K_S^o multiply and obtain the probability to see any K_S^o

decay in the 100 and 400 GeV/c data.

$$P_{K_S^o}(\ell) = .007\ell \; (.004\ell) \qquad \qquad \text{D.14}$$

For half the Λ's (the backward hemisphere) expected to decay we get

$$P_\Lambda(\ell) = .004\ell \; (.002\ell) \qquad \qquad \text{D.15}$$

The probability of observing any photon convert is a function

of the conversion length for total pair production process, e.g.

$\gamma \rightarrow e^+ e^-$, and the γ multiplicity. The conversion length is

$$\lambda_c = A/\sigma_{PR} \, N_o \, \rho \qquad \qquad \text{D.16}$$

where A is the atomic number of the medium, ρ the density in

g/cm^3, N_o Avogadro's number and σ_{PR}, the total cross section for

pair production. The cross section is a function of the photon

momentum[6]. For an average photon momentum from .5 to 6 GeV/c[7] the

cross section varies only by 16%. We then use a σ_{PR} of 18 mb,

corresponding to a photon momentum of 1 GeV/c and a conversion

length of 1350 cm. In analogy to Equation D.13

$$P_\gamma(\ell) = 1 - \exp(-\ell/\lambda_c) \qquad \qquad \text{D.17}$$

is the probability of seeing a photon convert within ℓ cm of the vertex. Expanding the exponential and multiplying by the average photon multiplicity, the probability for any γ to convert in the 100 (400) GeV/c data is

$$P_\gamma(\ell) = .004\ell \ (.006\ell) \qquad\qquad \text{D.18}$$

The total neutral decay (plus conversion) probability can be made a function of primary event multiplicity. The normalized multiplicity functions from Eqs. D.9 and D.10 are then combined with the decay probabilities to produce the probability of seeing a vee in an N prong event. At 100 GeV/c

$$P_N(\ell) = (.35N + .5) \ P_\gamma(\ell) \ /2.6 + (.01N + .14) \ P_{K^0_s}/.20$$

$$+ \ P_\Lambda = (.89N + 9.67) \cdot 10^{-3} \ \ell \qquad\qquad \text{D.19}$$

and

$$P_N(\ell) = (.69N + 5.08) \cdot 10^{-3} \ \ell \qquad\qquad \text{D.20}$$

at 400 GeV/c.

Plotting the number of vees seen as a function of distance from the primary vertex in Fig. D.1, there is a loss seen near the vertex. The number missing in the depletion region, n_M, is known and an equivalent distance L can be defined in which all vees can
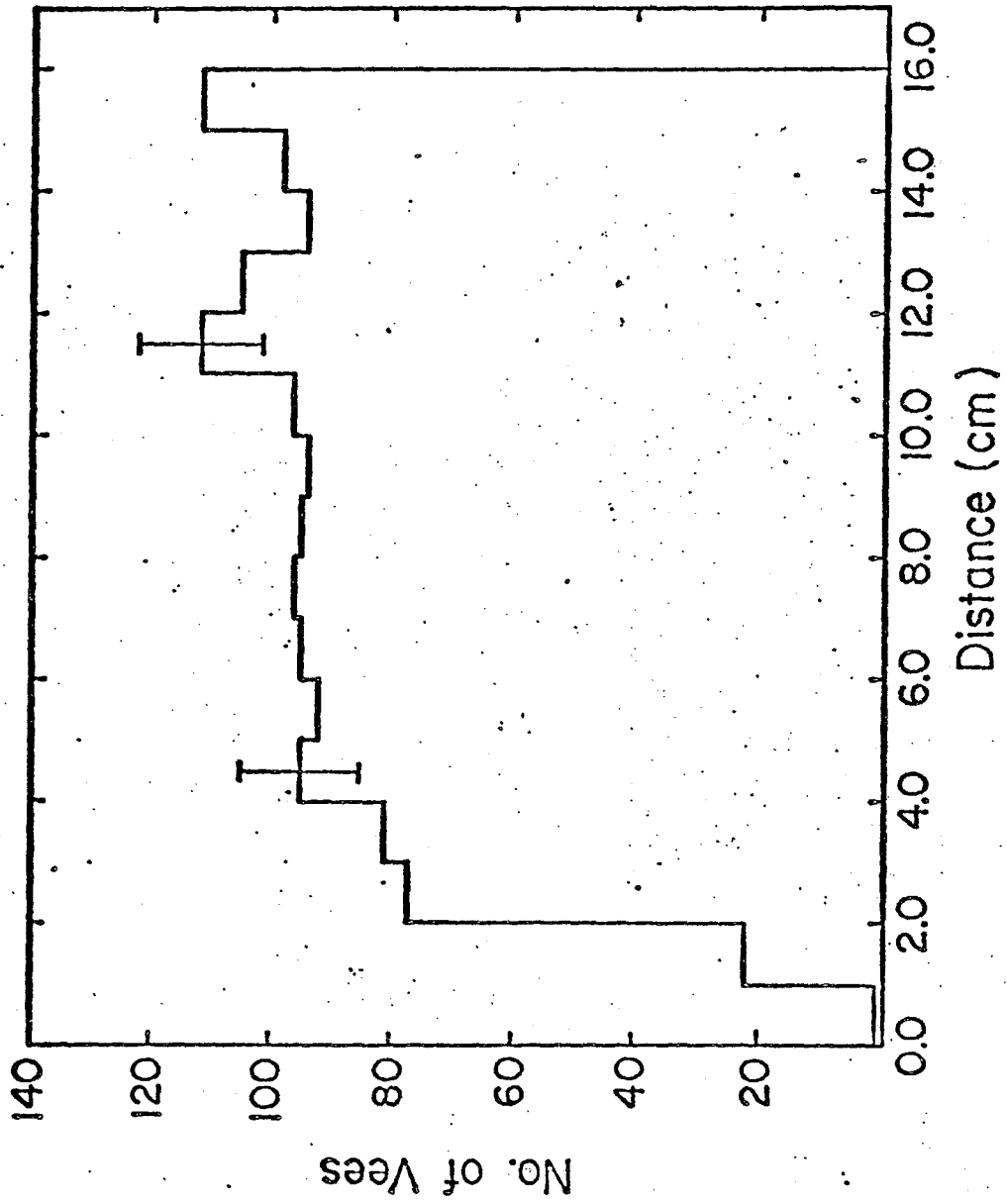
Fig. D.1

be considered lost. The number of vees lost or not seen is

$$Q_N(L) = (AN + B) \quad 10^{-3}LK = n_M \qquad D.21$$

where slope A and intercept B can be gotten from Eq. D.19 or D.20, and K is a constant. Letting $N = <N>$ we solve for LK, which was found to be between .5 and 1.0 for all collaborating institutions. The correction to the mean was on the order of .02 using a formula similar to Eq. D.8.

$$\Delta n_N = n_N^{TR} - n_N^{OB} \sim n_N^{OB} Q_N(L) - n_{N-2}^{OB} Q_{N-2}(L) \qquad D.22$$

D.5 Secondary Corrections

It is entirely possible for a scanner to miss an interaction or to miss a secondary track if it occurs close to the vertex in the forward spray of particles. The correction to the multiplicity distribution depends on both the primary and secondary vertex multiplicities. First the expected number of secondary interactions as a function of distance ℓ from the primary vertex is calculated and compared to the observed distribution. This yields the number of secondaries lost as a function of ℓ. Then the correction to each multiplicity is made as to reflect the multiplicity distribution of the secondary events.

An interaction length is defined as in Equation D.17 with $\sigma_T(\pi p)$, the total πp cross section, substituted for σ_{PR}. The πp cross section is momentum dependent, but above 2 GeV/c, 30 mb is

a good approximation for both negative and positive pions. Slower pions tend to have enough curvature to be visible before they interact. The probability of a single track not interacting between 0.0 and ℓ is

$$Q(\ell) = \exp(-\ell/\lambda) \qquad\qquad \text{D.23}$$

where $\lambda \sim 400$ cm. For an N prong event

$$Q_N(\ell) = (\exp(-\ell/\lambda))^N \qquad\qquad \text{D.24}$$

is the probability of no interaction, and per unit length becomes

$$dQ_N/d\ell = -N \ (\exp(-N\ell/\lambda))/\lambda \qquad\qquad \text{D.25}$$

Given the primary multiplicity distribution n_N, the number of tracks not interacting is Eq. D.26

$$dN/d\ell = \sum_N n_N dQ_N/d\ell \qquad\qquad \text{D.26}$$

and may be compared to the data in Table D.2 where non-interacting secondary tracks for each primary multiplicity are recorded as a function of ℓ in centimeters. (The data are from one Stony Brook roll where all secondaries, the associated primary multiplicity and ℓ were recorded.) We find a loss of observed secondaries for primary events with a multiplicity greater than 10. The equivalent length for losing all secondaries is 0.3 to 1.0 cm, dependent on

TABLE D.2

CHARGED SECONDARY INTERACTIONS

PRONGS	n_N	0	5	10	15	20
3	22	66	64	61	59	57
4	84	336	320	304	289	275
5	38	190	178	168	158	148
6	94	564	523	485	450	418
7	37	259	237	217	199	183
8	99	792	716	648	587	531
9	37	333	298	266	238	212
10	95	950	838	740	653	576
11	19	209	182	158	138	121
12	81	972	836	720	620	533
13	18	234	198	169	144	122
14	47	658	552	464	389	327
15	12	180	149	124	103	85
16	30	480	393	322	263	216
17	9	153	124	100	81	65
18	12	216	172	138	110	88
19	3	57	45	35	28	22
20	11	220	171	133	104	81
21	3	63	48	37	29	22
22	10	220	167	127	96	73
23	—	—	—	—	—	—
24	5	120	88	66	49	36
25	—	—	—	—	—	—
26	4	104	75	54	39	28
27	—	—	—	—	—	—
28	1	28	20	14	10	7

Distances are in cm on the scan table.

institution, and α, the fraction of primary events with missed secondaries is between 1.0 and 2.5 percent.

If the secondary interactions are randomly missed for primary multiplicities greater than 10, i.e. are independent of primary multiplicity, and that missed fraction is α, the observed number of N-prong events becomes

$$n_N^{OB} = n_N^{TR} (1-\alpha) + n_{N-1}^{TR} \alpha P_2$$

$$+ n_{N-2}^{TR} \alpha P_3 + \ldots + n_1^{TR} \alpha P_{N-1}$$

D.27

where P_N is the secondary multiplicity distribution normalized to unity. (Table D.3)

Approximating $n_N^{OB} \sim n_N^{TR}$ we derive the correction for unobserved secondaries.

$$\Delta n_N = n_N^{TR} - n_N^{OB} \sim (n_N^{OB} - n_{N-1}^{OB} P_2$$

$$- n_{N-2}^{OB} P_3 - \ldots \ldots \ldots)$$

D.28

TABLE D.3

SECONDARY INTERACTION MULTIPLICITIES

SECONDARY N	EVENTS	P(N)
2	377	0.495 ± 0.018
3	76	0.100 ± 0.011
4	144	0.189 ± 0.014
5	33	0.043 ± 0.007
6	51	0.067 ± 0.009
7	17	0.022 ± 0.005
8	24	0.032 ± 0.006
9	10	0.013 ± 0.004
10	14	0.018 ± 0.005
11	3	0.004 ± 0.002
12	6	0.008 ± 0.003
>12	6	0.008 ± 0.003

REFERENCES

1) Y. Akimov et al., Phys. Rev. Lett. 35, 763 (1975);

   Y. Akimov et al., Phys. Rev. Lett. 35, 766 (1975).

2) J. Whitmore, Phys. Reports 10C, 273 (1974).

3) C. Bromberg et al., Phys. Rev. Lett. 31, 1563 (1973).

4) J. Erwin et al., Phys. Rev. Lett., 32, 254 (1974).

5) H. Kichimi et al., KEK-PREPRINT-77-44 (to be published

   Phys. Lett. B, 1978).

6) T. M. Knasel, DESY Reports 70/2 and 70/3 (1970).

7) The average measured photon momentum, in an exposure of the

   hydrogen-filled 15' Fermilab bubble chamber to 300 GeV/c

   incident protons (E-343), was found to be 6 GeV/c.

   T. Kafka et al., private communication (letter submitted to

   Phys. Rev. Lett., 1978).

APPENDIX E

Measurement Errors

In dealing with a variety of data sets produced at different institutions, systematic biases must be understood. Distributions of interest may change and more importantly, error assignments may change radically, affecting the probability distribution from least squares fits made by programs like SQUAW.

E.1 Bubble Chamber Measurements

If any biases exist in the data, the most probable source is the bubble chamber measurement, due to the variety of measuring machines and TVGP programs used. The only significant deviations from the norm were found in the Stony Brook error assignments. The FRMS setting error for the Stony Brook measuring machines was approximately twice that of the other institutions, resulting in larger error assignments.

In Figures E.1 through E.3 we show the errors from the 400 GeV/c inclusive data for the variables ϕ, λ and p for non-stopping tracks. Only tracks with a measured length greater than 10 cm are used. The error in ϕ, the angle in the film plane, is a function of track length and curvature. Hence it has a minimum in the forward direction, the direction of the longest and fastest tracks, and is symmetric about $\pi/2$ radians. The error in the dip is a strong function of λ itself, as the projections

Fig. E.I
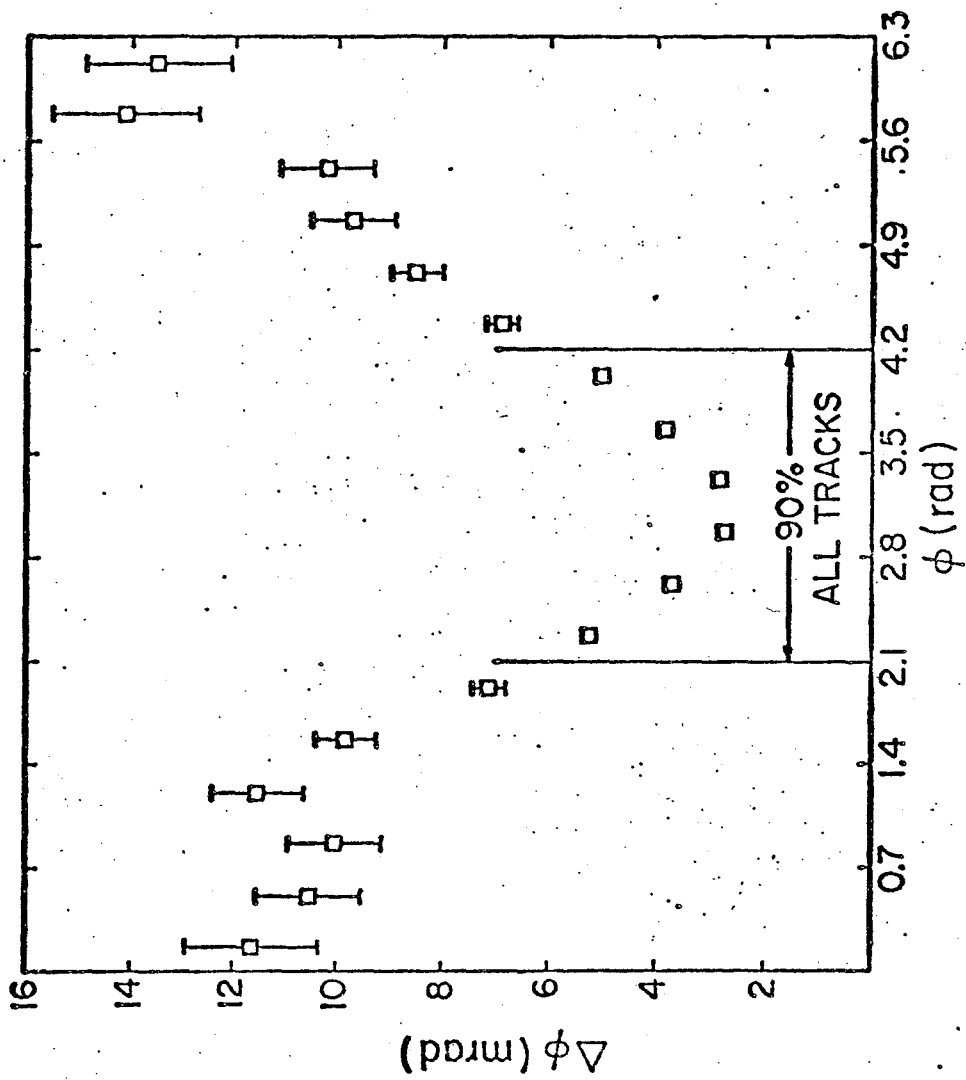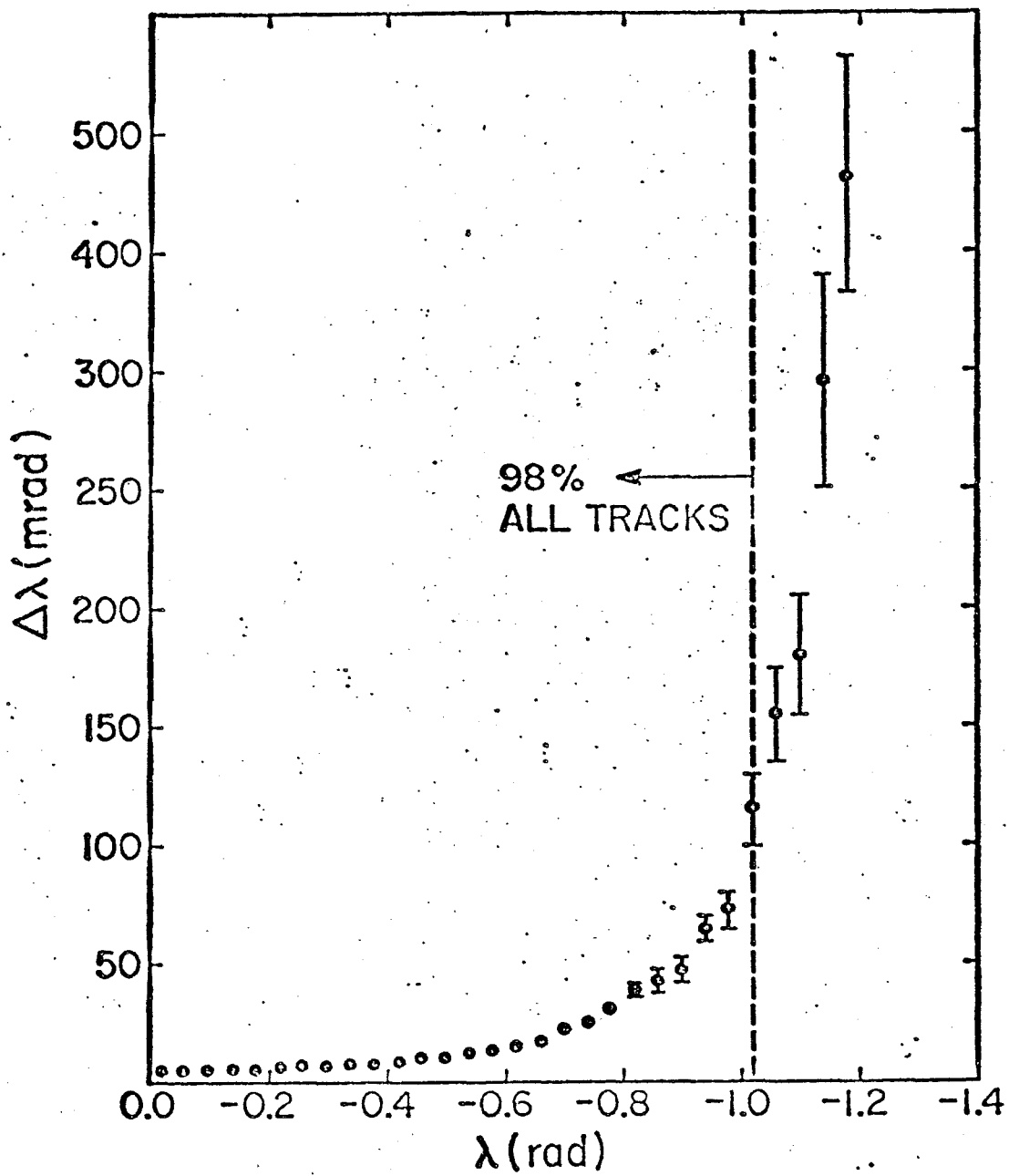
Fig. E.2
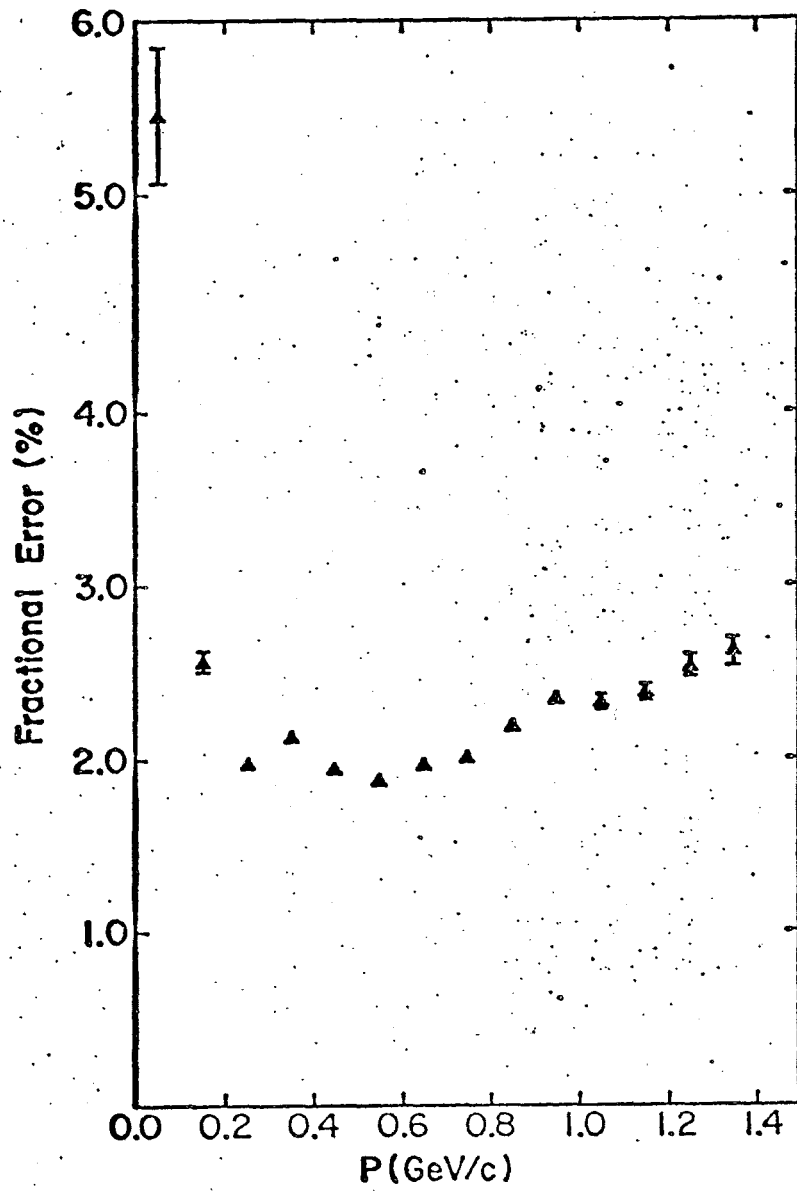
Fig. E.3

of steeply dipping tracks become increasingly more difficult to measure with increasing λ. A comparison of $\Delta\phi$ and $\Delta\lambda$ at their minima shows the azimuthal resolution to be twice as good. The last figure shows that the percentage error in momentum is high for very small momenta (large curvature) and after reaching a minimum between 500 and 600 MeV/c, begins to rise slowly. The correlations in errors between ϕ, λ and p have been neglected for simplicity, but may become large in extreme cases, e.g. steeply dipping tracks.

In Figures E.4 through E.6 we show the same distributions for each collaborating institution. The Michigan values are from 100 GeV/c data. The angle errors of the Stony Brook measurements are consistent with those of other institutions but the fractional momentum error is noticeably higher, making the Stony Brook momentum distributions suspect. However, the momenta themselves are distributed similarly for all institutions. See Fig. E.7 for positive pion distribution for slow tracks.

The same is true for negative pion and proton momenta, so we may conclude that if any bias is present, it can only affect the exclusive sample of events where SQUAW performs kinematic fits using the assigned error values. But the SQUAW results don't have a disproportionate amount of Stony Brook events satisfying the four-constraint fit to the neutron dissociation hypothesis of $hn \rightarrow hp\pi^-$. This is not surprising since fast
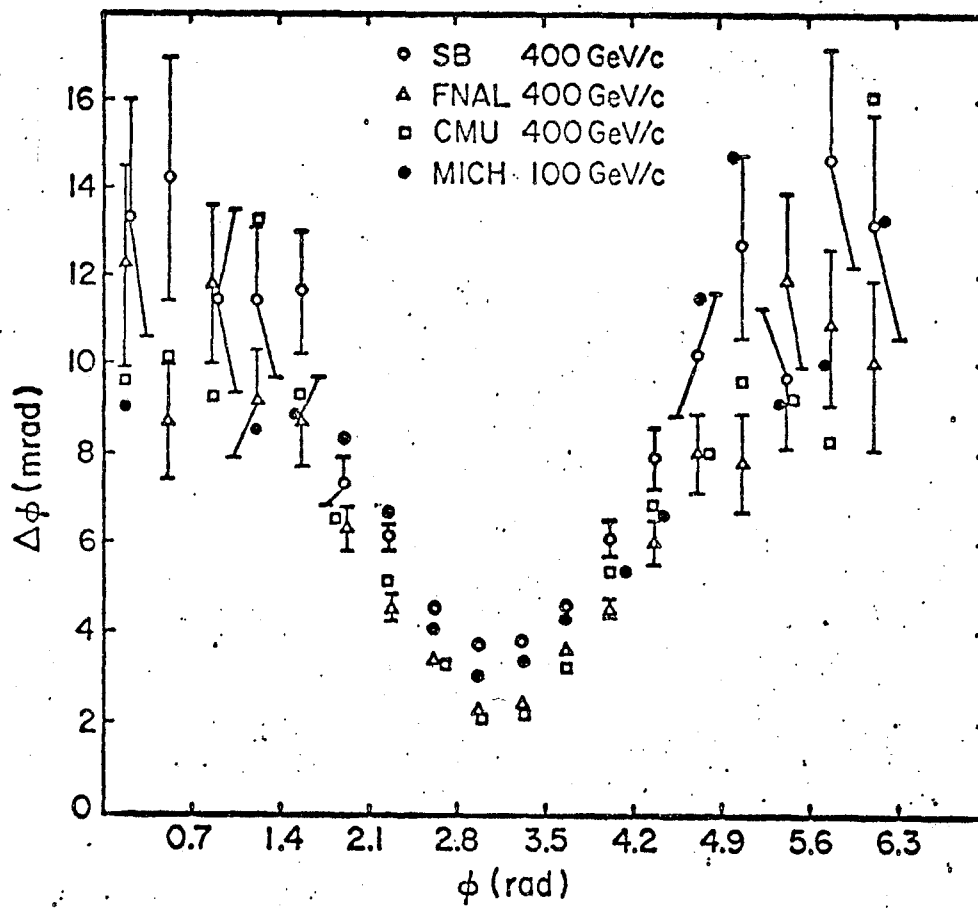
Fig. E.4
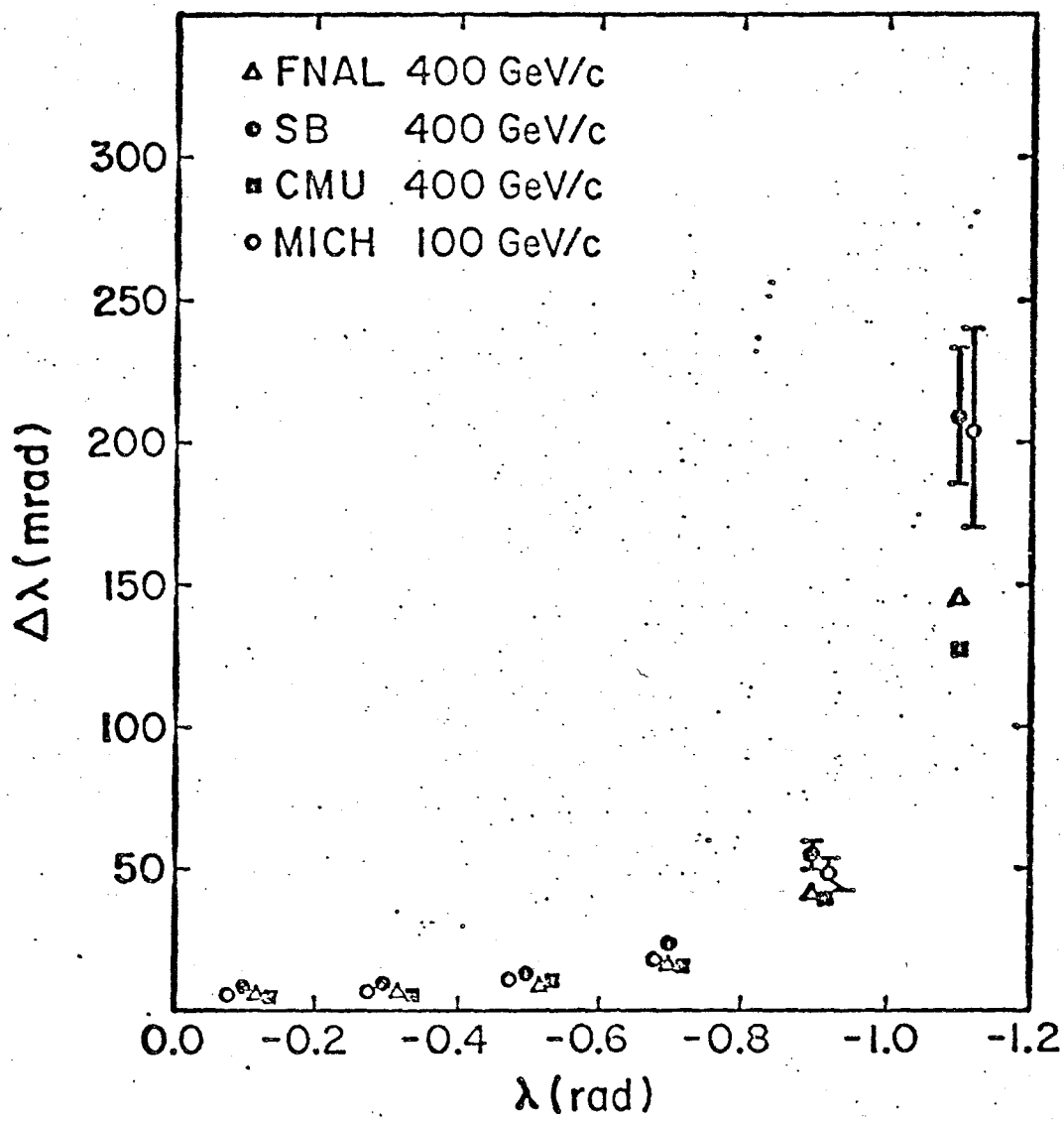
Fig. E.5
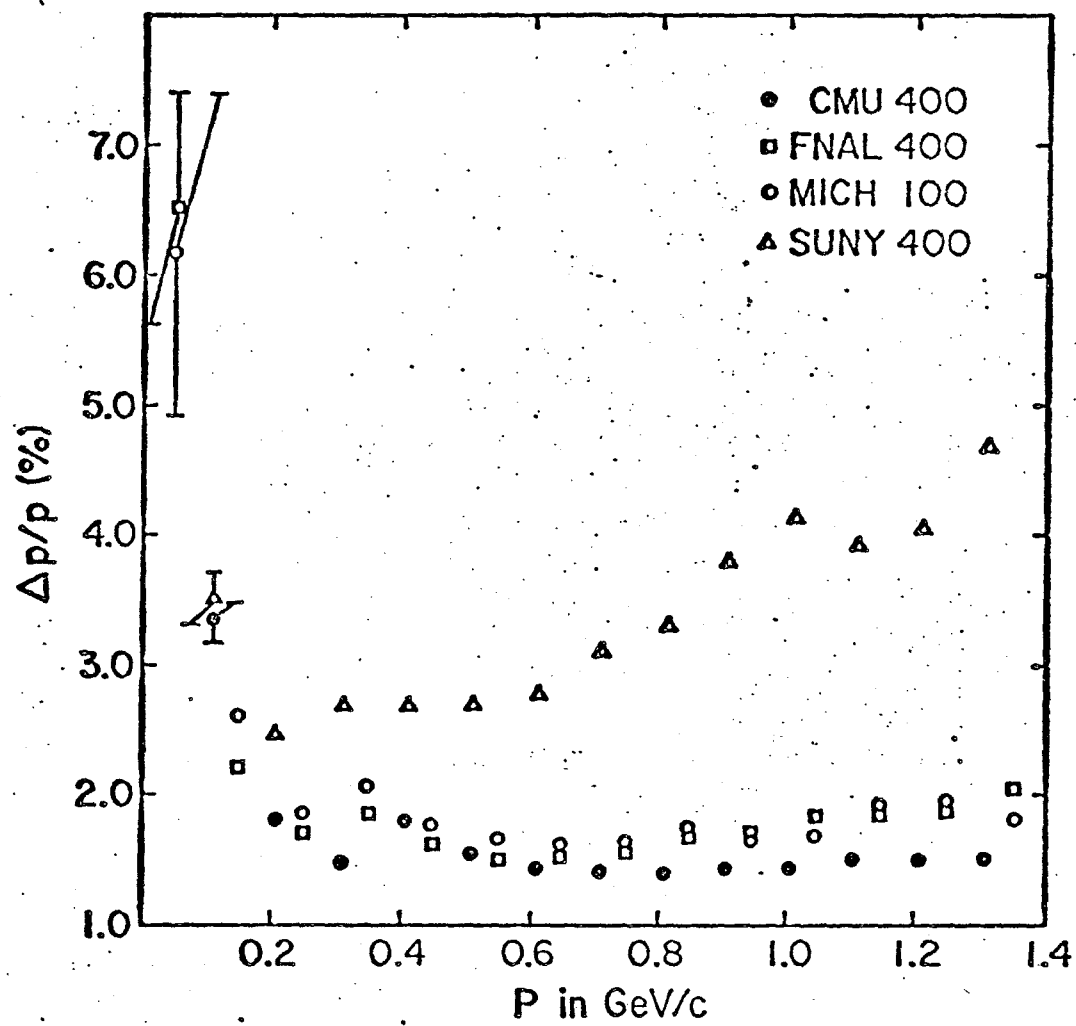
Fig. E.6
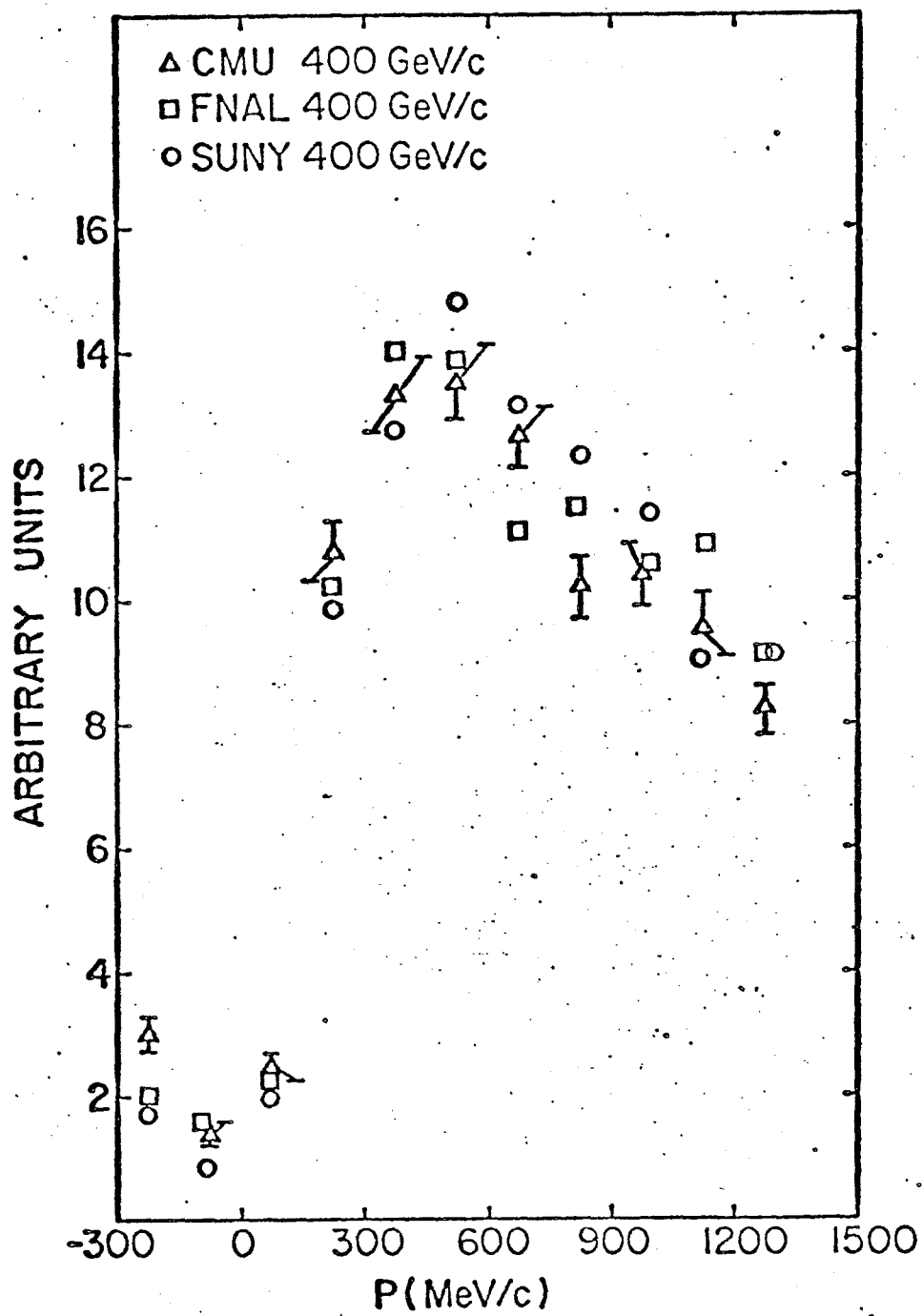
Fig. E.7

tracks having been TRACK ORGANIZED have errors mainly determined by the PWC measurements which are independent of institution. The absolute value of the combined momentum errors, as high as 5 GeV/c, make the differences in the momentum errors on slow tracks, which are not TRACK ORGANIZED, insignificant.

E.2 Ionization Errors

Particle misidentification in ionization mass assignments has two possible sources. Short stopping tracks may be deuterons from coherent events and ionized pions may be charged kaons. Because in our sample of interest we require a spectator proton and a slow proton to identify a neutron target event, the deuteron events, normally with only one possible proton (dark) track, are not a source of contamination. Furthermore, all calculations done with spectator proton distributions use only those spectators that have a negative $\cos\theta_s$. All deuterons will be forward with respect to the beam.

Charged kaon contamination may be estimated using the K_s^o distribution from Ref. 2. Crudely estimating the average charged K multiplicities and x_F distributions to be similar to those for K_s^o, in our measured region of phase space, p 1.4<GeV/c or x_F<-.10, Figure 89 in Ref. 2 shows that we measure 60% of the backward hemisphere (CM) kaons. As in Appendix D we use average K_s^o multiplicities of .14 and .24 at 100 and 400 GeV/c respectively, half of these for the backwards hemisphere. The average

multiplicities of measured pions are 1.3 and 1.6 respectively. This leads to a kaon contamination of 3 and 9%. In 205 GeV/c pp data[2] using Monte Carlo techniques, the $\bar{K}/\bar{p}$ contamination to the total π^- data sample, where all tracks in an event were measured, was found to be 10%. This is an upper limit for our data because roughly 40% of the kaons are produced between x_F of 0.0 and -0.1, which is above our 1.4 GeV/c lab momentum cutoff. Our crude calculation is then consistent with a more exact method, and the small kaon contamination to the charged pion sample will be ignored. As a final check, CERN results[3] at s=30 GeV^2 and Fermilab counter experiment results[4] at 100 and 400 GeV/c in pp collisions show K^+/π^+ and K^-/π^- ratios of 10 percent or less for transverse momenta less than 400 MeV/c in our phase space region.

E.3 Proportional Wire Chamber Measurements

Errors in ϕ, λ and p for fast tracks and beam tracks passing through the wire chambers, differ considerably from bubble chamber values. Where the bubble chamber measurement of momentum becomes totally unreliable for tracks with momenta greater than 20 GeV/c, yielding fractional errors greater than 20%, the PHS errors will typically be no larger than 20% even for the fastest beam-like tracks. (The merging of BC and PWC data by TRACK ORGANIZER improves this result considerably).

Angular resolution is much better for PWC tracks, owing to the "lever-arm" effect of having the wire chambers several

meters away from an event vertex. Where typical bubble chamber errors are on the order of a few milliradians, PWC errors can be quoted in tenths and hundreths of milliradians. Unlike in the bubble chamber, where the resolution for the azimuth is better than that for the dip, the PWC dip is the better determined angle.

Errors at the vertex are calculated after the PWC tracks have been swum to the BC vertex. To the degree that the chamber magnetic field is constant in the bubble chamber, the momentum used in swimming the track has no effect on the angle in the direction of the field. The error in the dip then reflects just the error in the wire positions. In contrast, the film-plane azimuth depends strongly on the PWC track momentum which introduces an added uncertainty to the determination of ϕ. Typical errors for ϕ and λ are .25 and .05 milliradians. The smallness of these quantities gives rise to a dominance of PWC track angles over the bubble chamber measured angles when TRACK ORGANIZING.

E.4 TRACK ORGANIZER errors

The errors calculated by TRKORG are part of the input to SQUAW and have a tremendous influence on the kinematic fit attempts. The validity of these error assignments will be demonstrated in this section.

In Figures E.8a and 8b we present scatter plots of the error in λ versus the error in ϕ for positively and negatively

$\Delta\lambda$ (mrad)

+ CHARGED TRACKS

$\Delta\phi$ (mrad)

Fig. E.8a

$\Delta\lambda$ (mrad)

```
           11          11 1      1 1       1
              121          1    1 2  11    I
    1   1        21    11 1 1        2 11   I
   1  111      2  221       111        2  24  I
     1    1312  12  121       111  2  24   I
   1  1 11  2212  213224   234    1 1  131  I
     13   11  21646212143 63222221  2   I
   51  221  452721 25612  31  2      I
      115434  44741321  1  1        I
      53757799751211               I
      59449912121                  11      I
      38993 12                             I
      2981  21       11     11        11   I
           1                              I
           1  211 1   1    1111 131    1  I
                          2211122  2  1 I
    1 12  111211213223242152122 1 5111  I
    11431 4242233 37434222 1 13351 1  I
    3543254355115632425442123111 22  I
    5956494845151 41  1  2            I
    399433 1                          I
                                      I
                                      I
                                      I
                      1               I
                                      I
       — CHARGED                      I
          TRACKS                      I
                                      I
                                      I
```

PROJ
ON X
AXIS

```
              245334424333322221211211 11111
0000000000000000000999472075141618269966936329440857
```

LOWR
EDGE
VALU

```
00000000000000000000000000000000000000000000000000
000000000011111111111222222222233333333334444444444
0123456789012345678901234567890123456789012345678 9
```

PROJ
ON Y
AXIS

$\Delta\phi$ (mrad)

Fig. E.8b

charged tracks that have been successfully TRKORG'ed. The system should show no bias for or against a charge type, and the two figures appear qualitively the same. The abundance of positively charged particles is expected, as the beam particles are positively charged and the wire chamber "sees" all of the beam fragmentation region. The errors are seen to be on the order of PWC track error values, which dominate.

An interesting feature is the band effect in the dip values. The lower bands correspond to tracks that have passed through all four downstream wire chambers. The upper bands of poorer resolution are from the slower three-chamber tracks. The band effect would presumably be seen in the azimuthal errors, if the wire chambers constrained in the x-y plane as well as in the z-direction. But this is not the case, as mentioned in Section E.3.

The fractional error in momentum as a function of momentum exhibit a linear dependence. Figures E.9a and 9b show the fractional error for four-chamber tracks. Beam-like positive tracks with momenta on the order of 100 GeV/c have errors between 2 and 9 percent, the average value being 5 or 6%. There are almost no beam-like negative particles, the majority of the fast negative particles resulting from beam fragmentation.

E.5   System Alignment and Sensitivity

a.   Alignment

ΔP/P

4-CHAMBER
+TRACKS

PROJ
ON X
AXIS

PROJ
ON Y
AXIS

LOWR
EDGE
VALU

p (GeV/c)

Fig. E.9a

ΔP/P

4-CHAMBER
-TRACKS

p (GeV/c)

Fig. E.9b

Extensive studies were made to test the accuracy of the TVGP-PWGP-TRKORG results and the sensitivity of these results to misalignments of the bubble chamber coordinate system to the PHS. The momentum of beam tracks was previously determined to be 97.7±.4 GeV/c by the program SURVEY, which requires only wire chamber data and the magnetic field map, and we use beam tracks to calibrate the system.

PWC beam tracks are well collimated, have known momenta and have good angular resolution from the long upstream lever-arm. In comparison to bubble chamber angles, the PWC beam tracks when swum to the vertex may be considered to have no error. Defining

$$\Delta\phi \equiv \phi_{BC} - \phi_{PWC} \qquad \text{E.1a}$$

$$\Delta\lambda \equiv \lambda_{BC} - \lambda_{PWC} \qquad \text{E.1b}$$

$$\Delta y \equiv y_{BC} - y_{PWC} \qquad \text{E.1c}$$

$$\Delta z \equiv z_{BC} - z_{PWC} \qquad \text{E.1d}$$

where the PWC values have already been rotated and translated into the bubble chamber system, we take weighted averages of the difference on each roll of film using the inverse square of the bubble chamber error as the weight. See Section A.12. The error in the mean differences is the weighted r.m.s. divided by the square root of the unweighted number of beams used. A $<\Delta\phi>$ or $<\Delta\lambda>$ significantly different from 0.0 means there is a misalignment of the two measuring systems.

Table E.1 presents the mean differences and errors for vertex angles and positions for beam tracks in the exclusive event sample. Two rolls from each institution are presented. Only tracks with a measured bubble chamber length greater than 35 cm are used. These longer tracks have a better bubble chamber resolution and will not mask any significant deviations. All dip differences are seen to deviate from 0.0, particularly the Carnegie-Mellon data. Azimuth differences tend to be smaller, within .25 mr and 3 standard deviations of 0.0, the Carnegie-Mellon data again being the exception. Except for Michigan vertices, all differences are less than 1 mm.

b. Sensitivity

What do the numbers in Table E.1 mean in terms of momentum determination and resolution? To answer this question, we took a relatively well-aligned roll (1232) and measured 120 non-interacting beam tracks. A fake vertex was generated on the beam track and the vertex and a fiducial mark used to define a 2-point track. The data was then processed as a 2-prong event through the TVGP-PWGP-TRKORG processing chain, the downstream part of the beam track treated like any other outgoing track that reaches the downstream wire chambers.

Vertices were generated at several points along each beam track, corresponding to different bubble chamber track lengths for the downstream part. A summary of the TRKORG

TABLE E.1

PWC-BC MISALIGNMENTS

ROLL	INST	N_B	$\Delta\phi$ (mr)	$\Delta\lambda$ (mr)	Δy (mm)	Δz (mm)
1226	SUNY	95	-0.14 ± 0.09	-1.97 ± 0.16	0.12 ± 0.06	-0.15 ± 0.19
1229	CMU	168	1.13 ± 0.05	-8.01 ± 0.17	0.19 ± 0.04	-0.93 ± 0.11
1230	MICH	42	0.07 ± 0.16	0.04 ± 0.47	0.44 ± 0.07	-2.09 ± 0.20
1231	SUNY	149	0.11 ± 0.06	-1.31 ± 0.23	0.13 ± 0.03	-0.24 ± 0.10
1232	FNAL	139	-0.11 ± 0.05	-1.51 ± 0.11	0.10 ± 0.04	0.22 ± 0.08
1233	CMU	121	1.27 ± 0.07	-7.49 ± 0.28	0.21 ± 0.04	1.07 ± 0.14
1238	MICH	49	0.22 ± 0.11	1.10 ± 0.56	0.53 ± 0.10	-1.81 ± 0.27
1240	FNAL	95	-0.28 ± 0.07	-0.65 ± 0.21	-0.08 ± 0.08	-0.06 ± 0.19

results is presented in Table E.2, where the OUT subscript refers
to the downstream track segment, and IN to the incoming upstream
segment. The angular differences should be 0.0 if the two ends of
the PHS are themselves properly aligned. The azimuth values are
consistent with 0.0 and the dip values, while not 0.0, are an
order of magnitude better than the values in Table E.1. The
slow increase or decrease in the differences as a function of track
length arises from the bubble chamber influence on the TRACK
ORGANIZER results and depends on the precise nature in which it is
out of alignment with the PHS.

The most interesting number is P_{OUT}, which is the beam
track momentum as determined by the entire processing system, and
is quite reasonable when compared with the SURVEY result of
97.7±.4 GeV/c. It appears only to have a slight dependence on
track length, so we may be confident that events in any particular
part of the bubble chamber don't have a momentum bias. The RMSP
or root mean square deviation of the momentum distribution, on the
other hand, increases markedly with a decrease in track length.
This width can be interpreted as the error in momentum when
TRACK ORGANIZING a beam-like track, which becomes larger for shorter
tracks, and is roughly equal to the actual momentum error quoted
by TRKORG. For vertices in the center of the chamber, yielding
on average track length of 37 cm, the quoted error is 6.4 GeV/c.
Both error values agree well with the 5 to 6% fractional error in

TABLE E.2

FAKE 2-PRONG RESULTS

L_{OUT} (cm)	Δy_{OUT-IN} (mm)	$\Delta\phi_{OUT-IN}$ (mr)	$\Delta\lambda_{OUT-IN}$ (mr)	P_{OUT} (GeV/c)	RMSP (GeV/c)
59	0.14±0.04	−0.0115±0.0199	0.1098±0.0280	99.44±0.23	2.52
48	0.12±0.04	−0.0130±0.0233	0.1040±0.0290	99.84±0.32	3.51
37	0.11±0.04	−0.0153±0.0342	0.0894±0.0291	100.19±0.56	6.13
26	0.11±0.04	−0.0490±0.0545	0.0404±0.0179	101.18±1.11	12.16

momentum quoted in Section E.4 for real secondary tracks, giving validity to the TRKORG error values.

The "fake" 2-prong events are also processed through a system where the wire chamber has been rotated or translated with respect to the bubble chamber. This is easily done by tampering with the rotation and translation constants calculated by FIDROT and used as input to PWGP. Fake secondary tracks of 48 cm are used in this test for the sake of better accuracy. In Figures E.10a and E.10b the change in momentum from the nominal TRKORG value of 99.8 GeV/c is shown for rotations in ϕ about the z-axis and for translations in the y-direction. Dip rotations about the y-axis and translations in the z-direction have no effect on the momentum.

We conclude from the values of $\Delta\phi$ in Table E.1 and the associated ΔP in Figure E.10a that all systematic errors from angular misalignment are at most equal to the quoted error values except in the CMU data. The fastest CMU tracks are found to be in the 110 to 120 GeV/c range as predicted by the CMU $\Delta\phi$ and are corrected before being fed to SQUAW. Momentum changes due to y-axis translations are negligible.
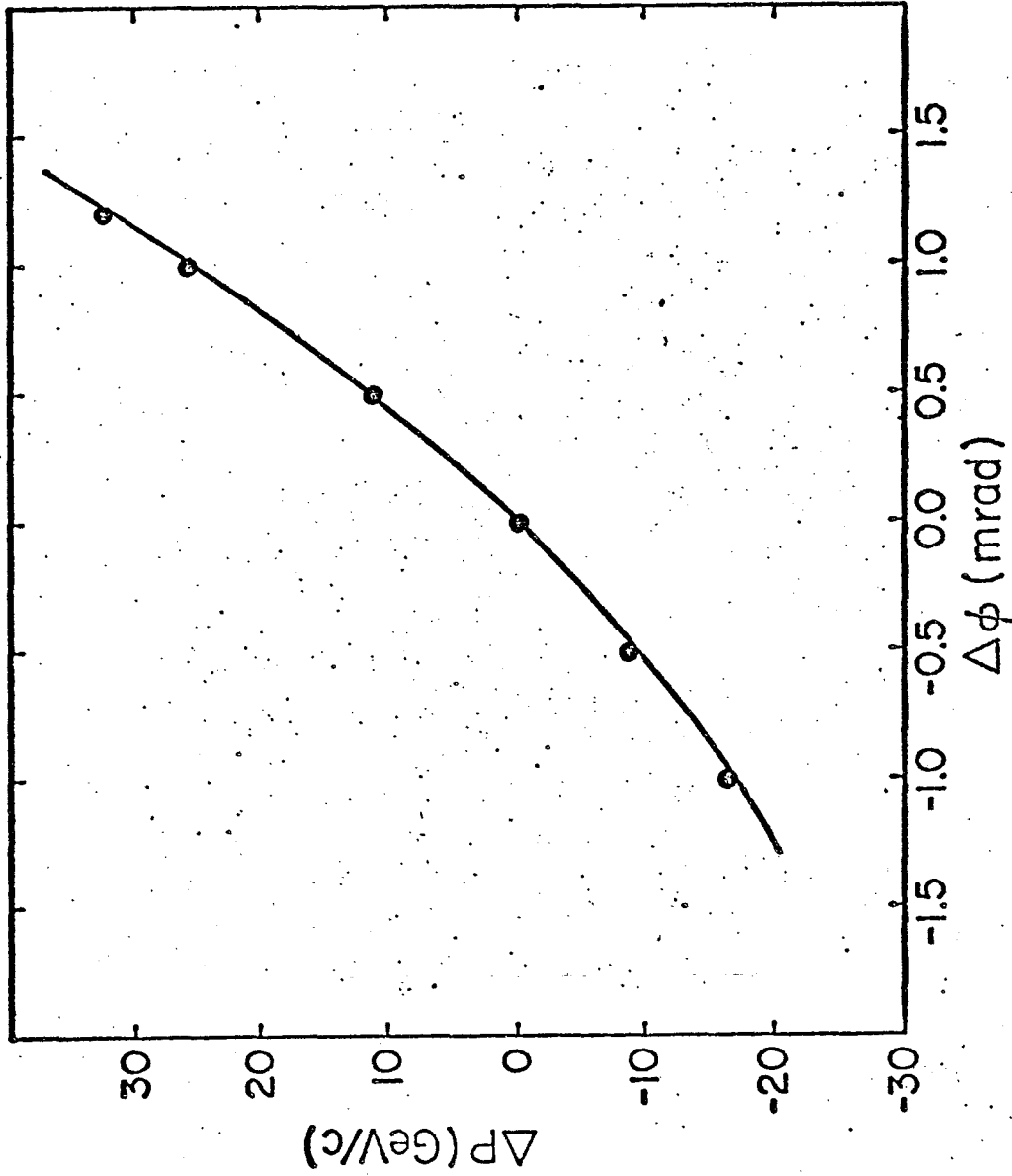
Fig. E 10.a
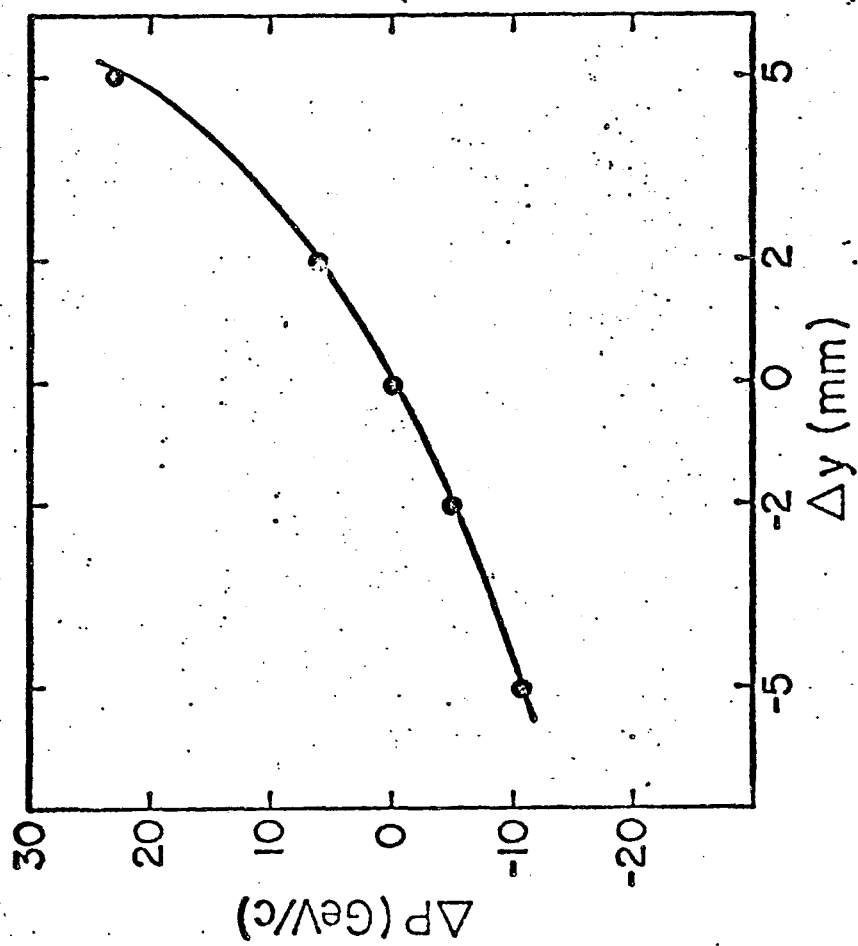
Fig. E.10b

REFERENCES

1)   J. Whitmore, Phys. Reports $\underline{10c}$, 273 (1974).

2)   T. Kafka, Thesis – "Multiparticle Production in pp Col-
     lisions at 205 GeV/c" (University Microfilms, Ann Arbor,
     1974).

3)   E. Albini et al., "Summary of Results of the Experiment on
     Charged Particle Production at Medium Angles Performed at
     the Cern ISR" (NP Internal Report 75-2, 1975).

4)   J. R. Johnson et al., Phys. Rev. $\underline{D17}$, 1292 (1978).

APPENDIX F

Mueller-Regge Analysis

F.1 The Generalized Optical Theorem

The simplest inclusive cross section is the total cross section for any two particle interaction, $a + b \to X$. The cross section for this process can be related to the imaginary part of the forward elastic scattering amplitude $a + b \to a + b$ as a result of the unitarity constraint on the scattering matrix.

Defining the scattering matrix as

$$S \equiv 1 + i\delta^4(\bar{q} - \bar{p})T \qquad\qquad \text{F.1}$$

where δ^4 is a four-dimensional Dirac delta function, $\bar{p}$ the total incoming momentum, $\bar{q}$ the total outgoing momentum, and T the transition matrix for going from an initial state $|ab\rangle$ to a final state $|X\rangle$. The unitarity constraint is $SS^\dagger = 1$ and when applied to Eq. F.1 yields

$$-i(T - T^\dagger) = TT^\dagger \delta^4(\bar{q} - \bar{p}) \qquad\qquad \text{F.2}$$

Letting the final state $|X\rangle$ form a complete basis such that

$$\sum_X |x\rangle\langle x| = 1 \qquad\qquad \text{F.3}$$

where the summation is over all possible final states, then

$$\langle ab|-i(T - T^\dagger)|ab\rangle = \delta^4(\bar{p}-\bar{q})\langle ab|T(\sum_X |x\rangle\langle x|)T^\dagger|ab\rangle \qquad \text{F.4}$$

which reduces to

$$2\text{Im}\langle ab|T|ab\rangle = \sum_X \delta^4(\bar{q} - \bar{p})|\langle ab|T|x\rangle|^2 \qquad\qquad \text{F.5}$$

is the elastic forward scattering amplitude $T_{ab}(s)$ and

depends only on the CM energy. If we can analytically continue

$T_{ab}(s)$ to the complex energy plane

$$2\mathrm{Im}T_{ab}(s) = T_{ab}(s+i\epsilon) - T_{ab}(s-i\epsilon) \equiv \mathrm{Disc}_s\, T_{ab}(s) \qquad\qquad \text{F.6}$$

$\mathrm{Disc}_s T_{ab}(s)$ indicating the discontinuity across the s-cut of the

amplitude. The right side of Eq. F.5 is $s\sigma_T^{ab}(s)$, the factor of s

coming from the implicit integration over Lorentz invariant phase

space, and the total cross section is then written as

$$\sigma_T^{ab}(s) = s^{-1}\mathrm{Disc}_s\, T_{ab}(s) \qquad\qquad \text{F.7}$$

This is the optical theorem, and is illustrated in Fig. F.19.

Mueller[1] generalized these results for inclusive processes.

For single particle inclusive reactions $a + b \to c + X$, which may

be written as $a + b + \bar{c} \to X$, we proceed as above, summing over all

final states with missing mass M^2 and showing the cross section to

be proportional to the three-body forward scattering amplitude.

See Fig. 1b. Note that the three body amplitude depends on three

variables out of s,t,u and M^2, and that the discontinuity in the

amplitude is taken across the M^2-cut. The analog to Eq. F.7 is then

$$E_c\frac{d^3\sigma^{ab}}{dp_c^3} = \frac{d^2\sigma^{ab}}{sdtd\text{M}^2} = s^{-1}\,\mathrm{Disc}_{M^2}T(s,t,M^2) \qquad\qquad \text{F.8}$$

More detailed discussions of these results can be found in Refs.

2 and 3.

F.2 Triple-Regge Analysis

According to Mueller, Regge theory may be applied to the

results of the generalized optical theorem, in our case to the
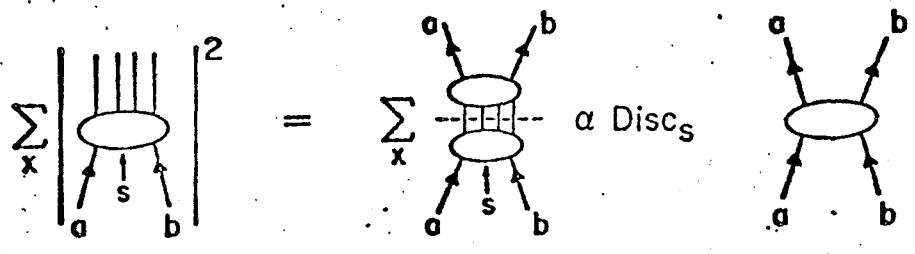
Fig. F.1a
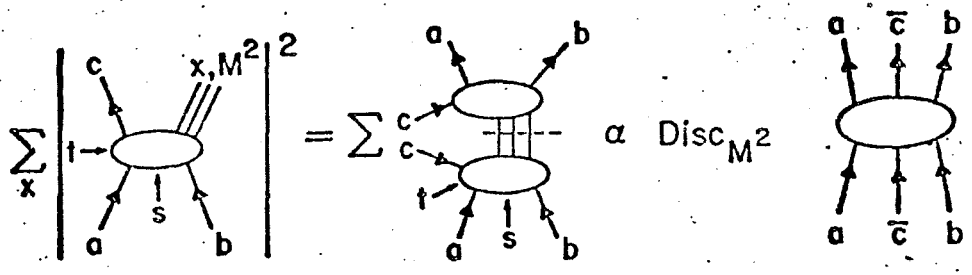
Fig. F.1b
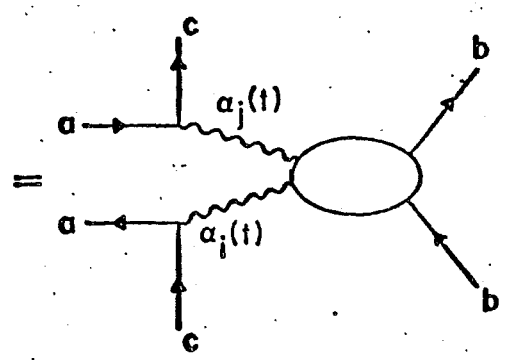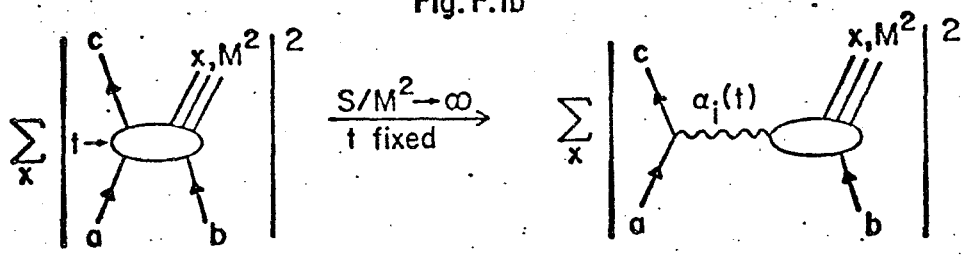
Fig. F.2a

single particle inclusive cross section in Eq. F.9 and Fig. 1.b. The amplitude will exhibit Regge behavior if one or more of the kinematic variables becomes large. Then there are Regge poles in the crossed channel and the asymptotic behavior of the amplitude is determined by the trajectories of the poles. The functional form of the amplitude may be derived from non-relativistic potential theory[4] or relativistically from group theoretical arguments[5].

Following Field and Fox[6], we let s/M^2 become large with $s \gg t$, and write the invariant cross section

$$\frac{s}{\pi} \frac{d^2\sigma}{dt\,dM^2} \xrightarrow{s/M^2 \to \infty} \frac{1}{16\pi s} \sum_{ij} \beta^i_{a\bar{c}}(t) \varepsilon_i(t) \left(\beta^j_{a\bar{c}}(t)\right)^* \cdot s^{\alpha_i(t)+\alpha_j(t)} \operatorname{Im} A_{ib \to jb}(\nu, t) \qquad \text{F.9}$$

where $\nu = M^2 - t - m_b^2$, $A(\nu, t)$ is the forward Reggeon particle scattering amplitude, and β^i_{ac} is the coupling of Regge pole i to particles a and c. $\varepsilon_i(t)$ is the Regge signature factor

$$\varepsilon_i(t) = \left[\tau_i + \exp(-i\pi\alpha_i(t))\right]/(-\sin\pi\alpha_i(t)) \qquad \text{F.10}$$

where $\alpha_i(t)$ and τ_i are the trajectory and signature of the pole. (For poles with even angular momentum, $\tau_i = +1$, and for odd angular momentum, $\tau_i = -1$). The limit is displayed graphically in Fig. F.2a.

By further requiring $M^2 \to \infty$, the asymptotic behavior of $A(\nu,t)$ may be reggeized as in Eq. F.11, governed by the poles $\alpha_k(0)$ which couple to $b\bar{b}$ and $\alpha_i\bar{\alpha}_j$. See Fig. F.2b.

$$\operatorname{Im} A_{ib \to jb} = \beta^k_{b\bar{b}}(0) \operatorname{Im}\varepsilon_k(0) g^k_{ij}(t) \cdot (M^2)^{\alpha_k(0)-\alpha_i(t)-\alpha_j(t)} \qquad \text{F.11}$$

where $g^k_{ij}(t)$ is the triple-Regge coupling. Combining Eq. F.9 and F.11, yields the triple-Regge formula, pictorially represented in
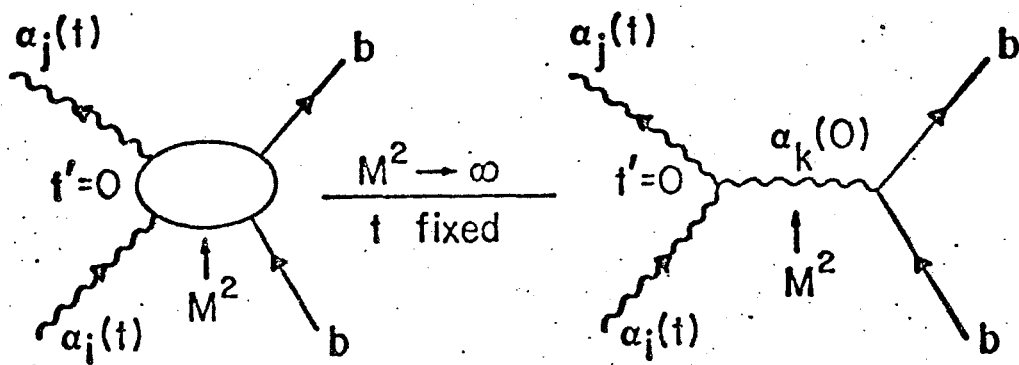
Fig. F.2b
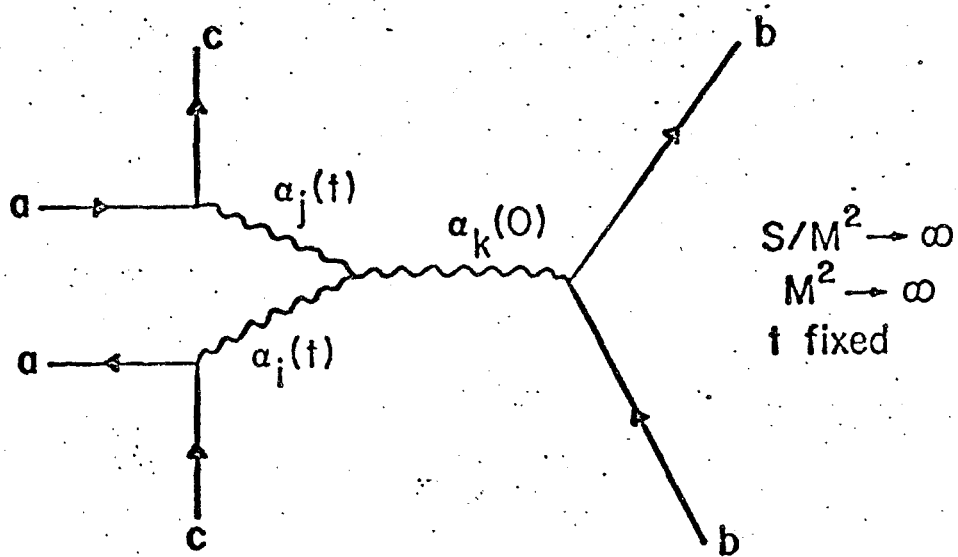
Fig. F.2c

Fig. F.2c.

$$sd\sigma/dtdM^2 = s^{-1} \sum_{ijk} G(t)(s/M^2)^{\alpha_i(t)+\alpha_j(t)} (M^2)^{\alpha_k(0)} \qquad \text{F.12}$$

$G_{ijk}(t)$ contains the four couplings and signature factors.

If $i{=}j$ in Fig. F.2b, the graph represents the total Reggeon-particle cross section mediated by Regge pole k and we write

$$\sigma^k_{ib}(M^2,t) = \beta^k_{bb}(t)\,\text{Im}\beta_k(0)g^k_{ii}(t)(M^2)^{\alpha_k(0)-1} \qquad \text{F.13a}$$

and

$$\sigma^{TOT}_{ib}(M^2,t) = \sum_k \sigma^k_{ib} \qquad \text{F.13b}$$

(Eq. F.13 is defined such that the optical theorem in Eq. F.6 is obeyed.)

Choosing i and j to be pion trajectories for a particular process, we expect dominant contributions from $\pi\pi P$ and $\pi\pi R$ couplings. Here P is a pomeron trajectory with zero quantum numbers and R a general Reggeon trajectory, such as the ρ/A_2 with isospin 1.

Eq. F.12 is then rewritten as

$$s\frac{d\sigma}{dt\,dM^2} = \frac{1}{16}\left|\beta^\pi_{a\bar{c}}(t)\right|^2 \left(1/\sin\pi\alpha_\pi(t)\right) \qquad \text{F.14}$$
$$\cdot\left[(s/M^2)^{2\alpha_\pi(t)-\alpha_P(0)}\sigma^P_T(\pi b) + (s/M^2)^{2\alpha_\pi(t)-1}(M^2)^{\alpha_R(0)}\sigma^R_{T_i}(\pi b)\right]$$

using Eq. F.13a. Letting

$$\alpha_P(t) = 1 + \gamma t \qquad \text{F.15a}$$

$$\alpha_\pi(t) = 0.0 + t \qquad \text{F.15b}$$

$$\alpha_R(t) = 0.5 + t \qquad \text{F.15c}$$

and using Eq. F.13b we arrive at

$$s\frac{d\sigma}{dt\,dM^2} = \frac{1}{16}\left|\beta^\pi_{a\bar{c}}(t)\right|^2\left(1/\sin^2\pi\alpha_\pi(t)\right)(s/M^2)^{2t-1}\sigma_T(\pi b) \qquad \text{F.16}$$

Near the pion mass-shell ($t \simeq m_\pi^2$), the sin function may be

expanded giving $(t-m_\pi^2)$ and we set

$$|\beta_{ac}^-(t)|^2 = g_{\pi ac}^2(t)\exp\left[a(t - m_\pi^2)\right]$$ F.17

where $g_{\pi ac}^2$ is the on mass-shell coupling, the exponential term a

correction for the pion trajectory being off mass-shell and the

factor $-t$ forces the cross section to zero at $t=0$. The final cross

section expression as given in Eq. F.18. is the Reggeized-One-Pion-

Exchange-Model.

$$sd\sigma/dtdM^2 = (g_{\pi ac}^2/16\pi^2)\left[-t/(t - m_\pi^2)^2\right]$$ F.18
$$\cdot(s/M^2)^{2t-1}\sigma_T(\pi b)\exp\left[a(t - m_\pi^2)\right]$$

REFERENCES

1) A. H. Mueller, Phys. Rev. $\underline{D2}$, 2963 (1970).

2) C. Quigg, "A. I. P. Conference Proceedings of Particles and Fields - 1971," Eds. A. C. Melissinos, et al. (American Inst. of Phys., New York, 1971).

3) J. Sens, "Particle Interactions at Very High Energies - Part A," Eds. D. Speiser et al. (Plenum Press, New York, 1974); D. Horn, ibid.

4) R. Omnes and M. Froissart, "Mandelstram Theory and Regge Poles" (W. A. Benjamin, New York, 1963); S. Frautschi, "Regge Poles and S-Matrix Theory" (W. A. Benjamin, New York, 1963).

5) H. D. Abarbanel, Phys. Rev. $\underline{D3}$, 2227 (1971).

6) R. D. Field and G. C. Fox, N. P. $\underline{B80}$, 367 (1974).

APPENDIX G

Deuterium Targets

Even in a simple deuteron nucleus, care must be taken in extracting cross sections for the nucleon of interest, in our case, the neutron. A formalism developed by Glauber[1,2] can be used to deal with the problem of screening, the eclipsing of one nucleon by the other, which decreases the expected deuteron cross section. Once the individual nucleon cross sections can be related to the nuclear cross section, it is still necessary to identify which nucleon, if not both, was involved in the reaction. Knowledge of the deuteron wave-function and the application of the impulse approximation model of Chew[3] will supply the handle needed to identify target types. Fridman[4] outlines the above and more in a systematic and detailed manner. The reader should note that deuteron target interactions fall into three classes:

1. Coherent deuteron interactions where the deuteron appears in the final-state;

2. Spectator interactions where only one nucleon interacts with the beam particle and the deuteron breaks up;

3. Rescatter interactions where both nucleons are involved and the deuteron breaks up.

G.1 Glauber Formalism and Screening

Let us naively assume the deuteron to be composed of two black sphere (totally absorbing) nucleons. The total cross section for a nucleon is $\sigma_i = \sigma_i^a + \sigma_i^d$, σ_i^a being the absorptive (geometrical) cross section and σ_i^d the diffraction scattering cross section, and for black spheres[5] $\sigma_i^a = \sigma_i^d = \pi R^2$. R is the radius of the sphere. The geometrical cross section for the second nucleon is then $\sigma_2/2$ and the probability that a straight line passing through the first nucleon also passes through the second is $P_{12} = \frac{1}{2} \sigma/4\pi <r^2>$, $<r^2>$ being the mean distance between nucleons. (It is implicitly assumed that $<r^2> \gg R^2$, i.e. the average nucleon separation is much larger than the range of interaction for a single nucleon, and that the probability density of the second nucleon is isotropic about the first). Geometrically, P_{12} is the solid angle subtended by the second nucleon as viewed by the first nucleon. The cross section of the first nucleon shading the second is $1/2\sigma_1 P_{12}$, and an equal term, $1/2\sigma_2 P_{21}$, arises from the interchange of nucleons 1 and 2. The total correction to the geometric nuclear cross section is then $-\sigma_1 P_{12} = -\sigma_2 P_{21}$ and we write

$$\sigma_D^a = \tfrac{1}{2}\sigma_1 + \tfrac{1}{2}\sigma_2 - (\sigma_1 \sigma_2/8\pi)<r^{-2}> \qquad \qquad \text{G.1}$$

where σ_D^a is the deuteron absorptive cross section. The total deuterium cross section becomes

$$\sigma_D = \sigma_1 + \sigma_2 - (\sigma_1 \sigma_2/4\pi)<r^{-2}> = \sigma_1 + \sigma_2 - \delta\sigma \qquad \qquad \text{G.2}$$

$\delta\sigma$ **is** the Glauber screening correction.

The screening correction term may be derived in a more **rigorous** manner using the eikonal approximation of the scattering **amplitude** combined with the optical theorem.[1] The Glauber correction arises from the interference of the scattering amplitudes **from** each nucleon, in the limit where the interaction range is **less** than the mean nucleon separation.

In the rigorous derivation, $\langle r^{-2} \rangle$ loses its direct physical interpretation and should now be considered a parameter **to** be obtained empirically by inverting Eq. G.2. Many calculations of $\langle r^{-2} \rangle$ have been done at low energies,[4,6] using a variety of hd, hp and hn cross sections. All values for $\langle r^{-2} \rangle$ fall between 0.03 mb^{-1} and 0.04 mb^{-1}. At high energies, Carroll[7] **finds** $\langle r^{-2} \rangle$ to be 0.039 mb^{-1} for incident pions and 0.036 for incident protons, independent of beam particle momentum. Eq. G.2 **may** be rewritten as

$$\sigma_D = \sigma_n + \sigma_p - G(\sigma_n + \sigma_p) = (1 - G)(\sigma_n + \sigma_p) \qquad G.3$$

with σ_n and σ_p being the appropriate neutron and proton target cross sections, and G the fractional Glauber correction to $\sigma_n + \sigma_p$ to produce σ_D. For pd reactions G is .053 at 100 GeV/c and by extrapolating Carrol's data, .056 at 400 GeV/c. For π^+ beam particles incident on deuterium at 100 GeV/c, G is found to be .039, using charge symmetry between the $\pi^- p$ and $\pi^+ n$ cross

sections.

G.2 The Hulthen Wave Function

Throughout the text, the deuteron will be viewed as a bound proton and neutron in a pure S (angular momentum L = 0) state, though there is an admixture of 6–7% D (L = 2) state. In this context, the Schrodinger equation (Eq.G.4) may be solved for the deuteron wave-function in coordinate space with $L^2\psi = 0$, where L^2 is the angular momentum operator squared, and we assume a pure S-state neglecting the angular dependence.

$$\left[-\frac{\hbar^2}{2M_r}\, \frac{1}{r}\, \frac{d^2}{d^2r}\cdot r + \frac{\hbar^2 L^2}{2 M_r r^2} + V(r) \right]\psi(r) = E\psi(r) \qquad \text{G.4}$$

M_r is the reduced mass of the proton-neutron system and is set equal to one-half the nucleon mass ($2M_r = m$) and $-E$ is the binding energy (B) of the deuteron. The solution as r becomes infinite has the form

$$\psi \sim e^{-\alpha r}(1-e^{-\mu r})/r \equiv u(r)/r \qquad \text{G.5}$$

where $\alpha = (Bm)^{1/2}$. Using the notation $\beta = \alpha + \mu$

$$u(r) = \left[2\alpha\beta(\alpha + \beta) \right]^{\frac{1}{2}}(e^{-\alpha r} - e^{-\beta r})/\left[2\pi(\beta - \alpha) \right] \qquad \text{G.6}$$

and β is adjusted to give a reasonable description for the wave-function. Hulthen and Sugawara[8] give values of $\alpha = .0456$ GeV/c and $\beta = .260$ GeV/c, and with the use of these values in Eq. G.6, the wave-function will be referred to as the Hulthen wave-function.

The nucleons have a momentum distribution (Fermi motion) that may be calculated by taking the Fourier transform of the Hulthen wave-function, as in Eq. G.7

$$\phi(\vec{p}) = (1/2\pi)^{3/2} \int \psi(\vec{r}) e^{-i\vec{p}\cdot\vec{r}} \, d^3\vec{r} \qquad \text{G.7}$$

The wave-function in momentum space is directionally isotropic and has the form

$$\phi(p) = k(\beta^2 - \alpha^2)/\left[(p^2 + \alpha^2)(p^2 + \beta^2)\right] \qquad \text{G.8}$$

where k is chosen to normalize $\phi(p)$ as desired. The momentum probability $P(p)$ is then defined by Eq. G.9 using a system of spherical polar coordinates

$$\int |\phi(p)|^2 d^3\vec{p} = \int |\phi(p)|^2 p^2 dp \, d(\cos\theta) \, d\phi = \int P(p) \, dp \qquad \text{G.9}$$

and has the form

$$P(p) = k' p^2/\left[(p^2 + \alpha^2)(p^2 + \beta^2)\right] \qquad \text{G.10}$$

where k' is chosen to normalize $P(p)$ to unity when integrated from $p = 0$ to $p \to \infty$.

G.3 The Impulse Approximation and the Spectator Model

The deuteron has such a small binding energy that the bound nucleons may be considered on mass-shell, i.e. they have masses close to those of free nucleons. In addition the mean nucleon separation $1/\alpha \sim 4$ fermi ($f = 10^{-13}$ cm) is larger than

the range of the nuclear force $R = 1/m_\pi \sim 1.4$ f, where m_π is the mass of the pion. It is then very likely that a beam particle will interact with only one target nucleon and that this interaction will be similar to a beam particle-free target interaction, provided that the interaction time is much less than the characteristic time of the deuteron. The interaction time, $\tau = R/\beta$ where β is the incident particle velocity and at high energies is 1, is less than $.5 \times 10^{-23}$ seconds. The characteristic time τ_d defined using the Uncertainty Principle $\beta \tau_d \simeq 1$, is $\sim 2 \times 10^{-21}$ s, indeed much greater than τ. The bound target nucleon is then considered "frozen" during the time of interaction.

The above is the basis of the impulse approximation model of Chew.[9] The non-interacting or spectator nucleon is expected to have the same momentum after the collision, when it is freed from the deuteron, as its fermi motion before the collision. Neutron target interactions in deuterium will then have a spectator proton associated with them, and vice-versa. Furthermore, if the Hulthen wave-function is a good description of the deuteron, the spectator momentum distribution is known. Consequently, the neutron target momentum may be determined through momentum conservation, the deuteron as a whole being at rest in the LAB.

On an event-by-event basis, the target three-momentum is equal and opposite to the spectator momentum. One has a choice

in determining the target energy, either letting the neutron target be on mass-shell ($E_t^2 = p_t^2 + m_t^2$), or conserving total energy by letting the energy of the target be the difference of the energy between the deuteron and the spectator proton. The second choice puts the neutron target off mass-shell, but Fridman[4] believes this choice to be more in the spirit of the impulse approximation model, and we therefore use Eqs. G.11 to define the target momentum

$$\vec{P}_t = -\vec{P}_s \qquad\qquad\qquad \text{G.11a}$$

$$E_t = m_d - E_s \qquad\qquad\qquad \text{G.11b}$$

where the t, s and d subscripts denote target, spectator and deuteron values.

The empirical validity of the impulse approximation would then seem to rest on how well the spectator proton momentum distribution matches the Hulthen prediction. Unfortunately, there are complications. The maximum spectator momentum is on the order of 300 to 400 MeV/c and the distribution peaks at 45 MeV/c. However, at best we see spectator proton tracks no less than 1 mm in length (80 MeV/c). Therefore, the Hulthen distribution predicts roughly 2/3 of the neutron target events to have invisible spectators, i.e. be odd-prong events, which limits the data available. Also, proton target events can produce slow protons in the forward direction which may be misidentified as spectator protons. To

be safe, we must then use only backward spectator events to test the hypothesis, which further limits our data.

The event distribution as a function of target momentum is given in Eq. G.12.

$$d^3N/dp_t d\cos\theta_t d\phi_t \propto F(p_b, p_t, \cos{_t})P(p_t) \qquad \text{G.12}$$

where θ_t and ϕ_t are the spherical coordinate angles in the Beam Coordinate System in the LAB. See App. A.3. The b subscript refers to beam particle values, and F is the Mueller flux factor, given in Eq. G.13.

$$F = \left[(\tilde{p}_b \cdot \tilde{p}_t)^2 - m_b^2 m_t^2 \right]^{\frac{1}{2}} = \left[(E_b E_t - p_b p_t \cos\theta_t) - m_b^2 m_t^2 \right]^{\frac{1}{2}} \qquad \text{G.13}$$

Use of the Mueller flux factor in Eq. G.12 makes d^3N invariant under Lorentz transformations. Substituting in spectator for target variables using Eqs. G.11 yields the spectator event distribution in Eq. G.14

$$d^3N/dp_s d\cos\theta_s d\phi_s \propto F^s(\tilde{p}_b, \tilde{p}_s, \cos\theta_s)P(p_s) \qquad \text{G.14a}$$

where

$$F^s(p_b, p_s, \cos\theta_s) = \left[(E_b E_s + p_b p_s \cos\theta_s)^2 - m_b^2 m_s^2 \right]^{\frac{1}{2}} \qquad \text{G.14b}$$

The beam is assumed to be unpolarized and we may trivially

integrate Eq. G.14a over ϕ_s to give

$$d^2N/dp_s\,d\cos\theta_s \propto F(\tilde{p}_b,\tilde{p}_s,\cos\theta_s)P(p_s) \qquad\qquad G.15$$

Integrating Eq. G.15 over p_s, defines the spectator distribution as a function of $\cos\theta_s$

$$dN/d\cos\theta_s \propto <F(\tilde{p}_b,\cos{}_s)> \qquad\qquad G.16a$$

where <F> is an average value of the flux factor, now a function of $\tilde{p}_b$ and $\cos\theta_s$ only. The value of <F> will have a maximum when the spectator is moving in the beam dirction, i.e. when $\cos\theta_s$ is equal to 1. The minimum of <F> will occur at $\cos\theta_s = -1$. A backwards-forwards asymmetry in the spectator distribution as a function of $\cos\theta_s$ should be seen.

In a similar manner, we may average Eq. G.15 over $\cos\theta_s$ to find the spectator momentum distribution as a function of p_s. See Eq. G.16b.

$$dN/dp_s \propto <F(\tilde{p}_b,\tilde{p}_s)>P(p_s) \qquad\qquad G.16b$$

Here the flux factor is now a function of $\tilde{p}_b$ and $\tilde{p}_s$ only.

For the momenta allowed by $P(p_s)$, this $<F>$ is always close to unity, such that dN/dp_s should look like the Hulthen momentum distribution.

The spectator distributions for both 100 GeV/c hd and 400 Gev/c pd data are given in Figures G.1, 2, 3 and 4. Only those spectators backwards with respect to the beam dirction are plotted. With respect to ϕ_s, the distributions in Figures G.1a and 2a should be flat, but there are deficiencies at $0^0/360^0$ and 180^0. At these angles, the spectator track projected onto the film plane is anti-parallel to the beam direction, and short stubs can be easily overlooked during scanning and measuring. This deficiency is then not surprising. Figures G.1b and 2b show the $\cos\theta_s$ distributions. The curves are the predictions of the spectator model in Eq. G.16a normalized to the area under the data in the histograms. The predictions and the data are consistent except perhaps in the first data bin, where the angle between the beam and the spectator proton goes to 180^0 and a loss of short stubs is again expected. The forward-backwards asymmetry can now be seen in the backwards spectators by the asymmetry about $\cos\theta_s = -0.5$.
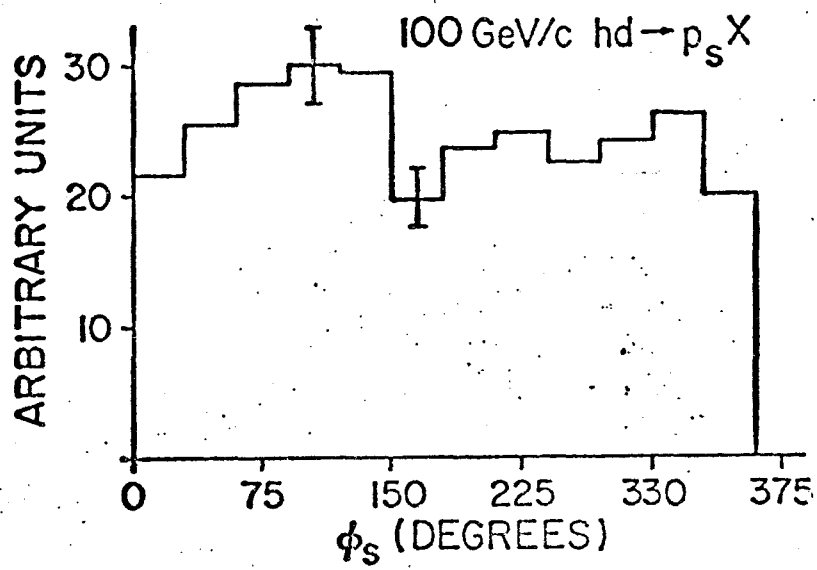
Fig. G. 1a

Fig. G 1b

Fig. G.2a

Fig. G.2b

100 GeV/c   hd $\rightarrow$ p$_s$ X

Fig.G.3

400 GeV/c pd → p_s X

p_s (MeV/c)
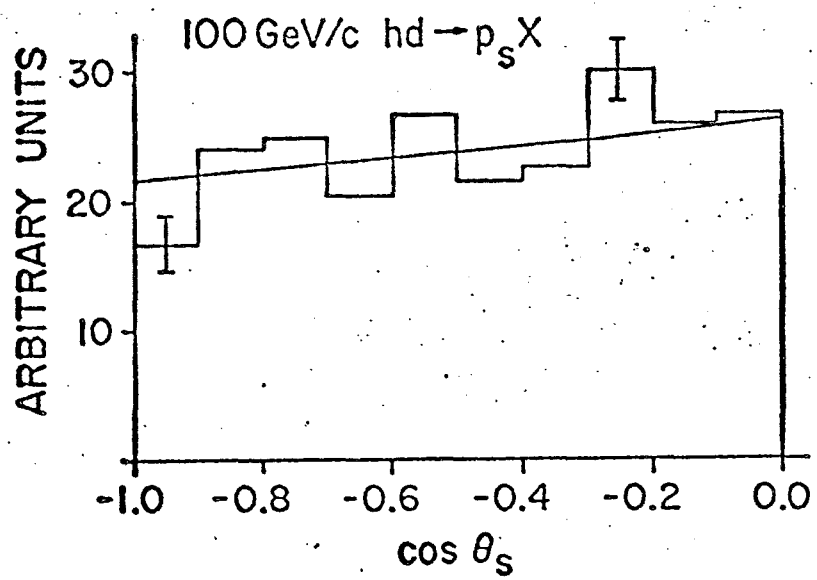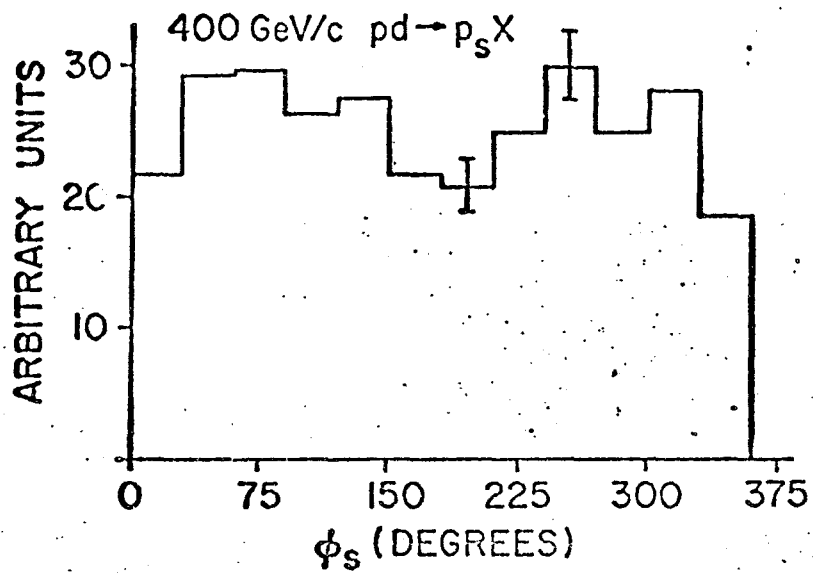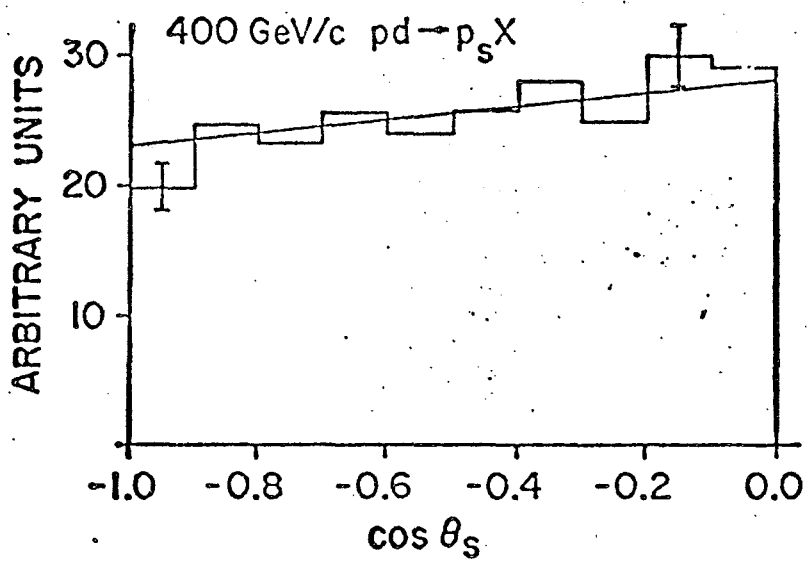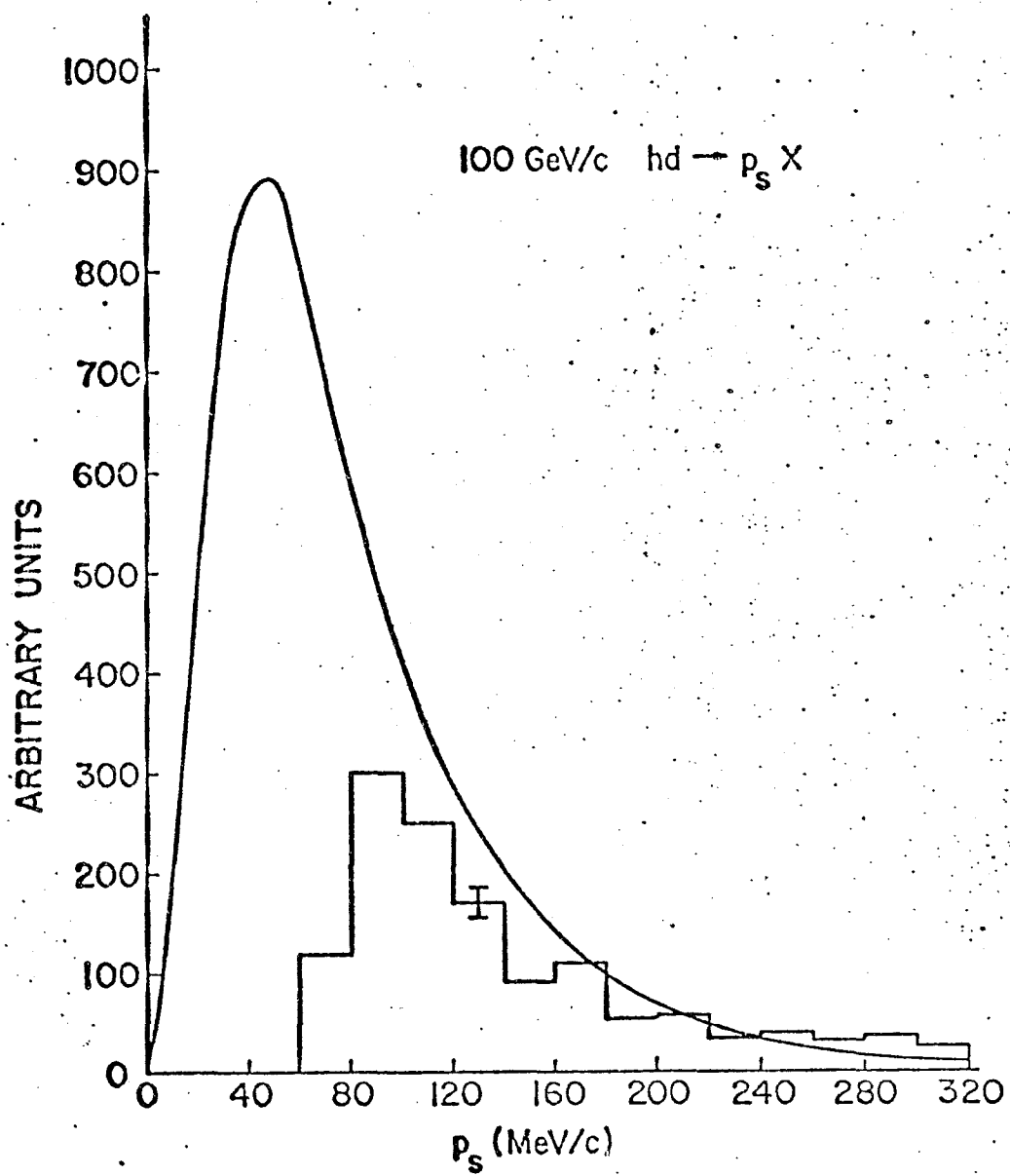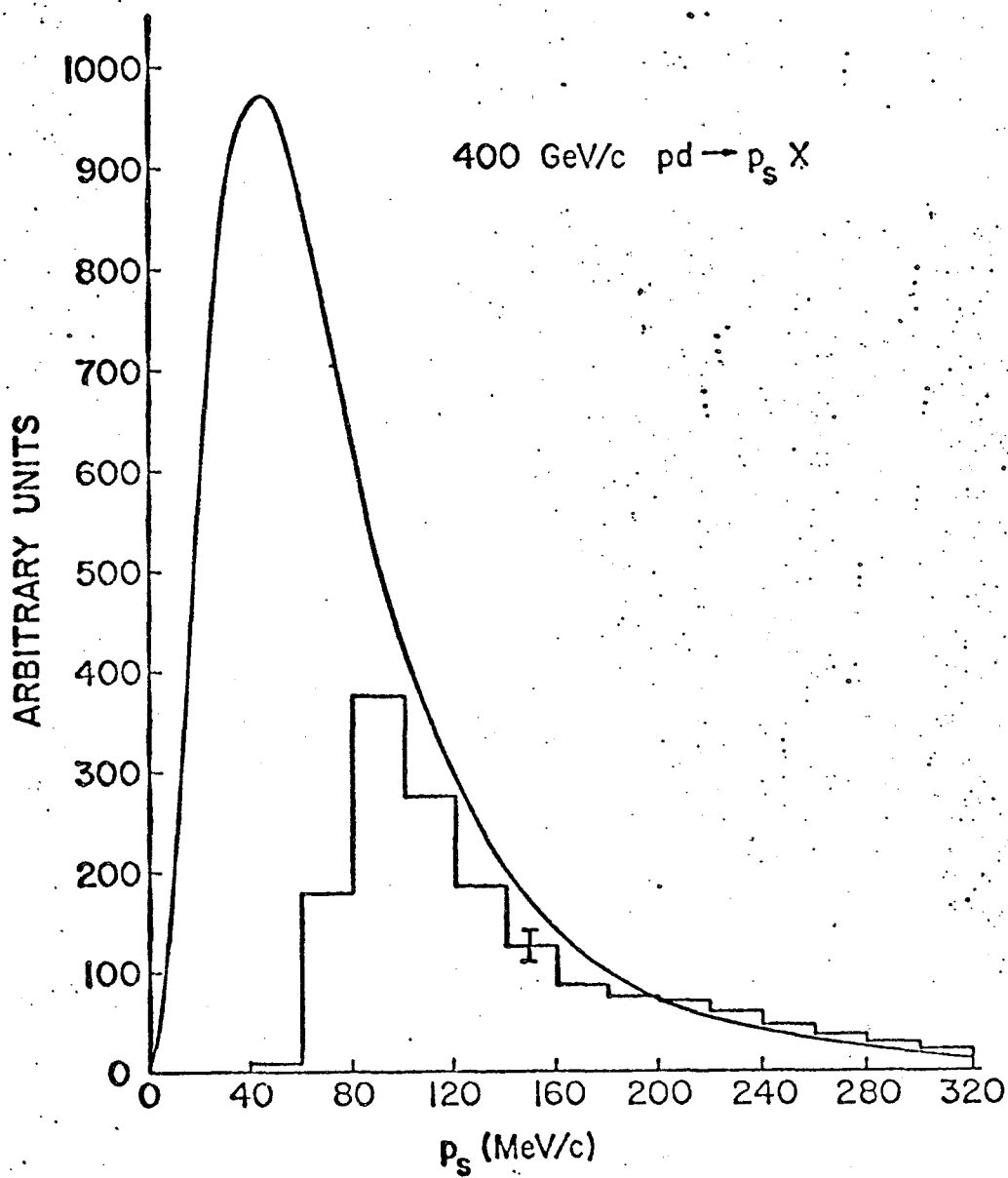
Fig. G.4

The data in Figs. G.3 and G.4 are the momentum magnitudes of the spectator protons weighted by $(1 + F)$ where F is the Mueller flux factor for the associated target in the forward direction reflected into the backwards direction $(\theta_t = -\theta_s \to -\theta - 180^0)$. The steep fall-off in the data below 80 MeV/c corresponds to the missing of all stubs less than 1 mm in length. If the spectator model is correct, the distribution obtained from the data by this method should be identical to a forward-plus-backward spectator distribution, provided we could unambiguously recognize the forward spectators. The predictions of the spectator model using a flux factor weighted Hulthen wave-function averaged over $\cos\theta_s$, are given by the curves. The curves are normalized to the odd-prong plus weighted even-prong backward spectator events. While below a momentum of 160 MeV/c the predictions seem somewhat high, the general shape is in good agreement with the visible spectator data.

We then assert that the impulse approximation spectator model is at least qualitatively correct, the shapes of the spectator distributions being understood. We further claim to be able to recognize a neutron target event if it is an odd-prong event or an even-prong event with a backwards spectator. Corrections for odd-prong events from coherent deuteron interactions with an invisible final-state deuteron are discussed in Section III.C. In addition, by generating a Hulthen target distribution with a

Monte Carlo program for proton targets in 100 GeV/c pp → pX
data[9], we have estimated the contamination to the odd-prong and
backwards-spectator event samples from proton targets in deuter-
ium. Values of .005 and .025 were obtained. (There is no
contamination to the neutron target slow proton sample,
$hn(p_s) \rightarrow (p_s)p_{sl}X$, because we don't expect two protons with less
than 1.4 GeV/c momentum in the LAB from a proton target inter-
action).

G.3 "Fermi-Smearing"

The term "Fermi-smearing" will be defined as the resulting
uncertainty in kinematic variables due to the unknown motion of
a target in an invisible spectator event. In our neutron target
sample, at least 2/3 of the data are odd-prong events, even if
forward spectator protons are identifiable.

To demonstrate the effect of Fermi-smearing on our data,
we choose to use the center-of-mass energy $s^{\frac{1}{2}}$. For a 400 GeV/c
proton incident on a neutron target in a deuteron at rest in the
LAB; the distribution of $s^{\frac{1}{2}}$ is given in Fig. G.5. The value of
$s^{\frac{1}{2}}$ for a neutron target at rest is $s_o^{\frac{1}{2}} = 27.43$ GeV, and $s_+^{\frac{1}{2}}$ and $s_-^{\frac{1}{2}}$
are the maximum and minimum values of $s^{\frac{1}{2}}$ for an event with an
unseen spectator proton ($p_s <$ 80 MeV/c). The cross-hatched
area is then the area of known   values, and unseen spectator
events have possible values within the range of $s_+^{\frac{1}{2}}$ and $s_-^{\frac{1}{2}}$.
Note that the average value of $s^{\frac{1}{2}}$, $<s^{\frac{1}{2}}> = 27.52$ GeV is slightly
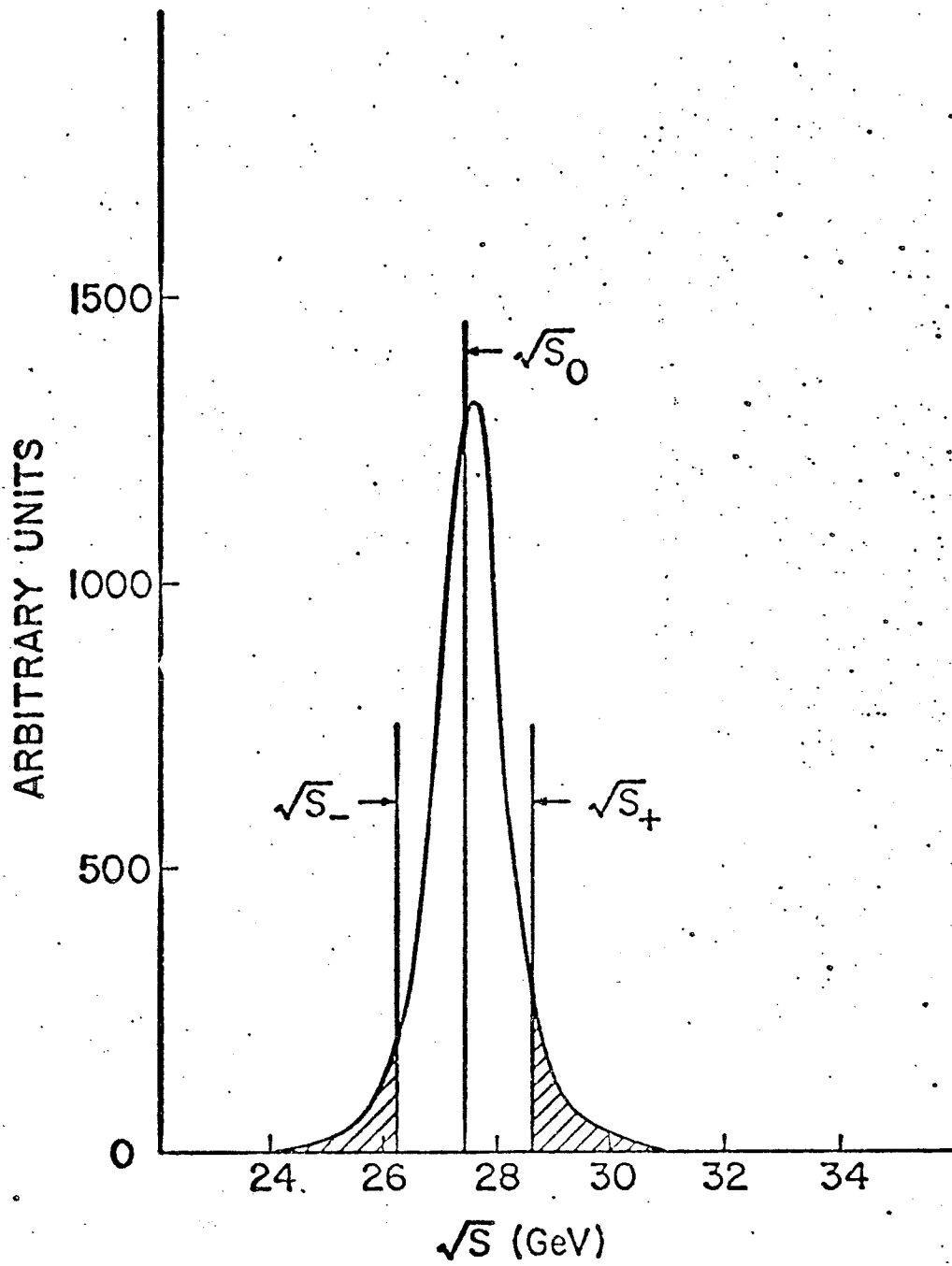
Fig. G.5

higher than $s_o^{\frac{1}{2}}$.

What value should then be assigned to $s^{\frac{1}{2}}$ for the odd-prong events? Let us generate a sample of spectator events using our spectator model and call this the "real" distribution. For each generated event, we either guess that the target is at rest or generate a spectator momentum, again using our model, but independently of the "real" event generated. If we calculate $s^{\frac{1}{2}}$ for each choice of target, we then find that the deviation in $s^{\frac{1}{2}}$

$$\delta(s^{\frac{1}{2}}) \equiv \sum (s_r^{\frac{1}{2}} - s_g^{\frac{1}{2}})^2/N \qquad \qquad \text{G.17}$$

where the summation is over each set of targets, N is the number of sets generated, $s_r^{\frac{1}{2}}$ is the real $s^{\frac{1}{2}}$ value and $s_g^{\frac{1}{2}}$ is one of the two types of guesses, is smallest for the stationary target guess. For 2000 events, $\delta s^{\frac{1}{2}}$ was .23 GeV for the stationary target and .33 GeV for the generated target choice. The same result was obtained when generating M^2 missing-mass values from pp $\rightarrow$ pX data; the minimum deviation in M^2 was given by the zero target momentum estimate. Therefore, if a spectator is not visible, the target will be assumed to have no three-momentum.

G.4 Rescattering

Estimates of the amount of rescattering events present in deuteron break-up events can be made. If normalizing single nucleon cross sections to hadron-deuterium cross sections, one

must correct for the loss of events to the rescattering process, i.e. deuteron break-up events are not the simple sum of proton and neutron target events corrected for Glauber screening.

Lys'[11] prescription for calculating F_{rs}, the rescattering fraction for all inelastic deuteron break-up events, is given in Eqs. G.18

$$F_{rs} = (1 - P_2)F_{rs}(\geq 3) + P_2 F_{rs}(2) \qquad G.18a$$

where

$$F_{rs}(\geq 3) = 1 - (M(p_s)/M(tot))\left[1 + \frac{\sigma(hp,N\geq4)}{\sigma(hn,N\geq3)}\right] \qquad G.18b$$

is the rescattering fraction for all events with 3 or more prongs, $M(p_s)$ is the number of proton spectator events, $M(tot)$ is the total number of deuteron break-up events with 3 or more prongs, and (hp, $N \geq 4$) ((hn, $N \geq 3$)) is the hadron-proton (h-neutron) cross section for events with 4 (3) or more prongs. $F_{rs}(2)$ is the rescatter fraction for inelastic $N = 2$ events and is estimated to be one-half $F_{rs}(\geq 3)$. P_2 is the inelastic 2-prong probability for hd interactions, as discussed in Section III.D. The above calculations yield an F_{rs} value of 0.208 ± 0.019 at 100 GeV/c and a preliminary value of 0.195 ± 0.017 at 400 GeV/c.[11] The F_{rs} for pion beam particles incident on deuterium is 0.145 ± 0.026. The results appear to be energy independent above 20 GeV/c incident beam momenta.[10]

REFERENCES

1) R. J. Glauber, Phys Rev. 100, 242 (1955).

2) V. Franco and R. J. Glauber, Phys. Rev. 142, 1195 (1966).

3) G. F. Chew, Phys. Rev. 80, 196 (1950).

4) A. Fridman, Fortschritte der Physik 23, 243 (1975).

5) Any quantum mechanics text derives this result using the eikonal approximation. For example see: K. Gottfried, "Quantum Mechanics," Vol.I (W. A. Benjamin Inc., New York 1966).

6) D. R. Harrington, Phys. Rev. 135, B358 (1964);
   W. Galbraith et al., Phys. Rev. 138, B913 (1965);
   D. V. Bugg et al., Phys Rev. 146, 980 (1966).

7) A. S. Carrol et al., Phys. Lett. 61B, 303 (1976).

8) L. Hulthen and M. Sugawara, "Handbuch der Physik," Vol. 39, S. Flugge ed. (Springer-Verlag, Berlin 1957).

9) The data were obtained from the University of Michigan.

10) J. E. A. Lys et al., Phys Rev. D15, 1857 (1977).

11) S. Dado et al., Phys. Rev D (to be submitted).